NASA/CR-2026000820

Icing Physics Studies Using the 3D SIDRM Test Article: 2023 Icing Tests Analysis

Tadas P. Bartkus
Ohio Aerospace Institute, Brook Park, Ohio

Sam Lee
HX5, LLC, Brook Park, Ohio

January 2026

NASA STI Program . . . in Profile

Since its founding, NASA has been dedicated to the advancement of aeronautics and space science. The NASA scientific and technical information (STI) program plays a key part in helping NASA maintain this important role.

The NASA STI program operates under the auspices of the Agency Chief Information Officer. It collects, organizes, provides for archiving, and disseminates NASA's STI. The NASA STI program provides access to the NTRS Registered and its public interface, the NASA Technical Reports Server, thus providing one of the largest collections of aeronautical and space science STI in the world. Results are published in both non-NASA channels and by NASA in the NASA STI Report Series, which includes the following report types:

- TECHNICAL PUBLICATION. Reports of completed research or a major significant phase of research that present the results of NASA programs and include extensive data or theoretical analysis. Includes compilations of significant scientific and technical data and information deemed to be of continuing reference value. NASA counterpart of peer-reviewed formal professional papers but has less stringent limitations on manuscript length and extent of graphic presentations.

- TECHNICAL MEMORANDUM. Scientific and technical findings that are preliminary or of specialized interest, e.g., quick release reports, working papers, and bibliographies that contain minimal annotation. Does not contain extensive analysis.

- CONTRACTOR REPORT. Scientific and technical findings by NASA-sponsored contractors and grantees.

- CONFERENCE PUBLICATION. Collected papers from scientific and technical conferences, symposia, seminars, or other meetings sponsored or cosponsored by NASA.

- SPECIAL PUBLICATION. Scientific, technical, or historical information from NASA programs, projects, and missions, often concerned with subjects having substantial public interest.

- TECHNICAL TRANSLATION. English-language translations of foreign scientific and technical material pertinent to NASA's mission.

Specialized services also include organizing and publishing research results, distributing specialized research announcements and feeds, providing information desk and personal search support, and enabling data exchange services.

For more information about the NASA STI program, see the following:

- Access the NASA STI program home page at http://www.sti.nasa.gov

NASA/CR-2026000820

Icing Physics Studies Using the 3D SIDRM Test Article: 2023 Icing Tests Analysis

Tadas P. Bartkus
Ohio Aerospace Institute, Brook Park, Ohio

Sam Lee
HX5, LLC, Brook Park, Ohio

Prepared under Contract 80GRC020D0003

National Aeronautics and
Space Administration

Glenn Research Center
Cleveland, Ohio 44135

January 2026

Acknowledgments

The authors would like to thank the many key collaborators without whom this work would not have been possible. Quentin Schwinn and Jordan Salkin of the NASA Imaging Technology Center deserve special thanks for their tremendous work in scanning and processing the ice shape data, in addition to recording and processing the time-lapsed video. The authors would also like to acknowledge the staff at the NASA Icing Research Tunnel for their outstanding support as preparing for the test entry and operating the facility in glaciated conditions was a demanding effort. Thank you to intern Emma Nagy from the Georgia Institute of Technology for providing support in analyzing heater measurements. Finally, the authors wish to acknowledge the financial support of the Propulsion Technologies subproject of the Advanced Air Transport Technology project (AATT) under NASA's Advanced Air Vehicles Program (AAVP). This work was performed under the Glenn Engineering and Research Support Contract (GEARS), Contract No. 80GRC020D0003.

This work was sponsored by the Advanced Air Vehicles Program
at the NASA Glenn Research Center.

Level of Review: This material has been technically reviewed by expert reviewer(s).

NASA STI Program/Mail Stop 050
NASA Langley Research Center
Hampton, VA 23681-2199

Icing Physics Studies Using the 3D SIDRM Test Article: 2023 Icing Tests Analysis

Tadas P. Bartkus
Ohio Aerospace Institute
Brook Park, Ohio 44142

Sam Lee
HX5, LLC
Brook Park, Ohio 44142

Executive Summary

In-flight icing is an important safety issue and is a factor that affects aircraft design and performance. Newer regulations are driving a need for improvements in airframe and engine icing simulation capability. Experimental data are required for the development of icing physics models and simulation validation. To that end, NASA conducted a series of component level icing physics tests at the NASA Icing Research Tunnel (IRT) in 2022 and 2023 that studied both supercooled liquid and ice-crystal icing. The test article that was utilized replicated 3D geometrical features of an inter-compressor duct and strut region of a turbofan engine. The surfaces of the Simulated Inter-compressor Duct Research Model (SIDRM) can be heated to simulate the warm surfaces of the turbofan inter-compressor duct. The test article was instrumented with pressure taps, heaters, heat flux gauges, and thermocouples, while 3D laser scans, photographs, video, and ice mass measurements were utilized to characterize the icing behavior. The 2023 tests utilized modified struts, which were larger compared to the tests conducted in 2022. There were multiple objectives for the 2023 test entry. The primary aim of these tests was to generate ice accretions on the SIDRM test article under well-characterized icing conditions. The ice accretion tests explored different test conditions to measure that parameter's impact on ice accretion size, location, and characteristics (quality, shedding behavior, and physical attributes) under supercooled liquid and ice crystal clouds. Also, aerodynamic tests were conducted to characterize the flow field. Finally, icing threshold tests were performed to determine heat flux settings that differentiated between icing and running wet conditions for both supercooled liquid and ice crystal clouds. This report presents analysis of data collected from tests conducted in 2023, with comparison to 2022 data where applicable, and discusses the impact of the modified struts. The icing measurements collected during the SIDRM tests will be used to develop and validate 3D computational engine icing tools, such as GlennICE, that predictively assesses the onset and growth of ice. One of the goals of the sponsoring NASA project is to develop simulation models and tools that can assist in the design and certification of engines for flight in icing conditions in a cost-effective way.

Nomenclature

AOA	angle of attack, also AoA, °
c	chord length, in.
C_p	pressure coefficient (nondimensional)
LWC	liquid water content, g m^{-3}
IWC	ice water content, g m^{-3}
MVD	median volumetric diameter, µm
P	pressure, Pa

s	unwrapped distance, in.
T	temperature, °C
t	time, spray duration, min
TWC	total water content, the sum of liquid and ice water content, g m^{-3}
U	airspeed (knots)
x	SIDRM span coordinate, (+) towards ceiling, zero at midspan leading edge, in.
y	SIDRM thickness coordinate, (+) towards non-instrumented side, zero at midspan leading edge, in.
z	SIDRM chord coordinate, (+) upstream, zero at midspan leading edge, in.

Subscripts

0	total
s	static
tap	pressure tap

1.0 Introduction

Numerous reports of turbofan engine power-loss or damage events have been attributed to the ingestion of ice crystals (Refs. 1 and 2). These events typically occur in deep convective updraft systems and have included engine stall, rollback, flameout, surge, and engine component damage. Mason et al. (Ref. 3) hypothesized that ice crystals ingested into the engine undergo partial melting within the warm compressor system and then, as a mixed-phase water mass, accrete on surfaces within the engine core. Stressing the importance of mitigating this threat posed by engine icing, the Federal Aviation Administration (FAA) released a document outlining existing ice crystal icing research needs (Ref. 4). Research efforts in understanding the physics of ice crystal icing have grown to address this flight safety threat. Numerous component level tests utilizing static airfoils have been conducted investigating the fundamental ice crystal icing physics (Refs. 5 to 17). More complex ice crystal accretion studies utilized heated ducts (Refs. 18 to 19). More recently, the National Research Council of Canada commissioned the Ice Crystal Environment Modular Axial Compressor Rig (ICE-MACR) to simulate turbofan compressor physics more closely (Refs. 20 to 23). With rotating machinery, the subscale rig allows for studies of fundamental physics such as centrifuging, particle breakup, annular accretion, and particle melt due to compression and conductive heating.

NASA Glenn Research Center (GRC) has conducted several experiments to better understand ice crystal icing. Multiple full-scale engine icing tests have been conducted at the NASA Propulsion Systems Laboratory (PSL) (Refs. 24 to 34). Of note was the engine icing test entry utilizing the heavily instrumented, unmodified Honeywell ALF502R-5 engine, serial number LF11 (Ref. 29). Tests were successful in replicating known engine rollback test conditions, indicating reliable simulation of flight conditions and engine performance in a ground facility. Several key findings related to surface heating were provided. Testing data showed that the addition of upstream heat sources from the spinner heat and inlet guide vane anti-ice system promoted ice accretion in the core flow path and rollback. In addition, increasing the fan speed raised the temperature in the core flow path suppressing accretion, avoiding engine rollback. Video that was made publicly available (Ref. 30) showed ice accretion aft of the exit guide vane with shark teeth-shaped ice features that drew interest from the engine icing community.

The full-scale engine icing tests provided valuable information replicating realistic flight conditions. Due to the inaccessibility to the test section and internal compartments of the engine, much of the ice accretion data is qualitative in nature. Quantitative measurements of ice mass and accretion geometry, including surface heat flux was not measured or possible. Quantitative data are needed to properly predict the onset and growth of ice within turbofan engines from first principles. To that end, NASA has conducted a series of component level tests to study the fundamental ice crystal accretion physics (Refs. 5, 6, 8, 9, 35 to 38), supplementing what was learned in the full-scale engine icing tests. The first two test entries in this series of accretion physics studies were conducted in the NASA PSL in 2016 (Refs. 8 and 9) and 2018 (Refs. 5 and 6). These tests generated a dataset of ice accretions on an unheated NACA 0012 airfoil with a focus on the cloud melt ratio impact on ice accretion. Quantitative ice geometry measurements were limited to extracting 1D and 2D ice shapes from orthogonal video images that captured the ice growth at the NACA 0012 leading edge.

NASA conducted a second series of component level icing physics tests at the NASA Icing Research Tunnel (IRT) in 2022 and 2023 utilizing the Simulated Inter-compressor Duct Research Model (SIDRM), a 3D test article whose geometry is representative of an inter-compressor duct and strut region of a turbofan engine (Refs. 35 to 39). The test article surfaces can be heated to simulate the warm surfaces of the turbofan inter-compressor duct, and is instrumented with heaters, heat flux gauges, thermocouples, and pressure taps. It should be noted that these tests do not fully simulate the environment within the engine. The testing air temperatures were below freezing, and the icing clouds were fully glaciated before making impact with the test article surface. It is believed that ingested ice crystal clouds are partially melted as they pass through warm engine passages before impacting internal engine components. In addition, this open geometry will result in different pressures and flow compared to the ducted region of the compressor. Despite these limitations, the data collected provide quantitative measurements useful for better understanding of the fundamental ice crystal icing physics.

The aim of these tests was to generate ice accretions on the SIDRM test article under well-characterized conditions. Icing tests were conducted under supercooled liquid icing and ice crystal icing conditions. Results from ice accretion tests conducted in 2022 have been previously reported (Refs. 35 and 36). The supercooled liquid icing tests provided simulation validation data on a 3D geometry. In addition, an estimate of collection efficiency was back-calculated from ice accretion geometry (Refs. 36 and 37) which is also required for ice crystal icing simulation. Several key findings were noted from the ice crystal icing tests (Ref. 35). A sufficiently high surface heat flux at the leading edge can provide a continuous supply of liquid melt to critical accretion zones downstream, resulting in elevated ice mass accretions. Also, warmer heater settings in critical accretion zones can suppress ice accretion. These findings are consistent with icing behavior observed in full-scale engine icing tests conducted previously at GRC (Ref. 29). Ice crystal accretion test runs investigating the contribution of liquid melt generated at the leading edge found that the melt can be transported downstream to critical accretion regions in two forms, via runback and splash. The form of melt supplied downstream affected accretion behavior and features. Shark teeth-shaped ice accretions were generated at certain test conditions, a physical attribute that has been observed in full-scale engine icing tests (Ref. 29).

The results presented in this report are from the icing tests conducted in 2023 utilizing modified struts, which were larger compared to the tests conducted in 2022 (7-in. NACA 0018 vs. 4-in. NACA 0012). Icing tests were conducted under supercooled liquid (SCL) icing and ice crystal (IC) icing conditions. The objective of the 2023 ice accretion tests was to identify the factors that influenced icing size, location, and characteristics (quality, shedding behavior, and physical attributes), and to measure the impact of the modified struts. Aerodynamic tests were conducted to characterize the flow field around the test article and determine to greater accuracy the stagnation line location at the leading edge. Finally, icing threshold tests were conducted under SCL and IC clouds to determine heat flux settings that differentiate between running wet and icing conditions. This report discusses by section, (Section 2.0) the SIDRM test article, (Section 3.0) the IRT reference pressure issue, (Section 4.0) the aerodynamic tests, (Section 5.0), the supercooled liquid icing tests, (Section 6.0) the ice crystal icing tests, and (Section 7.0) the heat flux icing threshold tests.

The icing physics data measured during the SIDRM test entries will be used to develop and validate engine icing computational tools (Refs. 40 to 52) such as the 3D simulation tool GlennICE (Refs. 40 and 49). These testing efforts were part of NASA's Advanced Air Transport Technology (AATT) project activities to improve understanding of the ice growth physics and advance engine aero thermodynamic modeling tools to predictively assess the onset and growth of ice in current and future engines during flight. Simulation tools like GlennICE will allow industry to design and certify engines for flight in icing conditions in a cost-effective way.

2.0 SIDRM Test Article

A limited description of the experimental set-up is provided here. For the interested reader, a more detailed description is provided elsewhere (Refs. 38 and 39). The icing test entry utilized the SIDRM test article, which is shown in Panel (A) of Figure 1. The test article replicates 3D geometrical features of an inter-compressor duct and strut region of a turbofan engine and is highlighted in the circled regions of Panels (B) and (C) of Figure 1. The larger 7-in. NACA 0018 struts are shown in Figure 1(A) and (B).

2.1 Strut Modifications for 2023 Tests

Ice crystal icing tests conducted in 2022 utilized 4-in. NACA 0012 struts where the strut leading edge was located in a linear section of the "ramp" part of the test article, just aft of a small section with a nonlinear curved geometry. Figure 2(A) shows an example of final ice accretions from a typical ice crystal ice accretion test conducted in 2022. The figure shows that the strut had little to no impact in terms of a physical anchoring point as the accretion is largely uniform spanwise and upstream of the strut. During the initial SIDRM geometry design phase, the location of the strut had been placed in the linear section of the ramp with the expectation that it would act as an anchor point for slushy ice that would begin building up at the nonlinear curved section of the ramp. The 4-in. NACA 0012 provided little data in terms of observing the impact of a 3D junction under an ice crystal cloud because ice usually accreted upstream of the strut. Larger 7-in. NACA 0018 struts were installed on each side of the test article with the strut leading edge moved 3 in. forward into the nonlinear curved section of the ramp. The red outline in Figure 2(A) shows approximately where the new strut leading edge would exist compared to the 2022 ice crystal accretion.

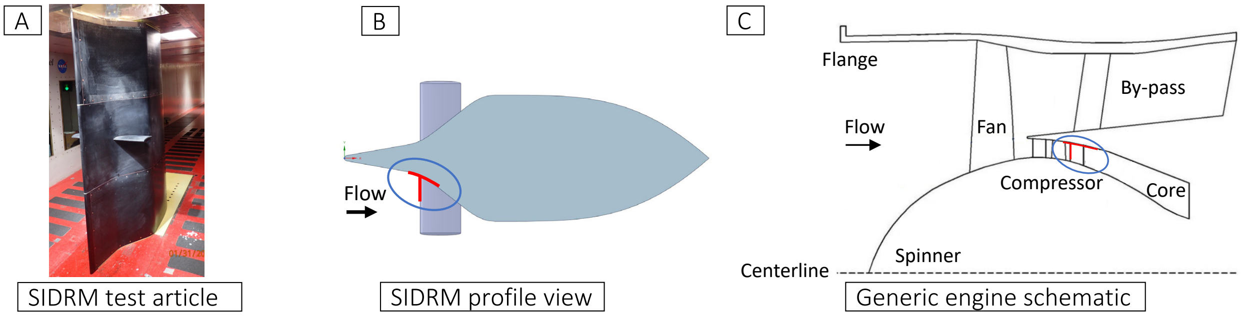

Figure 1.—Panels showing (A) an image of the SIDRM test article, (B) a schematic showing the SIDRM profile view with a focus on the strut main body junction, and (C) how that junction geometry relates to the inter-compressor duct and strut region of a turbofan engine.

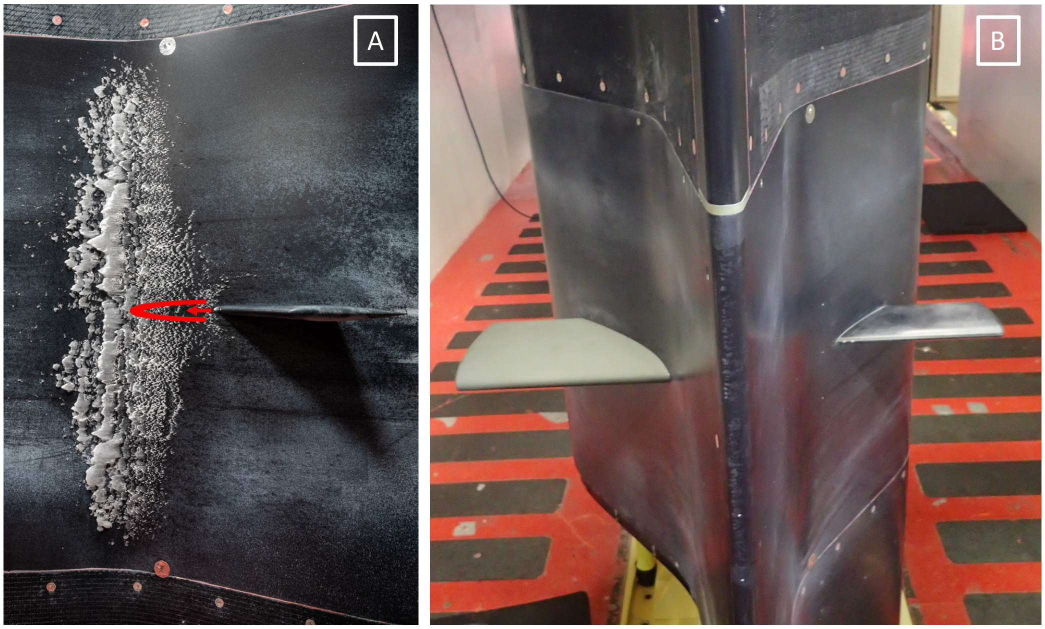

Figure 2.—Panel (A) shows an ice crystal accretion with the 4-in. chord NACA 0012 strut having little impact on the accretion conducted in 2022, and red outline approximating the location a larger strut. Panel (B) provides a comparison of the larger 7-in. NACA 0018 strut with the smaller 4-in. NACA 0012 as the smaller struts were being replaced.

The larger struts will provide a comparison to 2022 supercooled liquid ice accretions and allow for investigation into the impact of a 3D junction on ice crystal icing. Figure 2(B) provides a visual comparison of size and location of the two differently sized struts as the smaller struts were being swapped out for the larger struts.

2.2 SIDRM Orientation Within IRT Test Section

Figure 3 provides an orientation reference for the SIDRM test article within the IRT test section. The test article contains built-in instrumentation which will be detailed in the next subsection. One side is more heavily instrumented and is referred to as the instrumented side, while the other side is less instrumented and for ease is referred to as the non-instrumented side. Figure 3 shows the test article at a positive *AOA* and as a result the entire instrumented side is considered the pressure side, and the non-instrumented side as the suction side. All icing tests were conducted at 0 or positive AoA. Mostly positive but some negative angles of attack were conducted during aerodynamic tests. During these negative *AOA* tests, the pressure and suction sides are flipped compared to the schematic. Figure 3 also shows that the SIDRM test article was oriented such that the instrumented side was nearest the South control room in the IRT.

2.3 SIDRM Built-In Instrumentation

Figure 4 shows an image of the instrumented side of the SIDRM test article with an overlay of the heater zones approximating the locations they heated, along with the locations of several surface mounted thermocouples. The side seen in Figure 4 contains the majority of instrumentation (referred to as the instrumented side), while the other side (referred to as the non-instrumented side) has limited instrumentation for monitoring purposes. The heater zones are independently controlled. A cartridge heater is located at the test article leading edge (Zone 1), and thin film heaters line the inner mold line along the rest of the chord

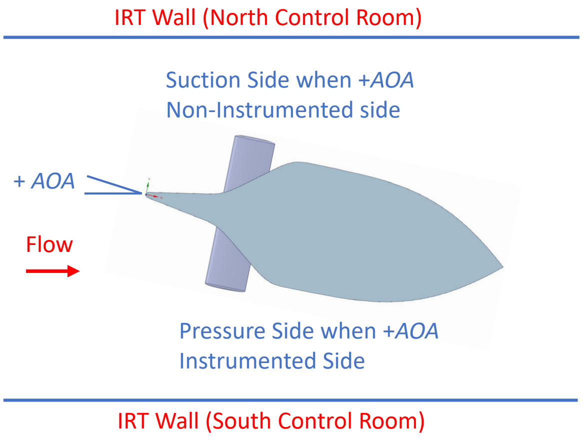

Figure 3.—Schematic of SIDRM test article at a positive AoA with the pressure/suction and instrumented/non-instrumented sides indicated.

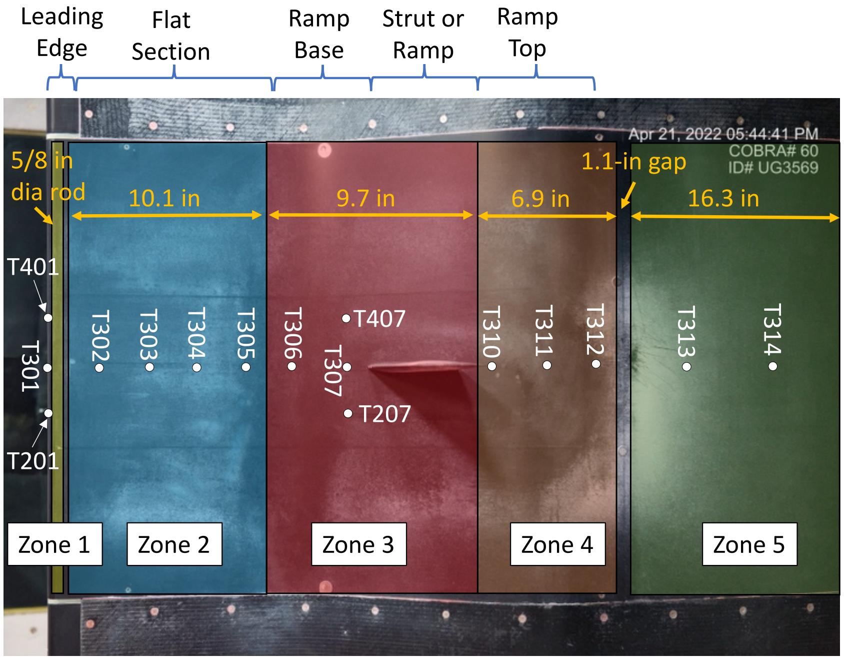

Figure 4.—Image of the SIDRM test article with an overlay of the heater zones (Zone 6 not pictured) approximating the locations they heated, along with the locations of several surface mounted thermocouples.

(Zones 2 to 6). Thin film heaters mirror the non-instrumented side of the test article to maintain symmetry. The heaters span 23 in. and axial lengths covered by the heaters is shown in Figure 4 (the heater footprint is larger due to surface curvature). Heater Zone 6 is not shown in this image, but covers 14.5 in. aft of Zone 5, with 3.2 in. near the trailing edge left unheated for structure fastening purposes. Similarly, the 1.1-in. gap between heater Zones 4 and 5 exists for structure fastening purposes as well. The names and locations of several surface mounted thermocouples are shown indicating in which zone they are located (not shown is T315 in Zone 6). A description of the test article curvature is shown to provide context in the figure, as some of the language will be used later in this report. Ice accretion primarily occurs in Zones 1 to 4 as the surfaces are forward facing to the impinging cloud and are generally the areas of interest.

Appendix A provides nominal locations of surface mounted thermocouples (Table A.1), internally located thermocouples near the leading edge (Table A.2), heat flux gauges located in pockets on the inner mold line (Table A.3), and the heat flux gauges' built-in thermocouples (Table A.4). This report primarily focuses on the surface temperatures, but locations of all the other thermocouples and heat flux gauges are provided in the appendix for completeness and for reference purposes.

Figure 5 is a schematic that indicates the general location of many surface thermocouples and pressure taps on the instrumented side and leading edge. There are 64 pressure taps built into the SIDRM test article. There are 32 taps wrapping around chordwise on each of the test article extensions, each row located about 17.25 in. from the span center. There is some staggering of taps at the leading edge. The appendix provides nominal locations of pressure taps located on the test article outer mold line (Table A.5).

For reference, the profile geometry of the SIDRM main body is provided in Table A.6 of the Appendix. Additional details of the struts locations and dimensions are also provided.

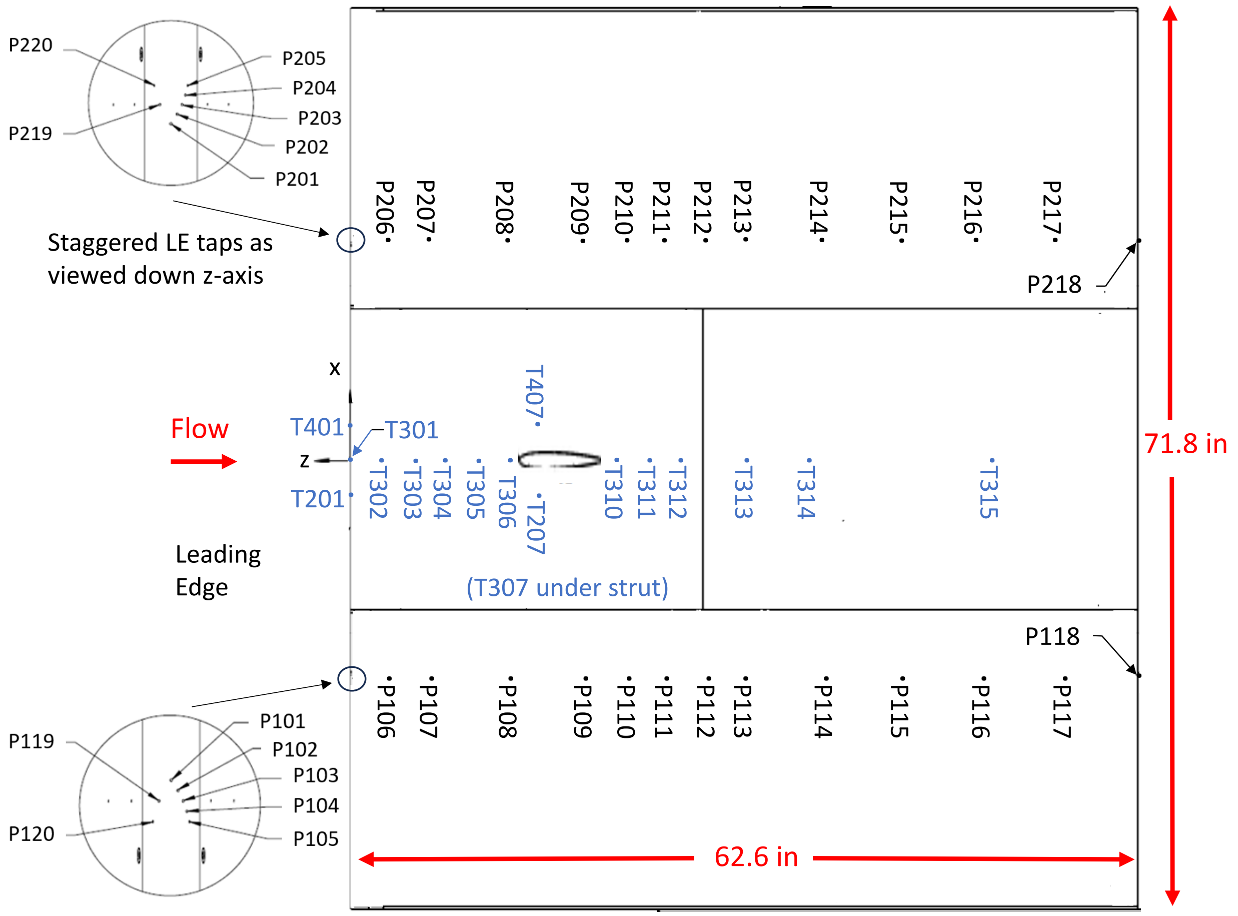

Figure 5.—Schematic of pressure tap and thermocouple locations on SIDRM. The opposite side (non-instrumented side) is not shown but the pressure tap locations mirror the side that is shown (instrumented side), aside from those shown near the leading edge.

3.0 Addressing IRT Reference Pressure Issue Impacts

An issue with pressure measurements was noticed some time after testing had been completed. A reference pressure tube in the IRT pressure system was disconnected and identified as the source of the issue. It was determined that the reference pressure tube had been disconnected starting September 16, 2022, until the issue had been discovered on April 1, 2024. The reading from this pressure line dictates control of the airspeed within the wind tunnel. With incorrect pressure values, the airspeed control system provided erroneous airspeed (U) and liquid water content (LWC) at the test section. This SIDRM test entry took place in early 2023 and was impacted by this issue. The data was reprocessed with corrected airspeeds and LWC values. Table 1 shows the target airspeed and the approximate corrected airspeed rounded to 0.5 knots for reference. Table 1 shows that the corrected airspeed is greater than the target, with negligible discrepancies at lower airspeeds, but larger differences with increasing airspeed. The deviation between target LWC and corrected LWC is a more complex calculation involving various condition settings, with corrected values ranging from 1 to 3% lower than the intended LWC for supercooled liquid water icing tests. Ice crystal icing tests utilize the same spray nozzle injection system, with liquid water glaciating as the cloud traveled from the spray bar to the test section. There is a component of ice crystals recirculating in the closed loop tunnel that contributes to the overall ice water content (IWC) at the test section. Reprocessing for corrected IWC is not possible, and it is unknown how the reference pressure tube and airspeed discrepancy impacted IWC for the ice crystal icing tests. For this report, the IWC is treated as if there was no impact from the reference pressure issue.

Part of the test objectives was to conduct some repeat test runs from 2022, however this reference pressure tube reference issue adds some variance. The first SIDRM test entry took place in early 2022 and was not impacted by this reference pressure tube issue, with all data previously reported remaining accurate. Comparisons between 2022 and 2023 tests will be limited accordingly in this report.

For reference, all ice accretion tests were conducted with target airspeeds of 150 and 200 knots. Most aerodynamic tests were conducted at target airspeeds of 100, 150, and 200 knots, with a select few test points conducted at 50 knots. Figures and tables in the following sections will be displayed with the corrected airspeed.

TABLE 1.—TARGET AIRSPEEDS COMPARED TO APPROXIMATE CORRECTED AIRSPEEDS, AS A REFERENCE

Target, U, knots	Approximate corrected, U, knots
50	50.0
100	100.5
150	152.5
200	207.0

4.0 Aerodynamic Tests

4.1 Aerodynamic Test Objectives and Test Conditions

Multiple objectives where set for the aerodynamic tests to help characterize surface flow around the SIDRM test article and are listed below.

- Assess the impact of an air gap between the test article and the test section ceiling (approximately 0.5 in. gap).
- Conduct a series of AOA sweeps at various airspeeds to understand the parameter impact on surface pressure and flow characteristics.
- Compare aerodynamic measurements against SIDRM tests conducted in 2022 to assess repeatability.
- Conduct tests that pinpoint the stagnation line at the leading edge.

Aerodynamic tests conducted in 2022 were performed utilizing 1° AOA intervals. Because the model was symmetric, the stagnation line was expected to be at the leading edge highlight location at 0° *AOA*. However, the aerodynamic data from 2022 suggested that the stagnation line formed at the leading edge highlight was not at 0° *AOA*, but at an angle between 0° and 1°. Aerodynamic tests conducted in 2023 were performed with smaller AOA intervals around 0° *AOA* to zero-in on the AOA that put the stagnation line at the leading-edge highlight of the model. Table 2 shows the *AOA* sweeps conducted at different airspeeds, *U*. The total air temperature was held constant for all aerodynamic test runs at T_0 = 5 °C.

The pressure coefficient, C_p, (nondimensional) was calculated from experimental measurements. Equation (1) shows the pressure coefficient expression where P_{tap} is the surface pressure as measured by the built-in pressure taps, P_s is the freestream static pressure, and P_0 is the total pressure. Total and static pressure measurements were made by pitot-static probes located at the beginning of the constant area test section.

$$C_p = \frac{P_{tap} - P_s}{P_0 - P_s} \tag{1}$$

4.2 Ceiling Gap Flow Impact Investigation

The SIDRM test article was purposely designed and constructed to not span the full height of the IRT test section. This is standard practice to ensure that the test article fits when installed. A foam cut-out that matches the contour of the test article was placed in the gap to ensure full uniform flow around the test article. For the initial entry in 2022 the foam cut-out extended the entire chord length, however the aft portion of the cut-out was difficult to contain in the gap during testing. Tests were ultimately conducted with just the forward portion of the foam cut-out installed in the gap that extended from the leading edge portion of the cut-out was difficult to contain in the gap during testing. Tests were ultimately conducted with just the forward portion of the foam cut-out installed in the gap that extended from the leading edge to approximately 25% of the chord. This same forward portion foam cut-out was used in the 2023 test entry. Figure 6 shows the foam cut-out inserted in the gap and its chordwise extent.

TABLE 2.—TEST CONDITIONS FOR THEAERODYNAMIC CHARACTERIZATION RUNS

T_0, °C	*U*, knots	*AOA*, °
5	50.0	0.0, 4.0
5	100.5	–0.8, –0.6, –0.4, –0.2, 0.0, 0.1, 0.2, 0.4, 1.0, 2.0, 3.0, 4.0
5	152.5	–0.4, –0.2, 0.0, 0.2, 0.3, 0.4, 1.0, 2.0, 3.0, 4.0
5	207.0	–0.4, –0.2, 0.0, 0.2, 0.3, 0.4, 0.6, 1.0, 2.0, 3.0, 4.0

Figure 7 shows pressure coefficient values plotted against normalized chord length, where each graph compares pressure tap measurements between the lower and upper rows. *AOA* values of 0° (Panels (A) to (C)) and 4° (Panels (D) to (F)) are shown at $U = 100.5$, 152.5 and 207 knots. The figure shows that there is good matching between the lower and upper tap row pressure measurements for the forward 30% of the chord for all angles of attack and airspeeds. This coincides with where the foam cutout exists to fill the gap between the test article and the ceiling, likely aiding in uniform measurement between the rows for the forward 30%. Noticeable deviations occur between the tap row measurements starting at $z/c = -0.4$, and likely an influence of the ~0.5-in. gap at the ceiling. The C_p peak at $z/c = -0.4$ is lower for the upper row of taps, suggesting some air flows towards the gap, resulting in slower flow for the upper portions around the maximum thickness of the SIDRM test article as compared to the lower portion.

Also of note, in Figure 7 is that there are asymmetric pressure measurements that occurred in the aft portion of the test article for the lower tap row between the instrumented and non-instrumented sides at *AOA* = 0°. This lower tap row asymmetry becomes greater as airspeed increased (Panels (B) and (C)). Symmetric measurements are expected at *AOA* = 0°. More study is needed to verify, but a few hypotheses are posited. Physical inspection of the test article showed that the geometry was within tolerance of geometry design. However, the inspection occurred in an ambient environment (no flow), and it is possible that the fiberglass extension panels in which these pressure taps were located may have flexed under aerodynamic loads, and geometric asymmetries may have resulted. In addition, the bottom fiberglass extension panels were removed for test article installation in the IRT test section. A second hypothesis is that there is asymmetric airflow that develops in the closed-loop tunnel, in particular with the relatively thick test article (21.68 in. at maximum thickness) installed in the 108-in. wide test section. The upper tap row pressure measurements maintain symmetry along the entire chord for all airspeeds at *AOA* = 0°, suggesting that the ceiling gap helps equalize any pressure differences between the two sides due to any flow or geometry asymmetries that may exist.

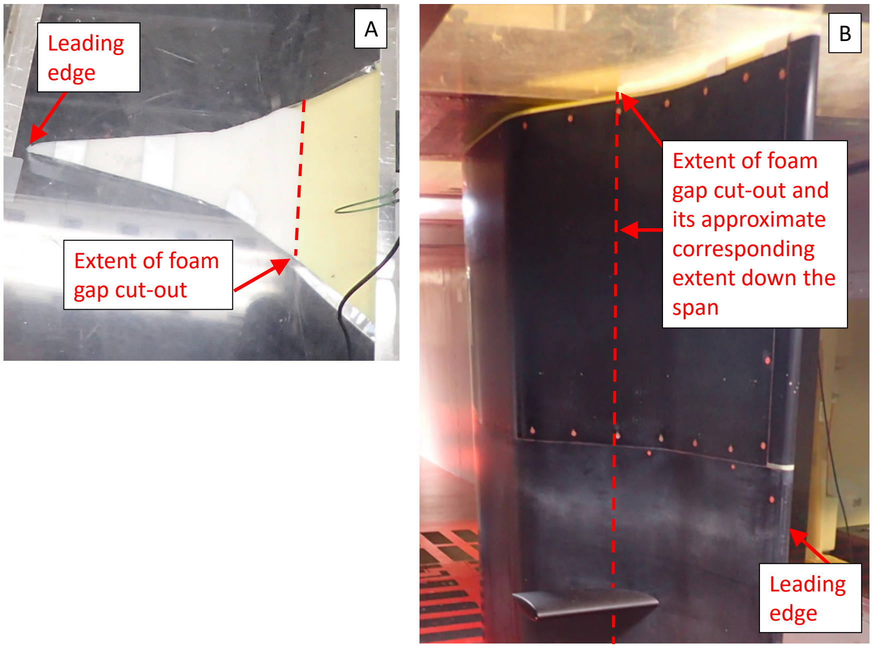

Figure 6.—Images showing the extent of the foam cutout to fill the ~0.5-in. gap between the SIDRM test article and the ceiling as viewed (A) from above the plexiglass ceiling and (B) from inside the test section.

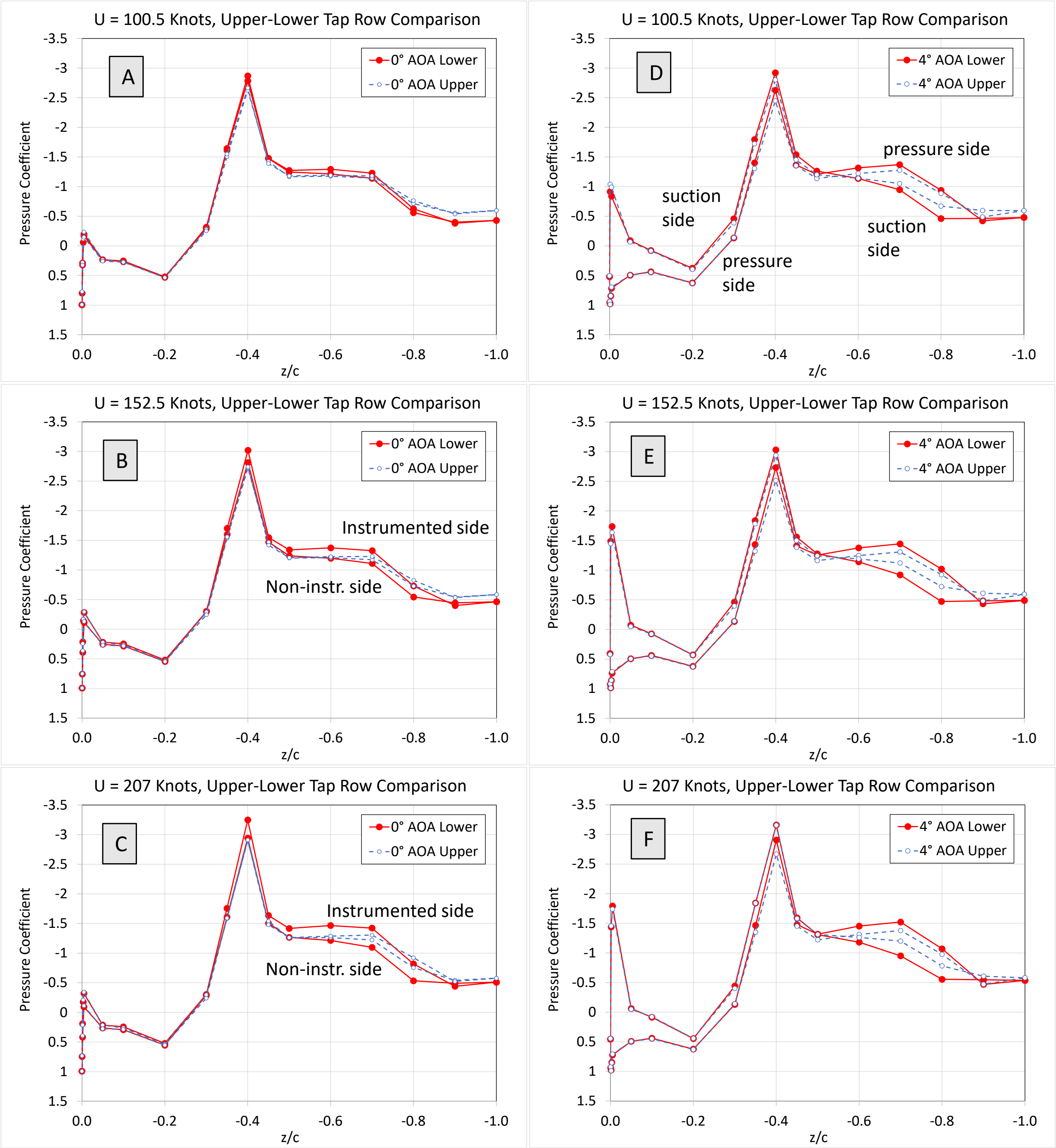

Figure 7.—Comparison of pressure coefficient values versus normalized chord length for the upper and lower tap rows. Values are provided at *AOA* = 0° (A) to (C) and 4° (D) to (F) for airspeeds of *U* = 100.5, 152.5, and 207 knots.

Despite some aerodynamic irregularities, the forward portion of the test article shows good surface pressure symmetry at *AOA* = 0°, and good agreement between the upper and lower tap rows for all aerodynamic tests conducted. The forward surfaces encounter favorable pressure, whereas the aft surfaces encounter adverse pressure which is unfavorable and susceptible to impacts of separation. The foam cutout aided good forward aerodynamic measurements, which is the focus of all icing tests, and it is believed that icing was not impacted by any aerodynamic irregularities that occurred on the aft portions due to the ceiling gap.

4.3 Angle of Attack and Airspeed Sweeps

Figure 8 shows pressure coefficient values plotted against normalized chord length for various angles of attack at airspeeds of *U* = 100.5, 152.5, and 207 knots. Both lower (Panels (A) to (C)) and upper (Panels (D) to (F)) tap row measurements are provided. The 1° AOA increments show how measured surface pressures were impacted. The C_p increasingly became more negative on the suction side near the leading edge as *AOA* increased, indicating a local increase in air speed around the leading edge surface. A stagnation value of $C_p = 1$ occurred near the leading edge and will be explored more in Section 4.5. The location of maximum test article thickness occurs at $z/c = –0.42$. The spike in C_p that occurs at $z/c = –0.4$ for each graph corresponds to the tap nearest this maximum thickness and indicates the chord location where airspeed is greatest.

Of note in Figure 8 is that at a positive AOA the lift generated at the front half of the test article is countered by negative lift on the aft half. In the forward half, the upper curves represent the suction side, the lower curves represent the pressure side (see pressure and suction descriptions written in Figure 8(A)). Integrating the difference between the two provides the amount of positive lift (an upward force) generated by the forward half. In the aft half, the upper curves represent the pressure side, the lower curves the suction side. The integrated difference now produces negative lift (a downward force) on the aft half. These countering forces act to effectively rotate the test article around its center axis. These countering forces become greater as *AOA* increases. It should be noted that the SIDRM geometry was not designed to be an efficient lifting surface but intended to investigate icing on the forward portion of the test article, where nonzero *AOA* tests, in part, provide data on collection efficiency shadow and concentration regions.

Flow separation occurred towards the trailing edge, where *AOA* impacted the location of flow separation. Figure 8(C) provides the clearest example where flow separation was measured at $z/c = –0.8$ for the suction side but was still attached on the pressure side at this chord location. Flow separation occurred farther aft on the pressure side at $z/c = –0.9$. For positive *AOA*, flow separation was likely delayed until farther down the chord due to the favorable pressure gradient keeping the flow attached on the pressure side.

As was mentioned in Section 4.2, differences are again noticeable between the upper and lower pressure tap row measurements for the aft portion of the test article in Figure 8. This reinforces how the ceiling gap that exists towards the aft portion of the test article likely accounts for the differences. For the lower tap row, there is a deviation in C_p between the suction and pressure sides as *AOA* increases, but that difference is washed out for the upper row of taps. Some air flow towards the ceiling gap likely accounts for this C_p washing out effect. In addition, flow separation is delayed in the upper tap row on the suction side ($z/c = –0.9$) compared to the lower tap row ($z/c = –0.8$). To reduce the number of graphs displayed, only the lower pressure tap row will be provided for the remaining figures in this section. The lower pressure tap row represents a truer pressure flow profile where flow is constrained by the floor and is 2-dimensional (2D), unlike the upper tap row where some air flows laterally towards the ceiling gap and flow is unintentionally 3-dimensional (3D) towards the aft portion of the test article.

Figure 9 shows pressure coefficient measurements of the lower pressure tap row for two airspeed sweeps to more easily identify its impact on aerodynamics. Panels (A) and (B) show airspeed sweeps at *AOA* = 0 and 4°, respectively. In both graphs, the continuously decreasing value of C_p (more negative) at $z/c = –0.4$ with increasing airspeed is due to Reynolds number effect ($\mathrm{Re} = 1\times10^6$ to 5×10^6) (Ref. 53). Greater momentum from faster airspeeds pushes the location of separation farther downstream, which in turn aids airspeed and affects C_p upstream at the model's thickest width.

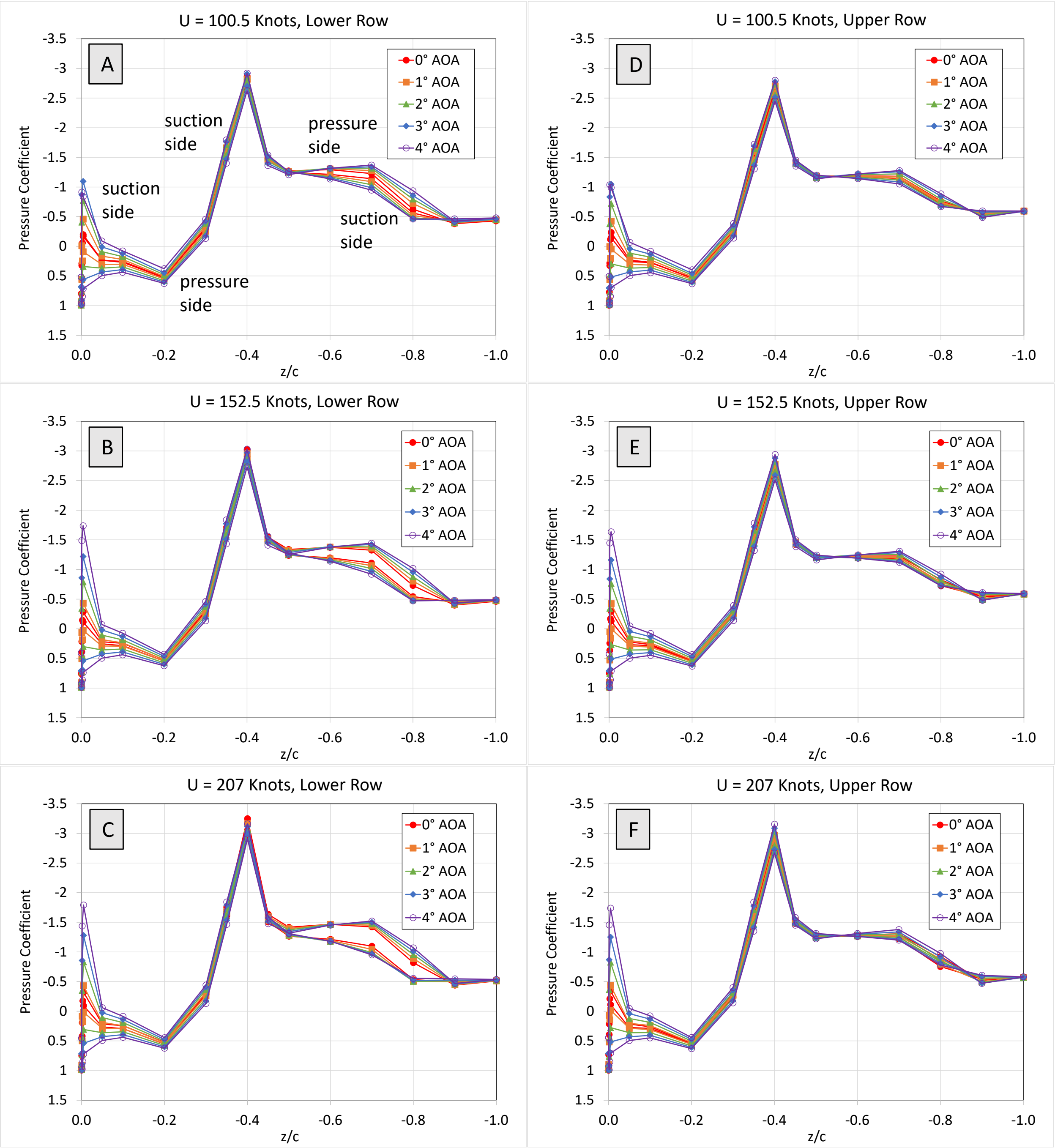

Figure 8.—Pressure coefficient values versus normalized chord length for angles of attack that range from *AOA* = 0 to 4° for airspeeds of *U* = 100.5, 152.5, and 207 knots. Both lower (A) to (C) and upper (D) to (F) tap row values are provided.

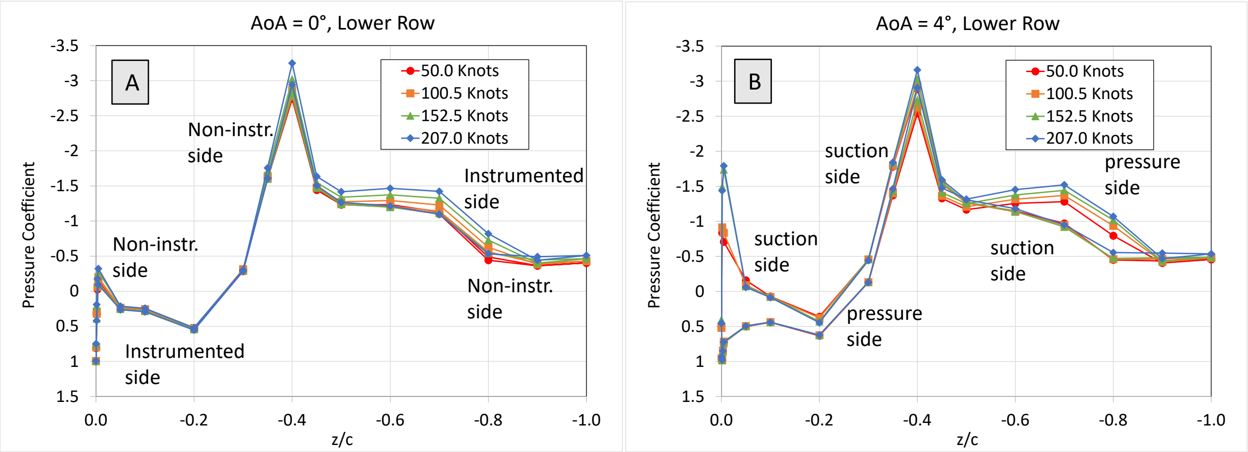

Figure 9.—Pressure coefficient values versus normalized chord length for velocity sweeps at angles of attack at *AOA* = 0 and 4°.

In the *AOA* = 4° graph, the C_p increasingly became more negative on the suction side near the leading edge as *U* increased. This shows that there is a local increase in air speed around the leading edge surface, as negative C_p values indicate air flow speeds greater than far-field airspeed.

Figure 9(A) shows that there are asymmetric pressure measurements that occurred in the aft portion of the test article between the instrumented and non-instrumented sides, despite *AOA* = 0°. This asymmetry becomes greater as airspeed increases. This reiterates and highlights the asymmetric measurements at *AOA* = 0° discussed in Section 4.2.

4.4 Comparison of 2023 to 2022 Measurements

Aerodynamic measurements acquired during the 2023 SIDRM tests are compared against those from the 2022 tests in Figure 10. During the 2023 tests, conditions were set with the intention of determining repeatability between the two test entries. As noted in Section 3.0, reference pressure issues that were only identified after testing was completed resulted in greater than intended airspeeds. These airspeed differences are noted in each graph in the figure. Despite airspeed differences, comparisons are made to evaluate repeatability and understand how small airspeed differences might impact pressure measurement.

Figure 10 shows pressure coefficient values plotted against normalized chord length for *AOA* = 0 and 4° where the target airspeeds were *U* = 100, 150, and 200 knots. The corrected airspeeds for tests conducted in 2023 are shown in the graphs. For perfect repeatability, the solid red curve would be plotted precisely on top of the dashed red curve, for example. The best repeatability occurs at the slowest target speed, and greater deviations occur at the two faster target airspeeds. At the lowest target airspeed, the differences in actual airspeed are negligible (*U* = 100 vs. 100.5 knots) and provides the best repeatability comparison. The actual airspeeds differ more significantly for the fastest target airspeed (*U* = 200 vs. 207 knots) and may be the reason for the poorer repeatability comparison. Despite any actual airspeed differences, the forward portion of the test article showed better repeatability (curves more closely plotted on top of each other) than the aft portion. This is favorable as ice accretion tests largely focus on the forward portion of the test article.

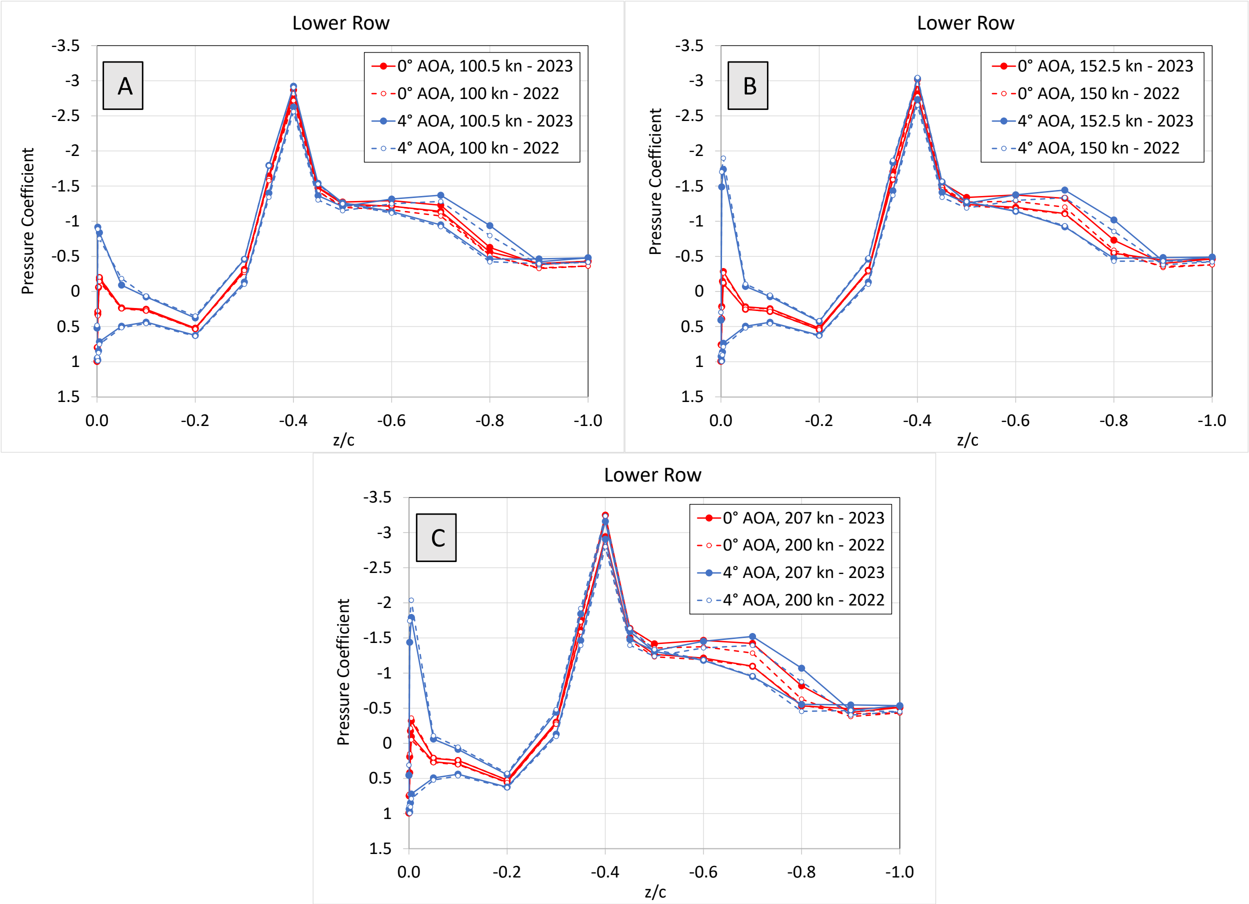

Figure 10.—Pressure coefficient values versus normalized chord length, comparing 2022 and 2023 measurements for *AOA* = 0 and 4° where the target airspeeds were *U* = 100, 150, and 200 knots. The corrected airspeeds for tests conducted in 2023 are shown in each graph.

4.5 Stagnation Point Inspection

Figure 11 shows pressure coefficient values plotted against the unwrapped distance (s) near the leading edge for *AOA* sweeps at three airspeeds to identify the stagnation line at the leading edge. The *AOA* at which the stagnation line occurs at the test article leading edge is plotted as a dashed black curve for each airspeed in Figure 11. This is identified as the curve where C_p curve is most symmetric about the leading edge (s = 0 in.). For the slowest velocity at U = 100.5 knots, the stagnation line occurred at *AOA* = 0.1°. For airspeeds of 152.5 and 207 knots, the stagnation line at the leading edge occurred at *AOA* = 0.3° for both airspeeds. This means for tests runs that were conducted at *AOA* = 0.0°, the instrumented side of the test article experienced a slightly greater positive pressure. It is not clear what is the cause of the nonaligned flow. It is possible that there is a slight angularity in the flow due to circulation in the closed loop tunnel or that the turntable is not perfectly aligned with the tunnel walls. These positive *AOA* values are in line with aerodynamic data collected during the 2022 SIDRM tests where the stagnation line was identified to exist at an angle between 0° and 1°. This slight misalignment is not expected to impact ice accretions in any significant manner.

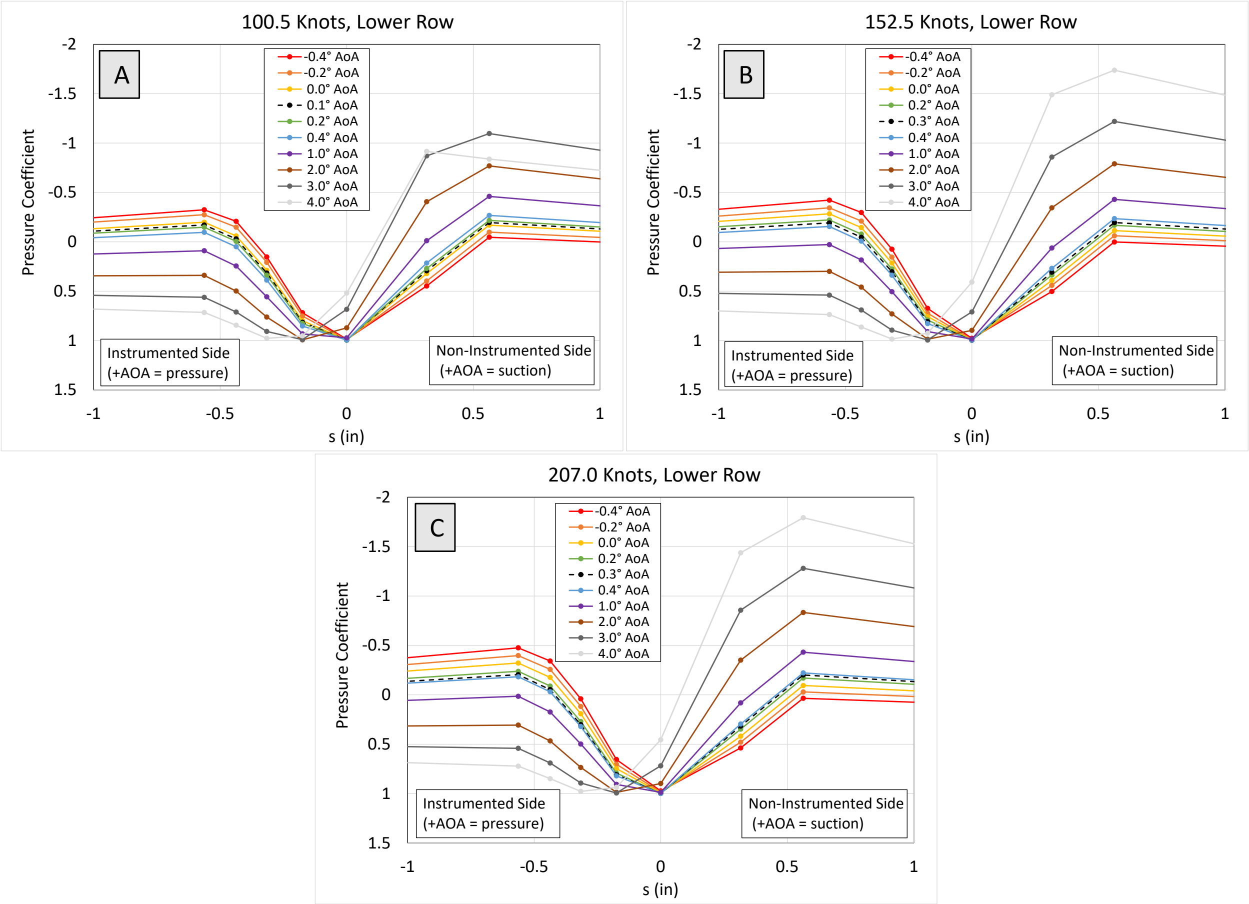

Figure 11.—Pressure coefficient values versus unwrapped distance near the leading edge for *AOA* sweeps at airspeeds of (A) 100.5 knots, (B) 152.5 knots, and (C) 207.0 knots.

5.0 Supercooled Liquid Icing Tests

5.1 Supercooled Liquid Icing Test Objectives and Test Matrix

Supercooled liquid icing tests were conducted as they provide simulation validation data on a 3D geometry. Multiple objectives where set for these ice accretion tests and are listed below.

- Conduct various parameter sweeps (T_0, spray duration time, *MVD*, and *AOA*) to measure that parameter's impact on ice accretion size/mass, location, and characteristics (such as glaze/rime ice and shedding behavior).
- For the T_0 parameter sweep, conduct test runs with 1 °C increments between $T_0 = –3$ and –6 °C, to more closely evaluate the glaze-rime ice transitioning regime.
- For the *AOA* parameter sweep, conduct a test run at *AOA* = 0.35°. This is the angle that was preliminarily determined during aerodynamic testing where the stagnation line occurred at the SIDRM leading edge. The ice accretion can be compared to the test run where *AOA* = 0.0°. After post-processing the data, the stagnation line was determined to be *AOA* = 0.30° for 152.5 and 207 knots. This is sufficiently close for comparison purposes.
- Conduct rime ice tests allowing for a first order estimate of collection efficiency that can be calculated from rime ice accretion geometry.

- Conduct repeat test runs to quantify repeatability.
- Conduct supercooled liquid icing tests that repeat test conditions that were performed during the SIDRM 2022 test entry. Whereas the strut geometry and strut locations were different between the two test entries, and slight differences in *U* and *LWC* exist due to the reference pressure issues discussed in Section 3.0, comparisons can provide insight into tunnel repeatability.

Twenty-three supercooled liquid ice accretion test runs were conducted during the 2023 test entry. Table 3 shows the test conditions (corrected for reference pressure issue) in Columns 1 to 7 and resulting accretion mass in Columns 8 to11. Table 3 is ordered in blocks according to the five parameter sweeps conducted: total air temperature, time duration at rime ice conditions, time duration at glaze ice conditions, *MVD*, and *AOA*. Positive AoA values mean that the test article was rotated in the direction that made the instrumented side the pressure side. Unique test runs are identified by their test run ID (i.e., UG no.). In the table, liquid water content is noted as *LWC*. Drop size distributions for the supercooled liquid clouds used for ice accretion tests are provided in Table A.7 in the Appendix. The static relative humidity is approximated to be saturated at the test section for this atmospheric wind tunnel (i.e., the total pressure is about 1 atm) as an equilibration spray was performed at the start of each day of testing. Four test points were repeated to provide a measure of repeatability (e.g., UG3582 and UG3631 in the total air temperature sweep).

5.2 Testing Procedures—Scanning and Weighing of Ice Mass

The testing procedures for the supercooled liquid ice accretion tests are outlined below.

1. Run up IRT to target test airspeed and air temperature.
2. Start recording data 30 s prior to spray activation.
3. Turn on icing cloud (spray on).
4. Turn off icing cloud per the time specified on the test matrix.
5. Continue holding tunnel airspeed and air temperature constant as data systems continue recording 30 s post spray.
6. Stop data recording systems and shut down drive fan.
7. Enter test section and take photographs of accreted ice.
8. Perform 3D scan of mid 10-in. span of accreted ice.
9. Break off strut ice and place into pan for weighing.
10. Using heated knife, cut out mid 8-in. span of accreted ice on casing and scrape ice into tray for weighing.
11. Remove all ice from SIDRM and clean test article, preparing for next test point.

The primary measurements to assess supercooled liquid ice accretion size were 3D laser scans of the final ice accretion and weighing of the accreted ice. The accreted ice geometry was measured after each test run utilizing a 3D laser scanner. Hexagon's Romer Absolute SI 7530 scanner was used and has a repeatability accuracy of ± 0.003 in. The center 10-in. (0.25-m) span was scanned from the leading edge to the extent of ice on either side of the test article, including the struts. Figure 12(A) depicts the area that was scanned with resulting 3D image of the ice accretion in the bottom right of the panel. After scanning, ice that had accreted on each of the struts was carefully removed for weighing (Panel (B)). Then the center 8-in. (0.20-m) span of accreted ice on the casing was cut from the leading edge to the extent of icing on both sides, removed, and weighed (Panel (C)). The ice mass measurements for the strut on the instrumented side, the strut on the non-instrumented side, the casing, and the combined total ice mass are provided in Columns 8 to 11 in Table 3.

TABLE 3.—TEST CONDITIONS (CORRECTED) FOR DIFFERENT PARAMETER SWEEPS CONDUCTED FOR THE SUPERCOOLED LIQUID ICING TEST RUNS, ALONG WITH FINAL ACCRETED ICE MASS MEASURED AT VARIOUS LOCATIONS

Test run conditions							Accreted ice mass measurements			
Column 1 Test Run, ID no.	Column 2 Spray duration, min	Column 3 T_0, °C	Column 4 *U*, knots	Column 5 *AOA*, °	Column 6 *MVD*, µm	Column 7 *LWC*, g/m^3	Column 8 Instrument side strut, g	Column 9 Non-instrument side strut, g	Column 10 Casing, g	Column 11 All ice, g
T_0 sweep										
UG3583	20	–3	152.5	4	25	0.49	180	178.2	415	773.2
UG3584	20	–4	152.5	4	25	0.49	169	190.6	417	776.6
UG3585	20	–5	152.5	4	25	0.49	167.7	182.2	453	802.9
UG3582	20	–6	152.5	4	25	0.49	173.5	190.5	470	834
UG3631	20	–6	152.5	4	25	0.49	156.5	170.9	475	802.4
UG3586	20	–9	152.5	4	25	0.49	172	196	516	884
UG3604	20	–12	152.5	4	25	0.49	172.2	183.3	540	895.5
UG3605	20	–17	152.5	4	25	0.49	172	187.5	583	942.5
Spray duration time sweep—Rime ice										
UG3587	5	–17	152.5	0	30	0.44	36.8	37.7	189	263.5
UG3619	5	–17	152.5	0	30	0.44	35.8	35.9	189	260.7
UG3588	10	–17	152.5	0	30	0.44	78.8	83.1	392	553.9
UG3613	15	–17	152.5	0	30	0.44	122.2	127.1	545	794.3
Spray duration time sweep—Glaze ice										
UG3633	5	–6	152.5	4	25	0.49	32.5	34.6	126	193.1
UG3632	10	–6	152.5	4	25	0.49	70.2	73.1	240	383.3
UG3582	20	–6	152.5	4	25	0.49	173.5	190.5	470	834
UG3631	20	–6	152.5	4	25	0.49	156.5	170.9	475	802.4
MVD sweep—Rime ice										
UG3615	3.5	–17	207	4	18	0.44	28.3	29.1	115	172.4
UG3590	3.5	–17	207	4	30	0.44	34.3	33.3	165	232.6
UG3634	3.5	–17	207	4	30	0.44	33	33.5	161	227.5
UG3608	3.5	–17	207	4	50	0.44	35.8	37.5	245	318.3
UG3607	3.5	–17	207	4	90	0.44	38.7	40.2	315	393.9
UG3635	3.5	–17	207	4	90	0.44	38.9	39.5	332	410.4
AOA sweep—Rime ice										
UG3589	3.5	–17	207	0	30	0.44	33.6	34.1	181	248.7
UG3616	3.5	–17	207	0.35	30	0.44	34.0	33.5	187	254.5
UG3606	3.5	–17	207	2	30	0.44	33.6	34.2	175	242.8
UG3590	3.5	–17	207	4	30	0.44	34.3	33.3	165	232.6
UG3634	3.5	–17	207	4	30	0.44	33.0	33.5	161	227.5

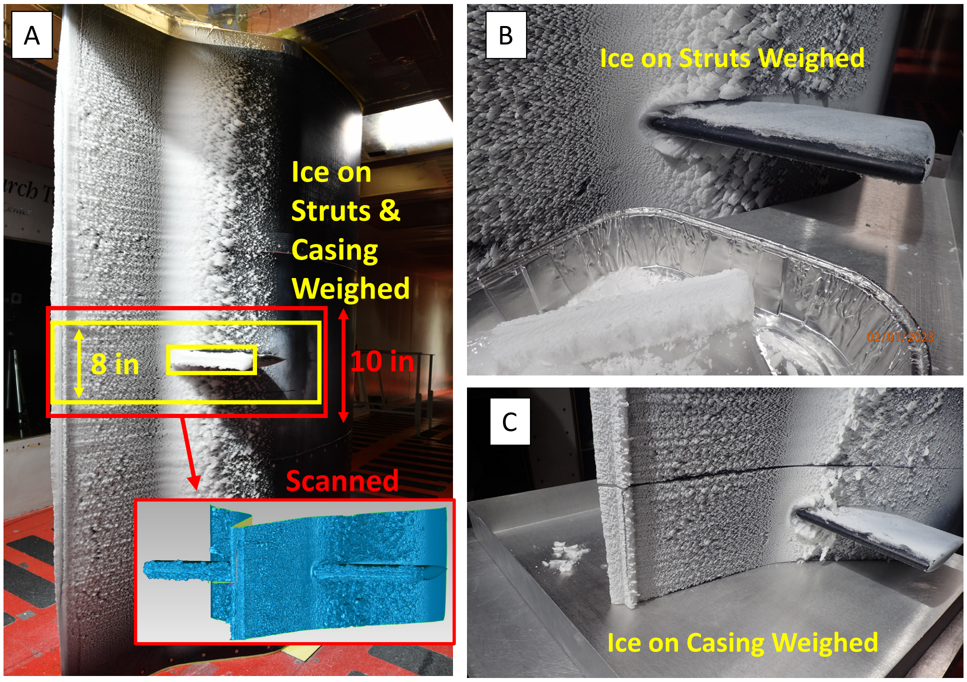

Figure 12.—Images describing (A) the locations that ice was scanned and weighed, with examples showing the process of (B) strut ice being removed for weighing and (C) casing ice being cut ready to be removed into a pan for weighing.

5.3 Total Air Temperature Sweep

A total air temperature sweep was conducted that ranged from glaze to rime ice as T_0 decreased. Figure 13 shows sample images of a glaze ice accretion conducted at $T_0 = -3$ °C shown in Panel (A) and a rime ice accretion conducted at $T_0 = -17$ °C in Panel (B). The accreted ice is partially transparent in the glaze test, and opaque in the rime test case. The insets show the non-instrumented side ice accretion on the struts, where the glaze condition resulted in a horn ice shape, and the rime condition resulting in an aerodynamic pointed ice shape. The total ice mass increased as T_0 decreased as can be seen in the final column of Table 3 for the T_0 sweep. Time lapse video shows continuous shedding of feathers near the ramp top for all test runs, but earlier and more shedding occurred for warmer tests and may account, in part, for the difference in final ice mass that was measured. The greater shedding amounts may be a result of weaker ice cohesion strength compared to colder accretions and feather accretions experiencing more drag due to accretion shape and size. Repeat test runs conducted at $T_0 = -6$ °C resulted in about 4% difference in total ice mass.

Figure 14 shows cross-sections of the accreted ice at the center-span for the air temperature sweep. Panel (A) shows the overall view, whereas Panels (B), (C), and (D) show zoomed-in cross sections at the leading edge, instrumented side strut (pressure side), and non-instrumented side strut (suction side), respectively. To avoid repeating descriptions of this figure layout again, each of the remaining subsections in this section (Section 5.0) will have the same figure layout presented. The transition from horn-shaped to streamline shaped ice accretions is evident at the leading edge (Panel (B)) as air temperature decreases, characteristic of the transition from glaze to rime ice. The size of the horn shape reduced as T_0 decreased in 1 °C decrements between $T_0 = -3$ and –6 °C in Panel (B). The tests were run at $AOA = 4°$, so the accretions at the leading edge lean towards the pressure side (to the left in Panel (B)). Panels (C) and (D) show evidence

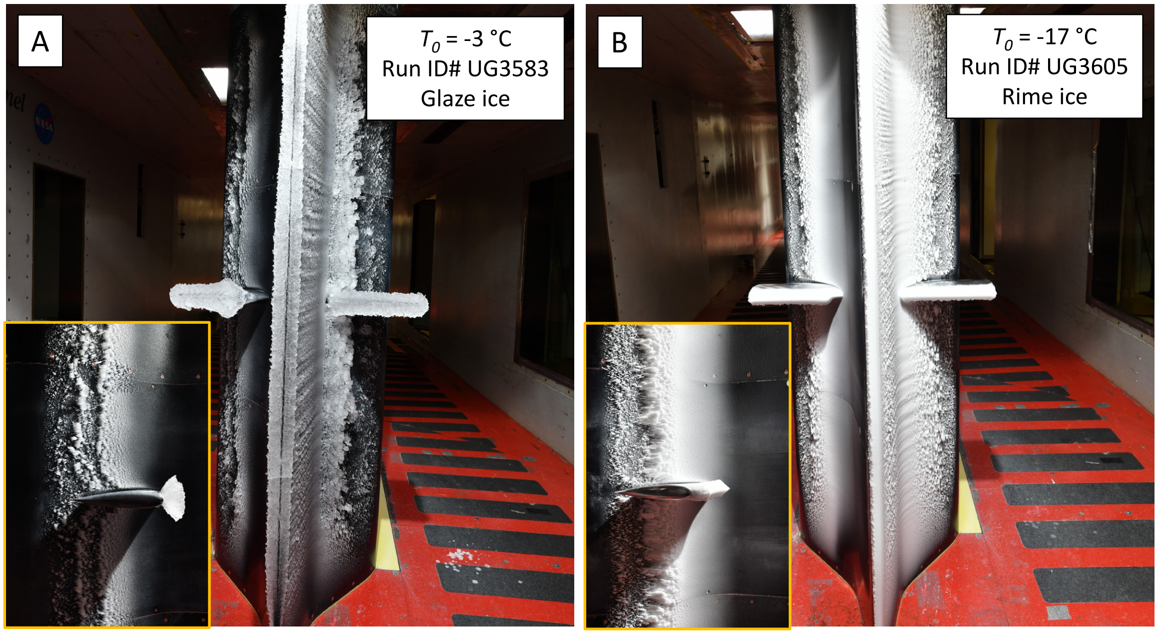

Figure 13.—Images of (A) a glaze ice accretion conducted at T_0 = –3 °C and (B) a rime ice accretion conducted at T_0 = –17 °C.

of shadow and concentration regions near the strut junction. Looking at the pressure side (Panel (C)), the shadow region is small and is likely a result of the boundary layer created by the main body upstream of the struts. The shadow and concentration regions of the impinging cloud are more prominent on the suction side (Panel (D)) as the main body at an AoA blocks and impacts cloud flow to the strut downstream at *AOA* = 4°. The horn ice accretions on the main body leading edge from the warmer test runs appear to have expanded the shadow region on both struts nears the junction. Panel (C) (pressure side) shows that the concentration region for the T_0 = –3 °C test run occurred around y = –4 in., which is further outboard than the T_0 = –17 °C test run which occurred around y = –3.5 in. Similarly, Panel (D) shows that the concentration region for the T_0 = –3 °C test run occurred around y = 6 in., which is further outboard than the T_0 = –17 °C which occurred around y = 4.5 in. Of note in Panel (B) is that just aft of the leading edge, there is little to no ice on the casing on the suction side, until just aft of the strut where the casing geometry becomes more exposed to the impinging cloud. Panels (B) and (C) show that there is ice accretion on the pressure side of the casing from the leading edge to the struts.

Figure 15 shows cross-sections of strut leading edge ice accretions at various locations on both struts for the air temperature sweep. Panels (A) and (B) show cuts 3.5 in. from the SIDRM center, near the strut and main body junction (inboard) for the instrumented and non-instrumented side struts, respectively. Panels (C) and (D) show cuts 8.0 in. from the test article center, further out into the freestream (outboard) for the instrumented and non-instrumented side struts, respectively. A diagram is inset in Panel (B) to provide spatial reference of the four cross-section cuts at the struts. To avoid repeating lengthy descriptions of this figure layout again, each of the remaining subsections in this section (Section 5.0) will have the same figure layout presented. Panels (A) and (B) highlight the impact of shadow regions near the strut junction created by the *AOA* = 4° test runs with little to no ice accretion on the suction side (Panel (B)). The cross sections in Panel (A) (pressure side) show accretions at the strut junction, which captured ice accretion on the strut leading edge and ice that accreted on the main body. Further outward on the struts, Panels (C) and (D) show the transition from horn-shaped glaze ice to more streamlined rime ice accretions as T_0 decreases.

The accretions on the suction side in Panel (D) are larger than on the pressure side in Panel (C). In addition, despite the sizeable shadow region created by the main body at AOA = 4°, accretion mass was greater for the suction side strut than the pressure side strut for all temperatures conducted in the sweep except for $T_0 = -3$ °C where they were nearly equal (see Columns 8 and 9 from Table 3). This may, but only in part, be a result of how the ice was removed from the struts. For the suction side, the growth and removal of ice from the strut was clear and distinct as there was little to no ice at the strut junction interface as can be seen in Figure 14(D). For the pressure side, there was significant ice growth near the strut junction and therefore there was no clear and distinct cutoff for the strut ice. When the accreted ice on the strut was broken off by hand, the break naturally occurred at its weakest and thinnest point at the junction. An example of the remining ice at the junction can be seen in Figure 12(B). Some measurement variation in strut ice mass will exist where there is ice at the strut junction, in particular for long spray duration tests like these 20-min tests for the T_0 sweep. However, this likely does not fully account for the strut ice mass differences as the suction side accreted ice geometry is noticeably larger than the pressure side for outboard regions of the strut.

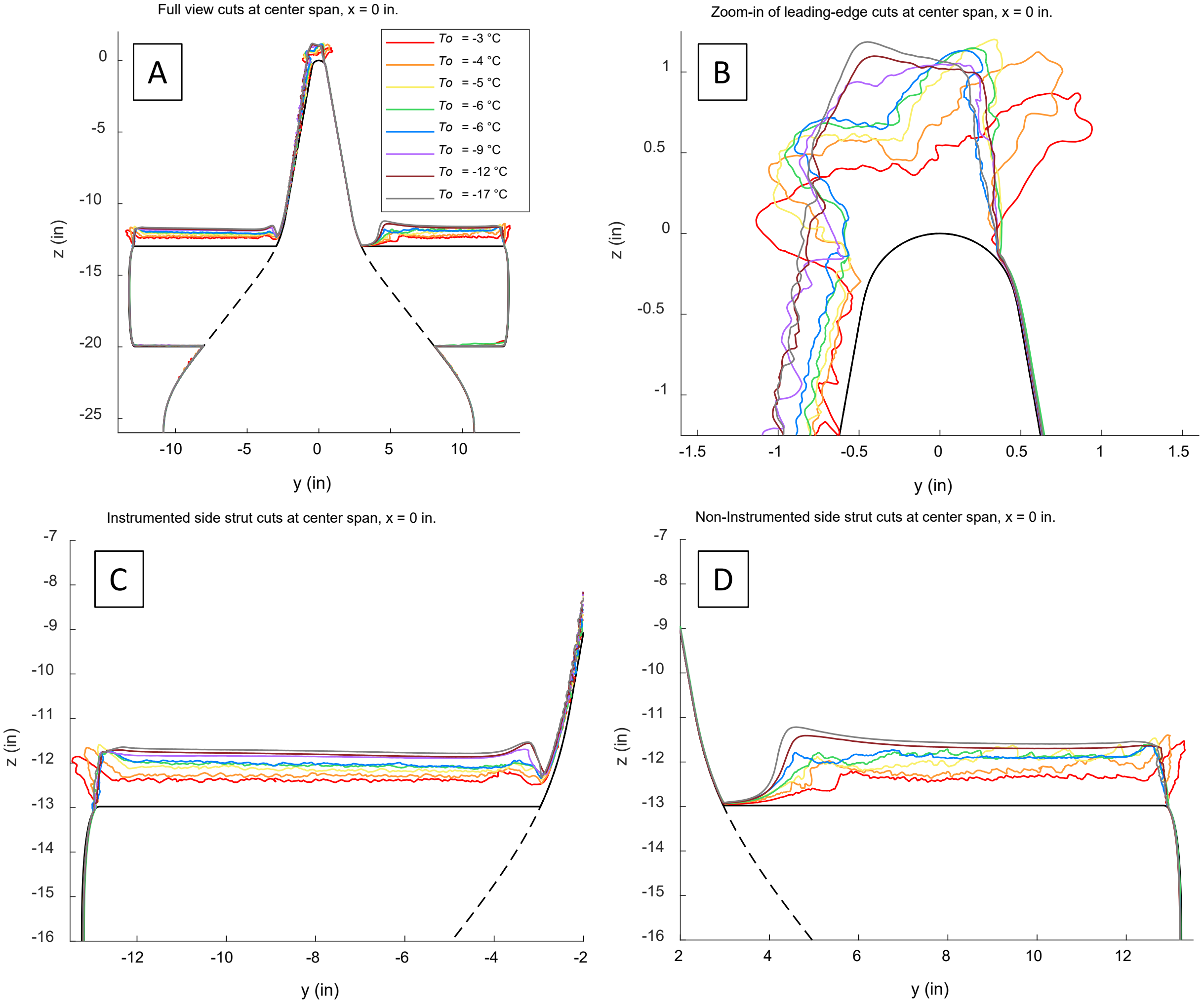

Figure 14.—Cross-sections of the accreted ice at the center-span for the T_0 sweep. Panel (A) shows the overall view, whereas Panels (B), (C), and (D) show zoomed-in cross sections at the leading edge, pressure side strut, and suction side strut, respectively.

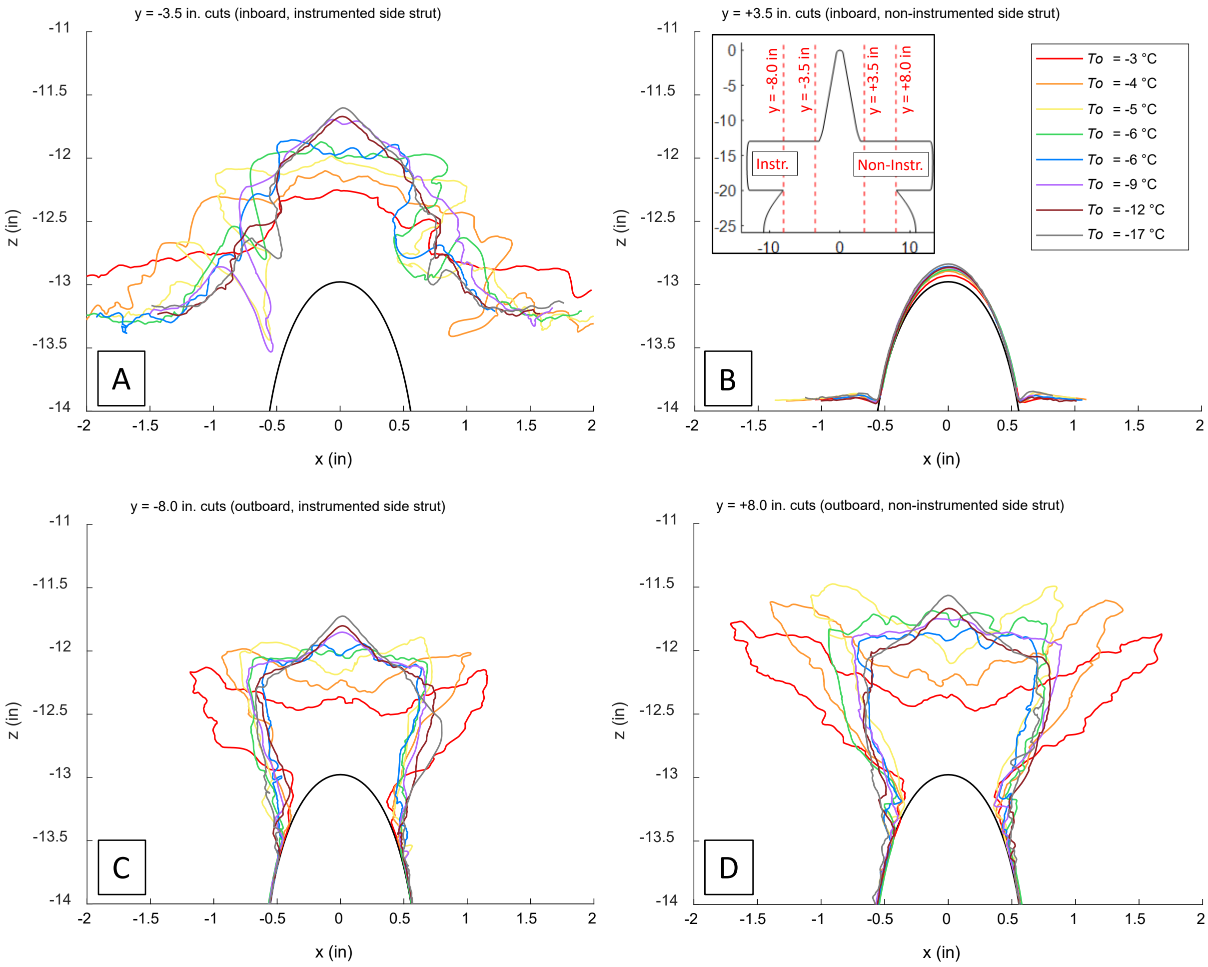

Figure 15.—Cross-sections of strut leading edge ice accretions at inboard (A) and (B) and outboard (C) and (D) locations on both struts for the T_0 sweep.

Multiple test points were repeated from the SIDRM 2022 test entry for the T_0 sweep. Table 4 compares accreted ice mass between the 2023 and 2022 SIDRM test entries. The ice mass from both struts is combined for this comparison. Dashes in the 2022 test entry represent test points that were not conducted or where ice mass not fully measured. As a reminder, due to the reference pressure issue, there are small differences in U and LWC between the two test entries. Airspeed was U = 152.5 knots for 2023 and U = 150 knots for 2022. In addition, LWC = 0.49 g/m^3 for 2023, and LWC = 0.50 g/m^3 for 2022. These are small and are not expected to significantly impact overall measurement. An additional reminder is that larger struts were utilized in the 2023 test entry (7-in. chord NACA 0018 for 2023 and 4-in. chord NACA 0012 for 2022). As a result, Table 3 shows that the 50% wider struts from the 2023 tests accreted about 50% more ice compared to the 2022 tests, as the wider struts captured more impinging cloud droplets. Comparing the accreted ice mass on the casing, approximately 2% lower mass was measured for the 2023 tests, except for the warmest test case. The LWC for 2023 was 2% lower than the 2022 entry, but with the increased airspeed, the overall cloud mass flow rate is constant between the two test entries. It is instead hypothesized that the slightly lower ice mass measurements in 2023 may be due to more droplets that impinged on the larger struts instead of the casing further aft of the struts. The impingement on the casing around the struts is low as the cloud flow is shallow (nearly parallel) with the test article surface geometry, resulting in a small 2% difference between the test entries.

TABLE 4.—COMPARISON OF ACCRETED ICE MASS ON THE STRUTS AND CASING BETWEEN THE 2023 AND 2022 SIDRM TEST ENTRIES FOR THE T_0 SWEEP

T_0 °C	2023		2022	
	Ice mass both struts, g	Ice mass casing, g	Ice mass both struts, g	Ice mass casing, g
–3	358.2	415	----	394
–4	359.6	417	----	----
–5	349.9	453	----	----
–6	364.0	470	241	479
–6	327.4	475	241	479
–9	368.0	516	239	526
–12	355.5	540	238	551
–17	359.5	583	224	595

5.4 Spray Duration Time Sweep—Rime Ice Conditions

A spray duration time sweep was conducted under rime ice conditions ($T_0 = -17$ °C) where spray time ranged from 5 to 15 min. Figure 16 shows sample images of ice accretion for a spray duration of 5 min shown in Panel (A) and 15 min in Panel (B). The accreted ice is opaque for both rime test case. The insets show the instrumented side ice accretion on the struts, where the rime condition resulted in streamlined ice shapes. The total ice mass increased as spray duration time increased as can be seen in Column 11 of Table 3 for this sweep. Time lapse video shows continuous shedding of feathers near the ramp top for tests durations longer than 5 min of accretion. Little to no shedding occurred for the first 5 min. The increase in shedding after 5 min may be a result of larger feather accretions experiencing more drag. The larger feather accretions can be seen for the 15 min spray in Panel (B), whereas the feathers are small and more difficult to see in Panel (A). Repeat test points were conducted at 5 min of spray duration time and resulted in just a 1% difference in total ice mass, suggesting very good repeatability. For reference, these two repeated test runs were conducted 10 days apart.

Figure 17 shows cross-sections of the accreted ice at the center-span for the spray duration time sweep under rime ice conditions. The increase in ice accretion size for longer duration spray times is evident in each panel in Figure 17. The tests were run at $AOA = 0°$, so the accretions are largely symmetric on all casing surfaces and struts. Symmetric shadow and concentration regions at the struts near the junction can be seen in Panels (C) and (D) due to boundary layer effects along the casing. Figure 17 also shows that ice accreted on both sides of the main body from the leading edge to the struts. The figure shows good repeatability in reproducing the same ice geometry for the 5-min test runs.

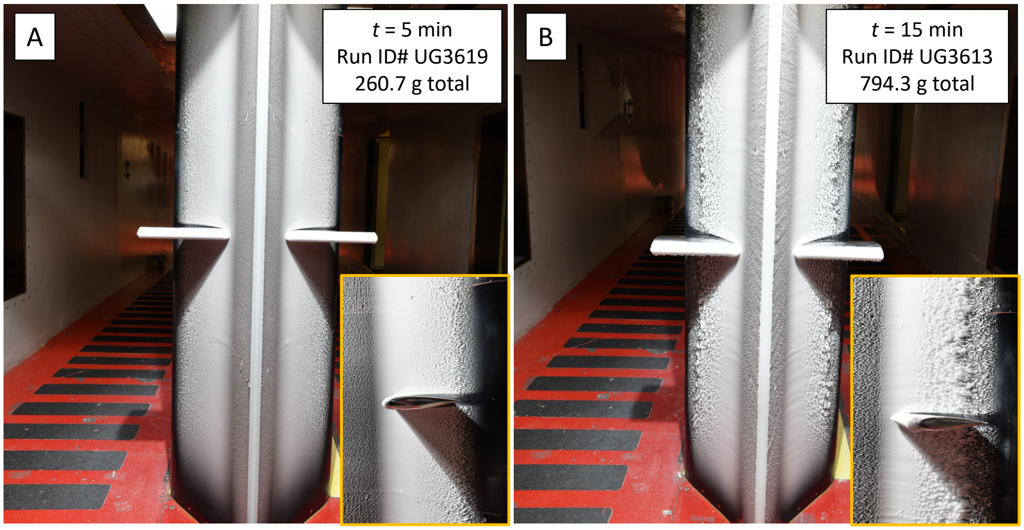

Figure 16.—Images of ice accretions conducted under rime ice conditions after spray durations of (A) *t* = 5 min and (B) *t* = 15 min.

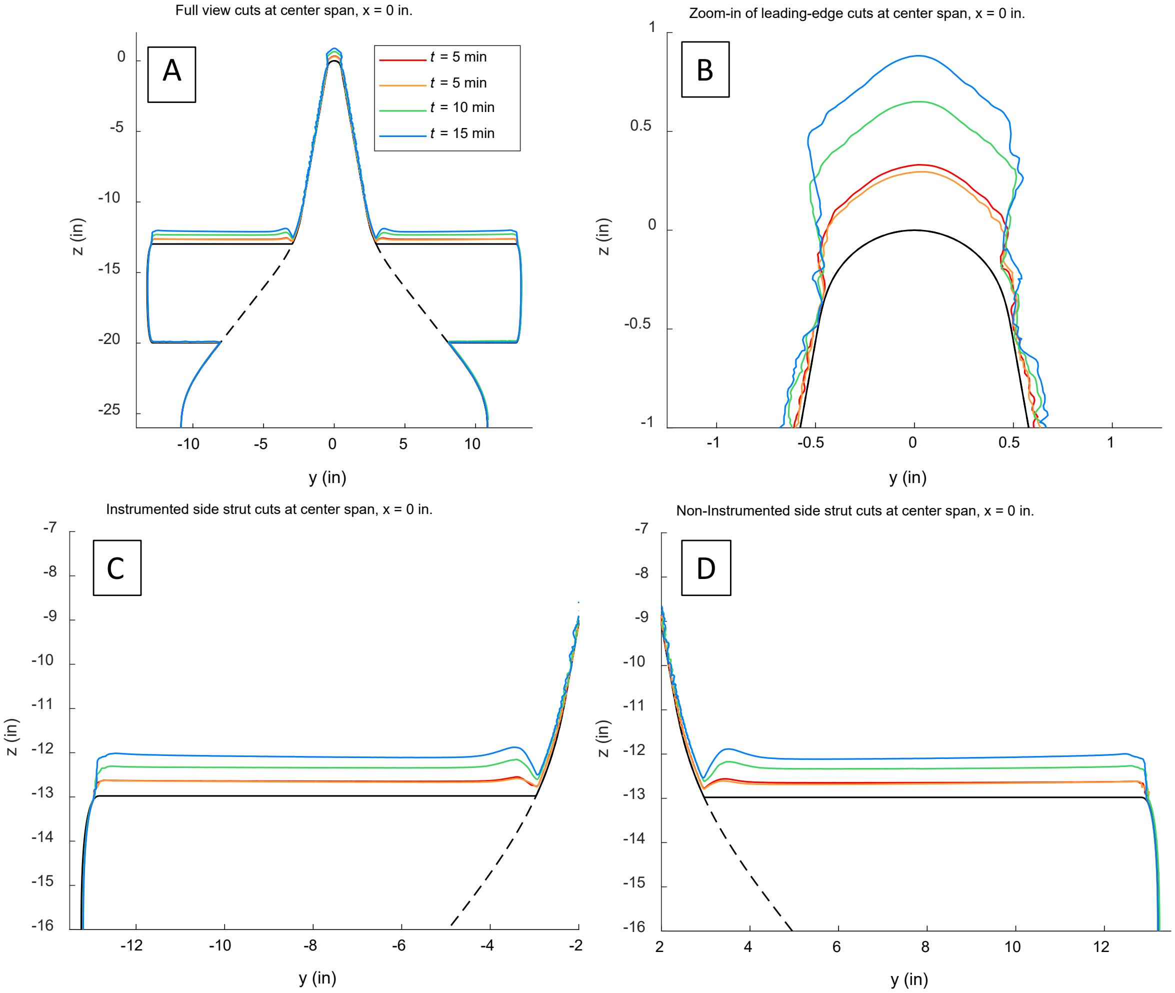

Figure 17.—Cross-sections of the accreted ice at the center-span for the spray time duration sweep under rime ice conditions. Panel (A) shows the overall view, whereas Panels (B), (C), and (D) show zoomed-in cross sections at the leading edge, pressure side strut, and suction side strut, respectively.

Figure 18 shows cross-sections of strut leading edge ice accretions at various locations on both struts for the spray duration time sweep under rime ice conditions. Panels (A) and (B) capture cuts in the concentration regions near the strut junction. Panels (C) and (D) show accretions on the struts that are more in the freestream. Of note is how similar the cross-sections of the main body leading edge ice accretions (Figure 17(B)) are to the outboard strut ice accretions (Figure 18(C) and (D)). This is a reasonable result as the leading edge of the main body and struts are of similar size and both locations experienced freestream cloud flow.

Multiple test points were repeated from the SIDRM 2022 test entry for the spray time duration sweep under rime ice conditions. Table 5 compares accreted ice mass between the 2023 and 2022 SIDRM test entries. Again, the wider struts used during the 2023 tests accreted more ice than the thinner struts used in the 2022 test entry, by nearly twice as much. Ice mass on the casing ranged from 4 to 9% lower for the 2023 tests compared to the 2022 test entry. Again, the lower ice mass measurements in 2023 may be due to more droplets that impinged on the larger struts instead of the casing further aft of the struts.

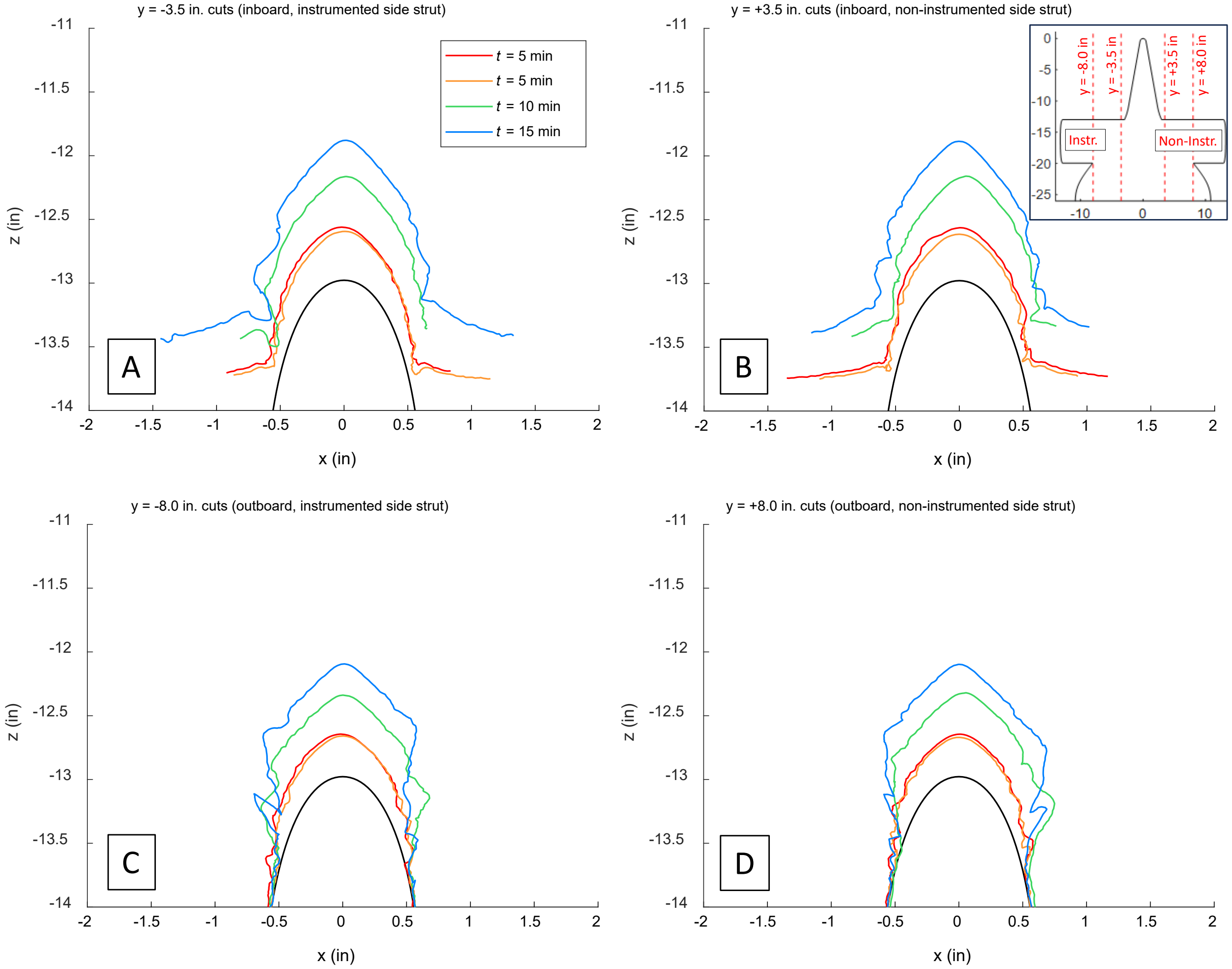

Figure 18.—Cross-sections of strut leading edge ice accretions at inboard (A) and (B) and outboard (C) and (D) locations on both struts for the spray time duration sweep under rime ice conditions.

TABLE 5.—COMPARISON OF ACCRETED ICE MASS ON THE STRUTS AND CASING BETWEEN THE 2023 AND 2022 SIDRM TEST ENTRIES FOR THE SPRAY TIME DURATION SWEEP UNDER RIME ICE CONDITIONS

Spray duration, min	2023		2022	
	Ice mass both struts, g	Ice mass casing, g	Ice mass both struts, g	Ice mass casing, g
5	74.5	189	33	208
5	71.7	189	33	208
10	161.9	392	79	407
15	249.3	545	---	----

5.5 Spray Duration Time Sweep—Glaze Ice Conditions

A spray duration time sweep was conducted under glaze ice conditions (T_0 = –6 °C) where spray time ranged from 5 to 20 min. Figure 19 shows sample images of ice accretion for a spray duration of 5 min shown in Panel (A) and 20 min in Panel (B). The accreted ice is largely opaque for both glaze tests shown in the figure. The insets show the ice accretion on the instrumented side strut, where the glaze condition resulted in a transitory mix between horn and streamlined ice shapes. As expected, the total ice mass increased as spray duration time increased, as can be seen in Column 11 of Table 3 for this sweep. Time lapse video shows continuous shedding of feathers near the ramp top after about 2 min of accretion. Shedding for this sweep occurred noticeably sooner in comparison to the 5 min when shedding was observed to begin for the rime ice test runs described in the previous subsection (Section 5.4). This earlier occurrence of shedding may be a result of weaker ice cohesion strength compared to colder accretions. Repeat test points were conducted at 20 min of spray duration time and resulted in about 4% difference in total ice mass. The difference between the repeated test runs occurred due to differences in ice mass on the struts. For reference, these two repeated test runs were conducted 17 days apart. Note that these two repeat test runs are the same repeated test runs described in the total air temperature sweep of Section 5.3.

Figure 20 shows cross-sections of the accreted ice at the center-span for the spray duration time sweep under glaze ice conditions. The increase in ice accretion size for longer duration spray times is evident and expected in each panel in Figure 20. The figure shows generally good repeatability in reproducing the same ice geometry for the 20-min test runs. The tests were run at $AOA = 4°$, so the accretions at the leading edge lean towards the pressure side (to the left in Panel (B)). Panels (C) and (D) show evidence of shadow and concentration regions near the strut junction. Looking at the pressure side (Panel (C)), the shadow region is small and is likely a result of the boundary layer created by the main body upstream of the struts. The shadow and concentration regions of the impinging cloud are more prominent on the suction side (Panel (D)) as the main body at an AoA blocks and impacts cloud flow to the strut downstream at $AOA = 4°$. The development of horn ice accretions on the main body leading edge for the longer spray duration test runs appear to have expanded the shadow region on both struts nears the junction. The expanded shadow region for longer test runs on the pressure side (Panel (C)) is small, but more prominent on the suction side (Panel (D)). Of note in Panel (B) is that just aft of the leading edge, there is little to no ice on the casing on the suction side, until just aft of the strut where the casing geometry becomes more exposed to the impinging cloud. Panels (B) and (C) show that there is ice accretion on the pressure side of the casing from the leading edge to the struts (and just a bit beyond not shown in the figure).

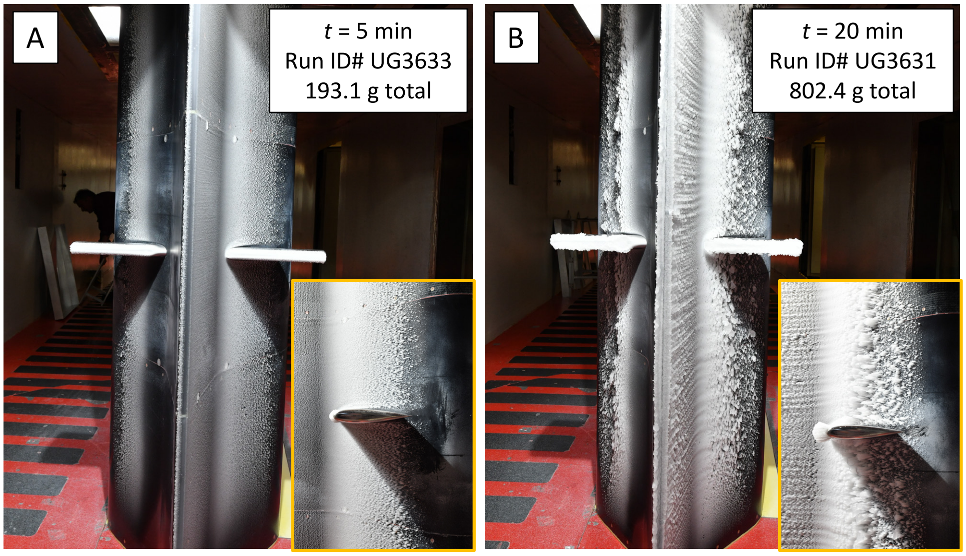

Figure 19.—Images of ice accretions conducted under glaze ice conditions after spray durations of (A) *t* = 5 min and (B) *t* = 15 min.

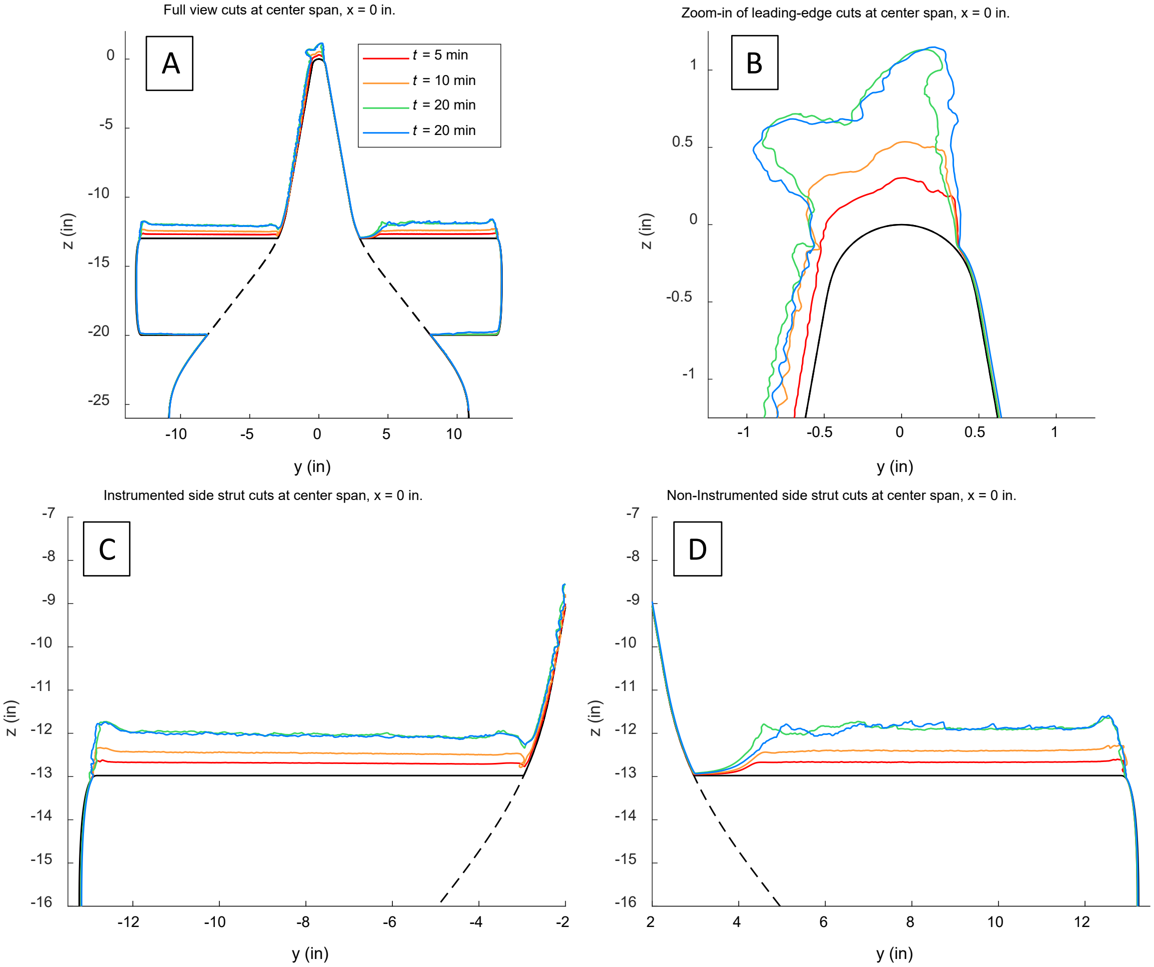

Figure 20.—Cross-sections of the accreted ice at the center-span for the spray duration time sweep under glaze ice conditions. Panel (A) shows the overall view, whereas Panels (B), (C), and (D) show zoomed-in cross sections at the leading edge, pressure side strut, and suction side strut, respectively.

Figure 21 shows cross-sections of strut leading edge ice accretions at various locations on both struts for the spray duration time sweep under glaze ice conditions. Panels (A) and (B) highlight the impact of shadow regions near the strut junction created by the *AOA* = 4° test runs with little to no ice accretion on the suction side (Panel (B)). The cross sections in Panel A (pressure side) show accretions at the strut junction, which captured ice accretion on the strut leading edge and ice that accreted on the main body. Further outward on the struts, Panels (C) and (D) show transitory mix between horn and streamlined ice shapes. The accretions on the suction side in Panel (D) are larger than on the pressure side in Panel (C). In addition, despite the sizeable shadow region created by the main body at *AOA* = 4°, accretion mass was greater for the suction side strut than the pressure side strut for all accretion times conducted in the sweep (see Columns 8 and 9 from Table 3). It is possible that there is a concentration of the cloud on the suction side when the large test article is at a positive AoA because the flow is more constricted on that side. This would require additional independent measurements and CFD studies to verify this hypothesis.

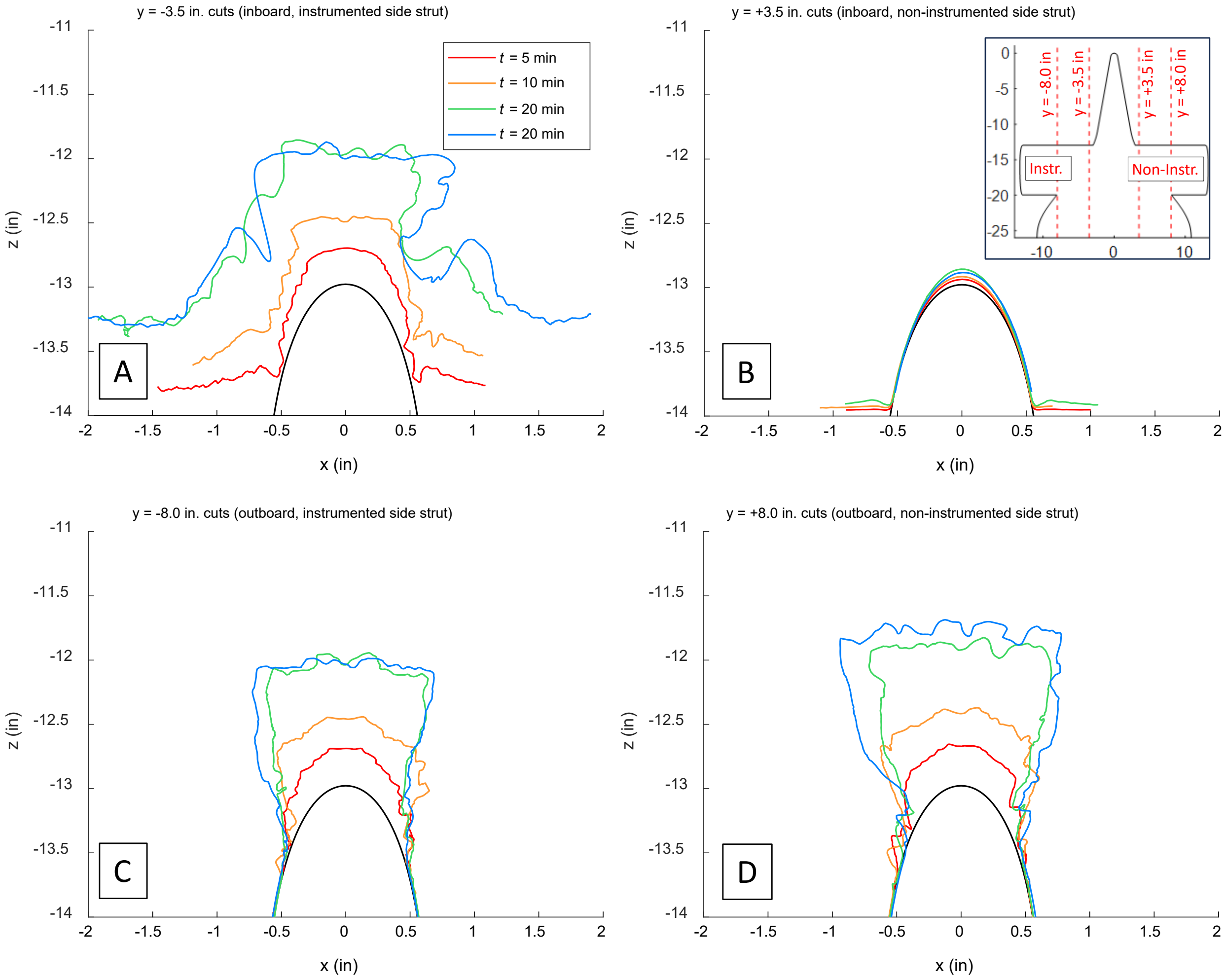

Figure 21.—Cross-sections of strut leading edge ice accretions at inboard (A) and (B) and outboard (C) and (D) locations on both struts for the spray time duration sweep under glaze ice conditions.

5.6 Cloud Median Volumetric Diameter Sweep

A median volumetric diameter (*MVD*) sweep was conducted under rime ice conditions ($T_0 = -17$ °C) where *MVD* ranged from 18 to 90 µm. Figure 22 shows sample images of ice accretions conducted under icing clouds of *MVD* = 18 µm shown in Panel (A) and *MVD* = 90 µm in Panel (B). The insets show the non-instrumented side (suction side) ice accretion and highlights the differences in impingement limits between different *MVD* clouds. This *MVD* sweep was performed at *AOA* = 4°, resulting in a shadowed casing on the suction side, with no ice accreting just aft of the leading edge until the casing ramp area near the strut. Larger *MVD* clouds impinged further upstream into the casing shadow region on the suction side. Larger *MVD* clouds also impinged further downstream on the casing ramp beyond the strut, on both the suction and pressure sides. These extended impingement limits are directly related to larger droplets being more ballistic resulting in higher collision efficiencies on SIDRM surfaces, whereas smaller droplets followed the flow more closely and resulted in lower collision efficiencies. The total ice mass increased as *MVD* increased, as can be seen in Column 11 of Table 3 for this sweep. This increasing ice mass trend with increasing *MVD* applies entirely on the casing, due to the greater ballistic nature and greater collision efficiency of larger droplets on the various casing surfaces. The ice mass was approximately equal between the struts, despite tests performed at *AOA* = 4°. Time lapse video shows less shedding for larger *MVD* clouds. No shedding was observed for tests with *MVD* of 50 µm and greater for these 3.5-min duration accretion tests. Two sets of repeat test points were conducted at *MVD* = 30 and 90 µm, which resulted in about 2% to 4% difference in total ice mass. For reference, these two repeated test runs were conducted 15 and 9 days apart, respectively.

Figure 23 shows cross-sections of the accreted ice at the center-span for the *MVD* sweep. The ice accretion leading edge thickness increased slightly with increasing *MVD* (Panel (B)). This was likely due to larger drops resulting in greater collision efficiencies at this leading edge for the *MVD* values tested. Panel (C) shows that large *MVD* test runs resulted in thicker ice accretions along the pressure side casing. The majority of increase in total ice mass with increasing *MVD* occurred on the casing, with smaller contributions coming from the struts. This is in agreement with what is shown in Panels (C) and (D). The figure shows good repeatability in reproducing the same ice geometry for the two repeat test runs. The tests were run at *AOA* = 4°, so the accretions at the leading edge lean towards the pressure side (to the left in Panel (B)). Panels (C) and (D) show evidence of shadow and concentration regions near the strut junction.

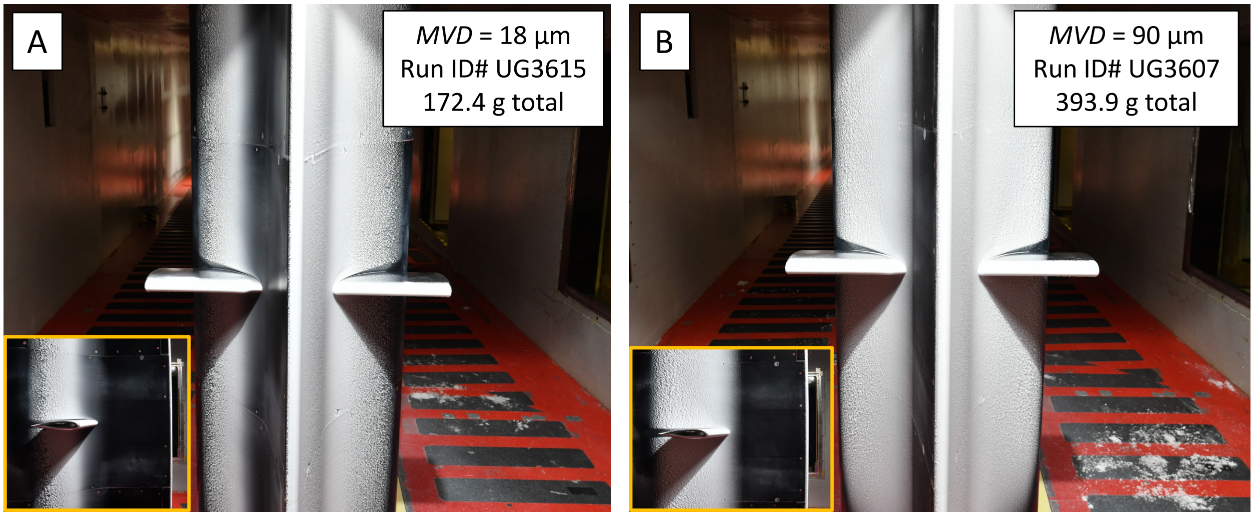

Figure 22.—Images of ice accretions conducted under icing clouds with (A) *MVD* = 18 µm and (B) *MVD* = 90 µm.

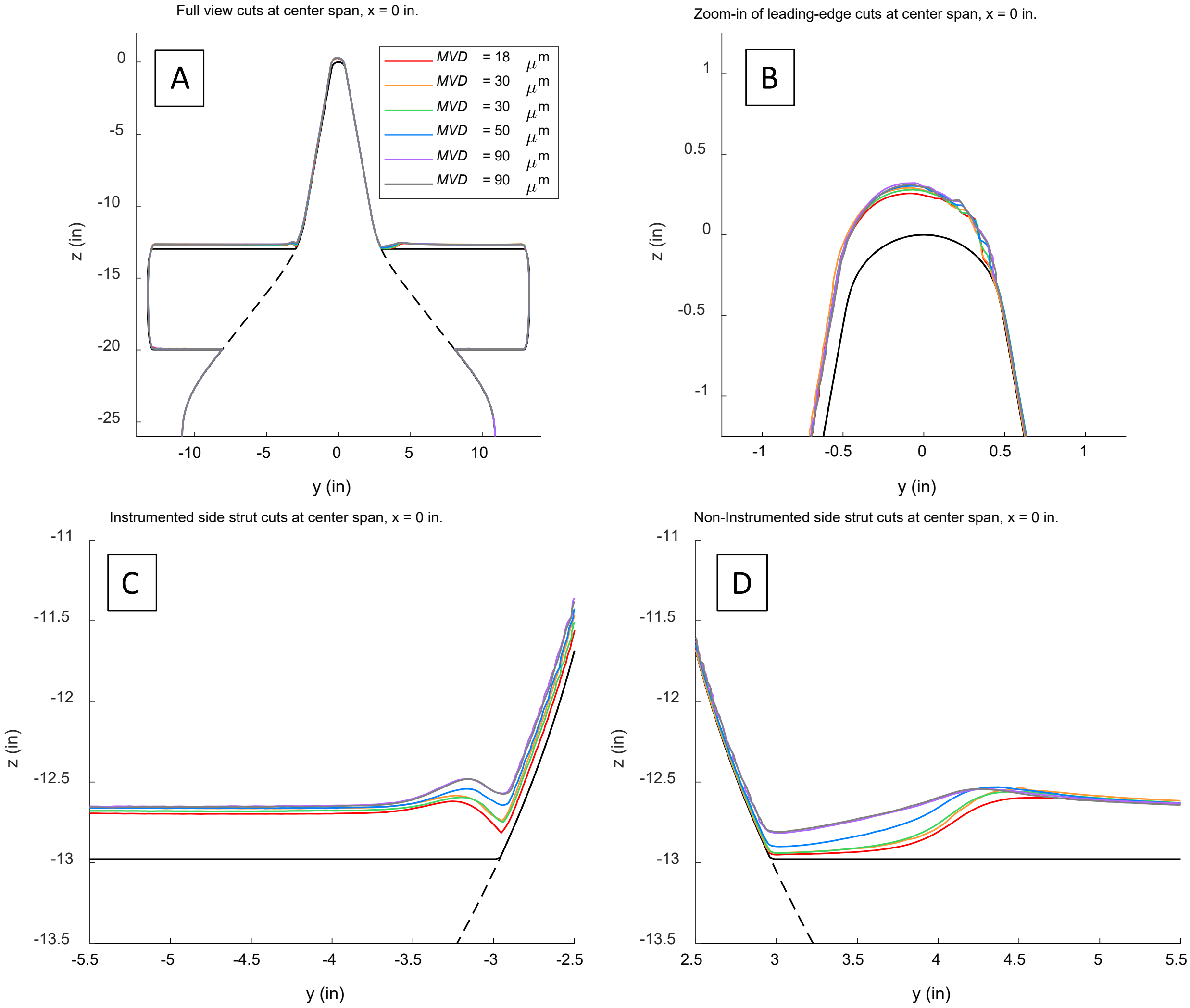

Figure 23.—Cross-sections of the accreted ice at the center-span for the *MVD* sweep. Panel (A) shows the overall view, whereas Panels (B), (C), and (D) show zoomed-in cross sections at the leading edge, pressure side strut, and suction side strut, respectively.

Looking at the pressure side (Panel (C)), the shadow region is small and is likely a result of the boundary layer created by the main body upstream of the struts. The shadow and concentration regions of the impinging cloud are more prominent on the suction side (Panel (D)) as the main body at an AoA blocks and impacts cloud flow to the strut downstream at $AOA = 4°$. Looking at the strut on the suction side (Panel (D)), the severity of shadowing is less prominent for larger *MVD* clouds. Again, this is due to larger droplets being more ballistic than smaller droplets. The cross sections in Panel (B) shows that there is no ice on the suction side casing from just aft of the leading edge to around the strut area (Panel (D)). While it is small, Panel (D) reinforces the statement in the previous paragraph where the impingement limit on the suction side casing is further upstream for larger *MVD* clouds.

Figure 24 shows cross-sections of strut leading edge ice accretions at various locations on both struts for the *MVD* sweep. Panel (A) shows cross sections on the edge of the concentration region at the inboard cut on the pressure side strut, with slightly larger accretions for larger *MVD* clouds. Panel (B) shows cross sections in the shadowed region on the suction side strut, reinforcing the reduced impact of shadowing of larger *MVD* ballistic droplets. Panels (C) and (D) show essentially no variation in strut leading edge ice accretion size and geometry for the various *MVD* test runs. This low sensitivity to *MVD* may be due to similar collision efficiencies on the narrow struts for all *MVD* tested.

5.7 Angle of Attack Sweep

An *AOA* sweep was conducted under rime ice conditions (T_0 = –17°C) where *AOA* ranged from 0 to 4°. Figure 25 shows sample images of ice accretions conducted at *AOA* = 0° shown in Panel (A) and *AOA* = 4° in Panel (B). The insets show the overhead view of the non-instrumented side strut (suction side when *AOA* > 0°). The insets show the ice accretion profile at the strut leading edge. Note that ice only accreted on the strut leading edge, and any white surfaces seen aft of the leading edge is white titanium dioxide paint used for 3D laser scanning that was not fully removed from the strut. The strut ice accretion profiles in the insets highlight the shadow and concentration regions that resulted when the test article was rotated for the 4° *AOA* test run. The test run performed at *AOA* = 4° (Panel (B)), resulted in a shadowed casing on the suction side, with no ice accreting just aft of the leading edge until the casing ramp area near the strut. Whereas ice accreted on all forward surfaces of the main body for the test run performed at *AOA* = 0° (Panel (A)). As a result, ice mass largely decreased with increasing *AOA*, as can be seen in Column 11

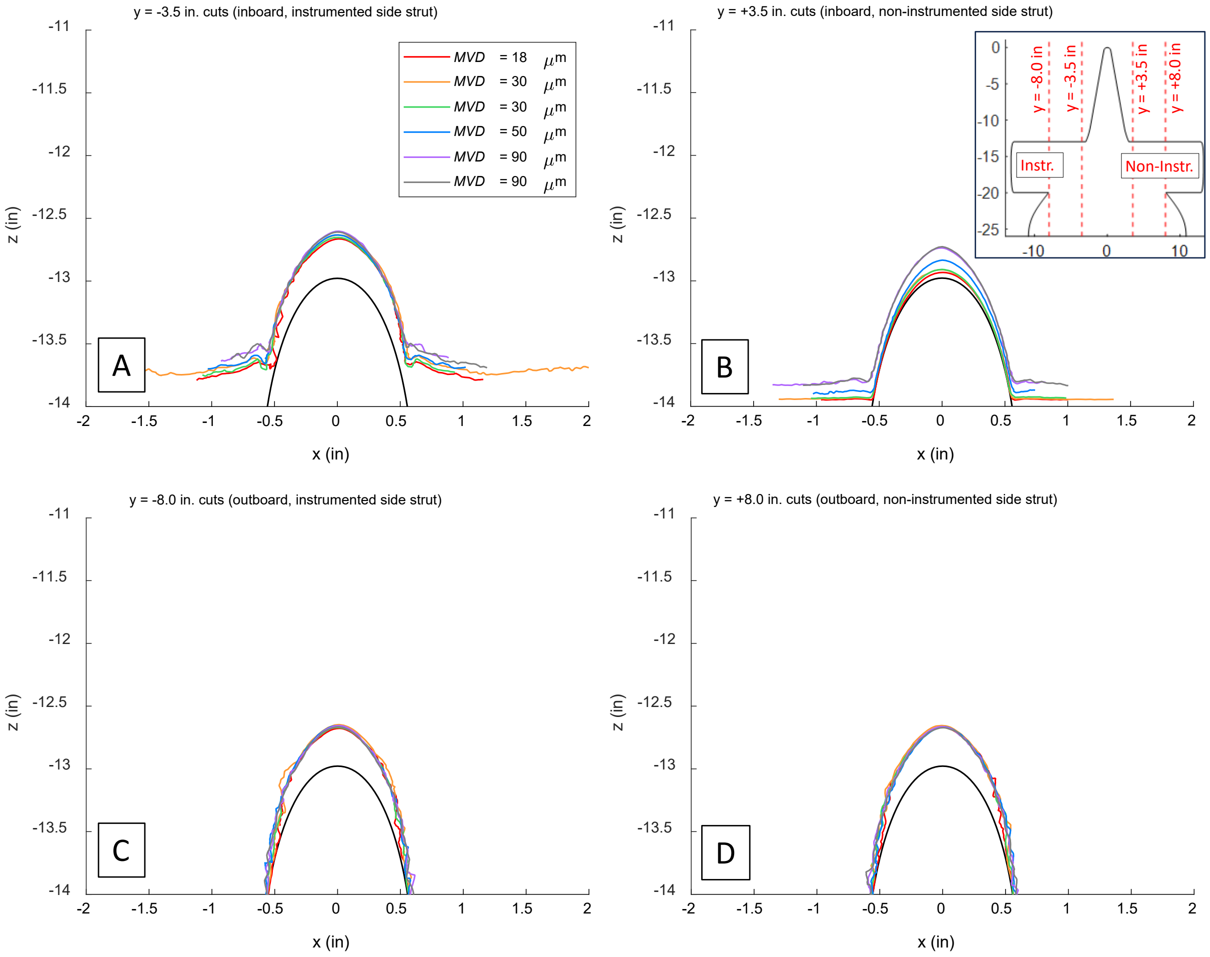

Figure 24.—Cross-sections of strut leading edge ice accretions at inboard (A) and (B) and outboard (C) and (D) locations on both struts for the *MVD* sweep.

of Table 3 for this sweep. This trend is due to more main body surfaces that experienced increased shadowing from the cloud at greater angles of attack. A test run was performed at *AOA* = 0.35°, the angle that was preliminarily determined after aerodynamic testing to be where the stagnation line occurred at the leading edge (this was determined to be *AOA* = 0.30° after post-processing as noted in Section 4.5). There was 3% more ice mass measured for this *AOA* = 0.35° compared to the *AOA* = 0.0° test run. For reference, the repeat test runs in this sweep varied by 2%. This suggests that differences between the *AOA* = 0.0 and 0.35° test runs are similar to the testing variation noise and the impact is small. The ice mass was approximately equal between the struts for all angles of attack tested for this sweep (see Table 3, Columns 8 and 9). Time lapse video showed very little shedding for these 3.5-min duration accretion tests.

Figure 26 shows cross-sections of the accreted ice at the center-span for the *AOA* sweep. Panel (B) shows how the accreted ice at the main body leading edge shifts to the pressure side as *AOA* increased. Panels (B), (C), and (D) show how the casing ice is symmetric for the *AOA* = 0.0 and 0.35° test runs, but as *AOA* increased, more ice accreted on the pressure side casing (Panel (C)), and shadowing effects became more significant on the suction side casing (Panel (D)). Panels (C) and (D) show evidence of shadow and concentration regions on the strut near the junction. Looking at the pressure side (Panel (C)), the shadow region is small due to the boundary layer created by the main body upstream of the struts and became smaller as *AOA* increased. The shadow and concentration regions of the impinging cloud are more prominent on the suction side (Panel (D)) as the main body blocked more of the impinging cloud as *AOA* increased. Of note, the cross section accretions are very similar for the *AOA* = 0.0 and 0.35° test runs in all panels of Figure 26, highlighting the small impact the deviation of the true aerodynamic stagnation line at the leading edge has on the overall ice accretion.

Figure 27 shows cross-sections of strut leading edge ice accretions at various locations on both struts for the *AOA* sweep. Panels (A) and (B) show variation in cross section geometry as these inboard cuts are taken in the shadow and concentration regions on the struts. Panels (C) and (D) show essentially no variation in strut leading edge ice accretion size and geometry for the various *AOA* test runs, and little to none was expected as changing *AOA* does little to impact collision efficiency in the outboard sections of the struts that are exposed to the free stream.

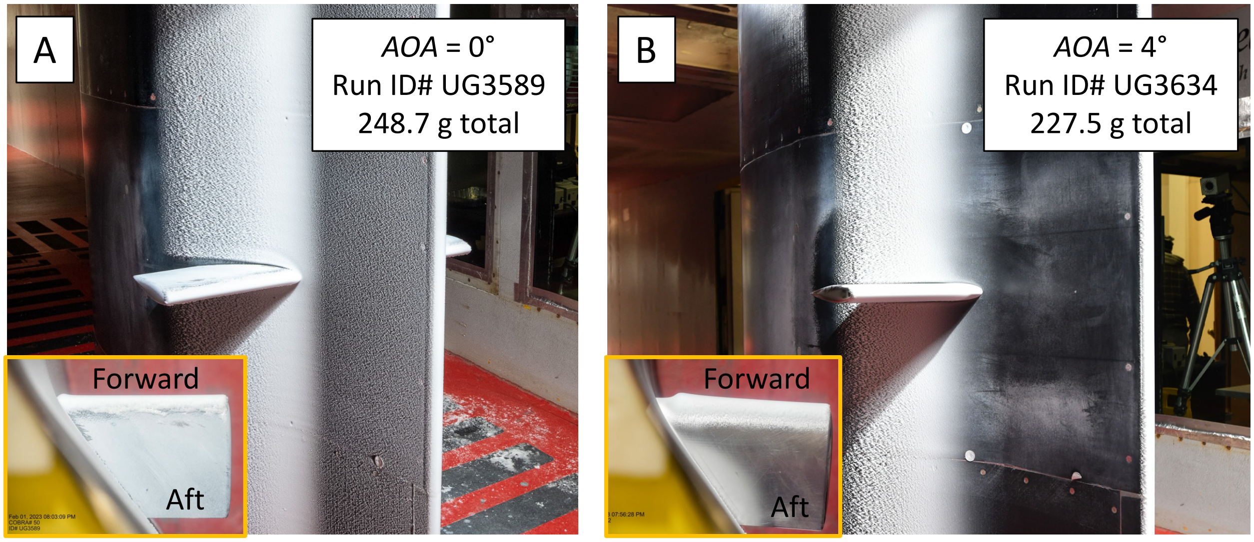

Figure 25.—Images of ice accretions conducted at (A) *AOA* = 0° and (B) *AOA* = 4° showing impacts of shadowing effects.

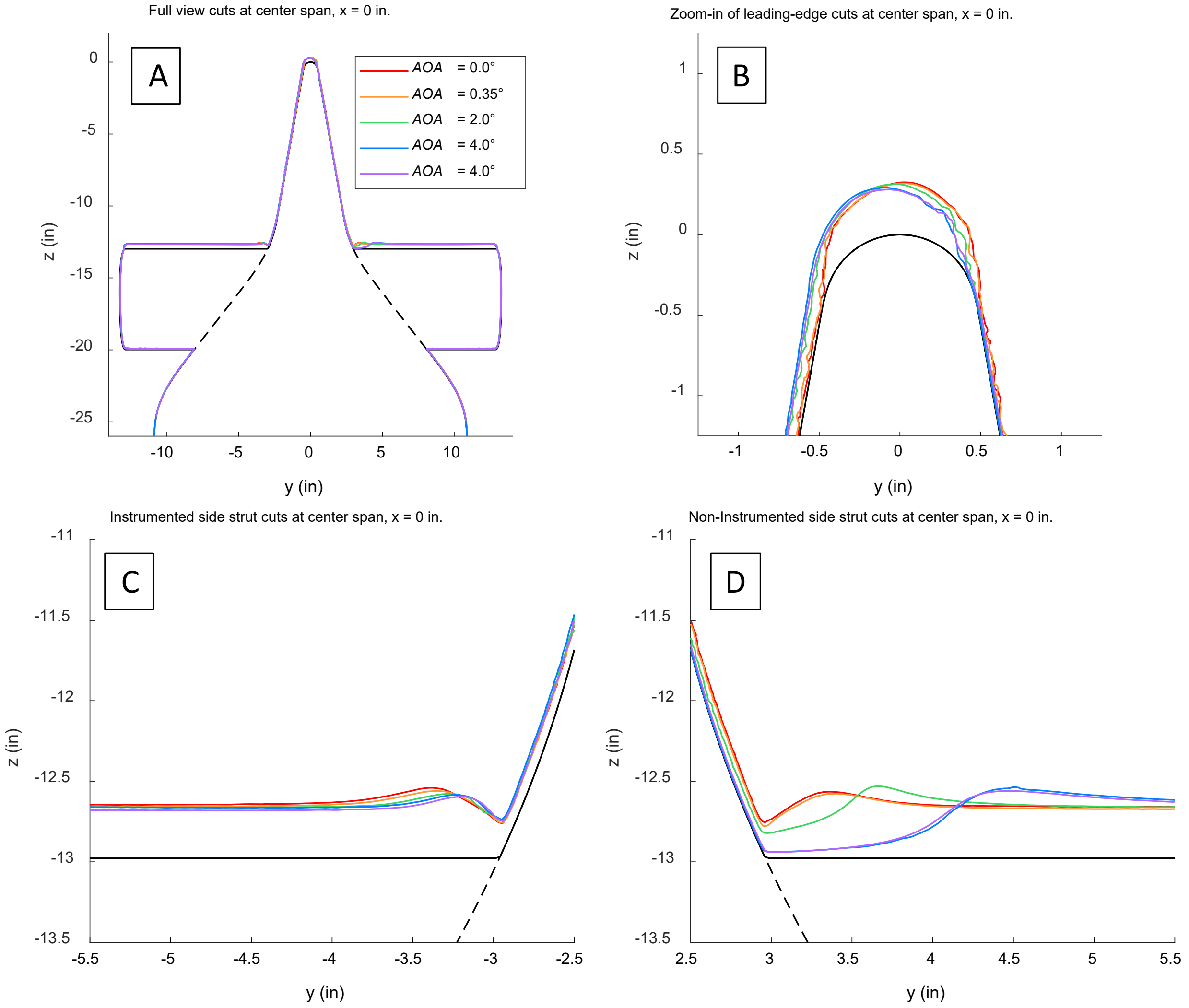

Figure 26.—Cross-sections of the accreted ice at the center-span for the *AOA* sweep. Panel (A) shows the overall view, whereas Panels (B), (C), and (D) show zoomed-in cross sections at the leading edge, pressure side strut, and suction side strut, respectively.

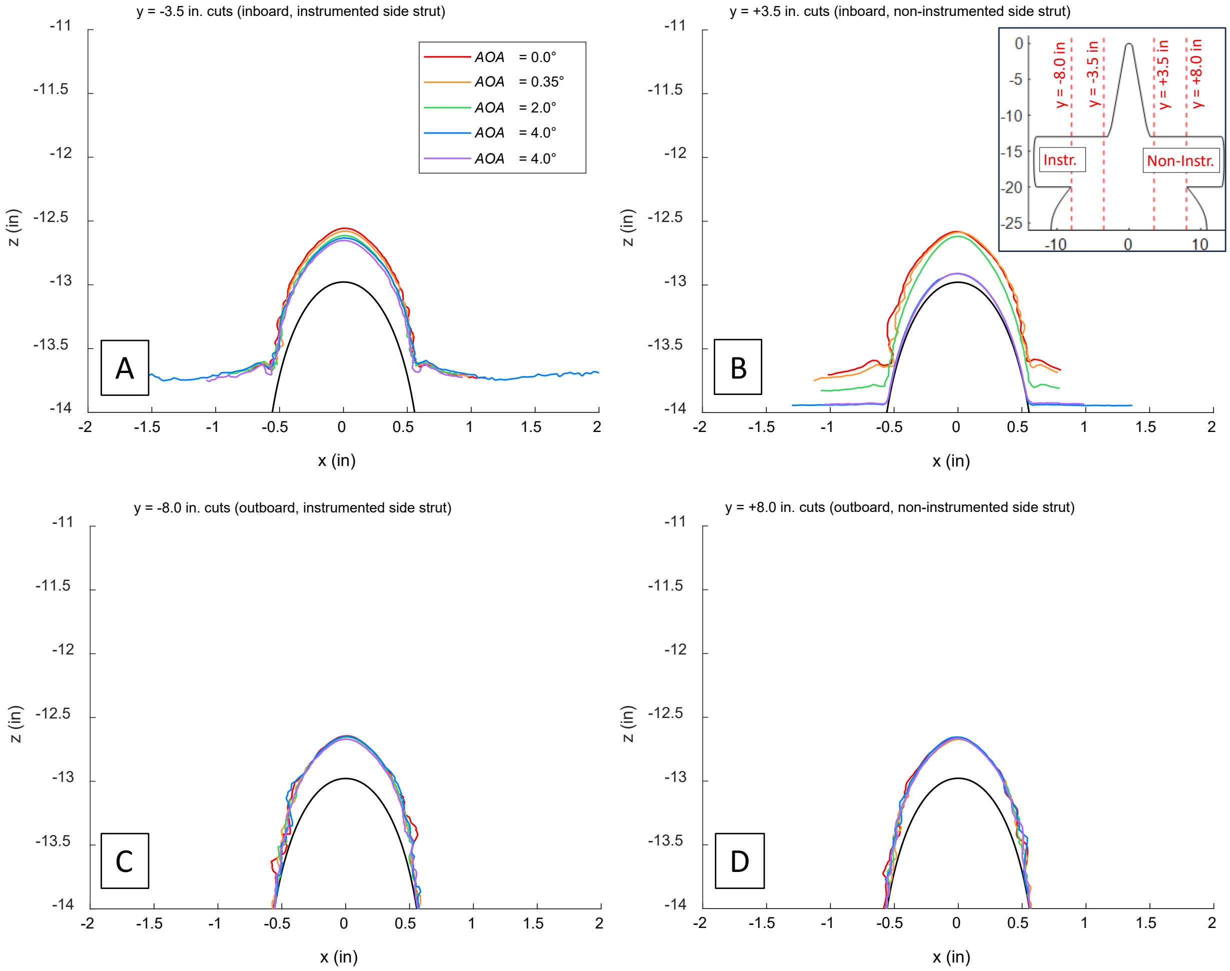

Figure 27.—Cross-sections of strut leading edge ice accretions at inboard ((A) and (B)) and outboard ((C) and (D)) locations on both struts for the *AOA* sweep.

6.0 Ice Crystal Icing Tests

6.1 Ice Crystal Icing Test Objectives and Test Matrix

Multiple objectives where set for these ice crystal icing (ICI) tests and are listed below.

- Evaluate impact of larger and shifted forward struts on ice accretion around the strut junction.
- Conduct ICI tests that repeat test conditions that were performed during the SIDRM 2022 test entry. Whereas differences exist in *U* and *IWC* due to the reference pressure issues discussed in Section 3.0, comparisons can provide insight on repeatability and impact of the new struts.
- Conduct tests evaluating impact of heater surface heat flux on ice accretion.
- Conduct parameter sweeps where all other test conditions, including heater settings, are fixed to measure that parameter's impact on ice accretion size/mass, location, and characteristics (such as shedding and ice growth features). The initial 2022 test entry was more exploratory in nature and heater settings were varied within those parameter sweeps.
- Conduct repeat test runs to quantify repeatability.

Twenty-one ice crystal icing tests are presented here from the 2023 test entry. Table 6 shows the test conditions in Columns 1 to 7, heat flux settings for the six SIDRM heater sections in Columns 8 to 13, and resulting accretion mass in Columns 14 to 17. Table 6 is ordered in blocks according to different test objectives. Shaded orange cells indicate condition or heater setting that varied for that test objective block. Three test points were repeated to provide a measure of repeatability (e.g., UG3594 and UG3626 in the second test objective block). The airspeed is corrected for the reference pressure issue. No correction is provided for the ice water content (*IWC*). The *IWC* values listed in Table 6 are from ice crystal cloud characterization tests conducted during the 2022 test entry (Ref. 35). The *IWC* that was measured in 2022 was a combination of the glaciated icing cloud that was directly injected into the test section from the spray bars (freezeout of sprayed liquid droplets) and recirculation of the glaciated icing cloud within the closed-loop wind tunnel. Looking at the direct spray bar contribution to *IWC*, the correction is within 1% from the intended water content for the conditions sprayed. The recirculating component is estimated to be impacted by this amount as well. This total correction amount falls within the variation noise measured for *IWC* during the 2022 characterization tests, which was around 10%. For this reason, no *IWC* corrections were made. The *MVD* values listed in Table 6 are also from ice crystal cloud characterization tests conducted during the 2022 test entry. Particle size distributions for the ice crystal clouds used for ice accretion tests are provided in Table A.8 in the Appendix. Again, the static relative humidity is approximated to be saturated at the test section for this atmospheric wind tunnel as an equilibration spray was performed at the start of each day of testing, which introduced humidity to the flowing air.

Power supply controllers provided power to the six heating zones, where each of the six zones was controlled independently. For Zone 1 that was heated by a cartridge heater, the heat flux values were calculated using the power as measured by the power supply controller divided by the full surface area of a cylinder with a 0.47-in. radius, an approximation for the outer mold line geometry of the leading edge. For Zones 2 to 6, heat flux values were calculated using the power as measured by the power supply controller to each zone and divided by the thin film resistive heating element footprint. All heat generated by the heaters was approximated to be transferred outward toward the outer mold line of the test article, as the side of the heater facing away from the outer mold line was lined with several layers of insulation.

TABLE 6.—TEST CONDITIONS AND HEATER SETTINGS FOR THE ICE CRYSTAL ICING TESTS, GROUPED BY TEST OBJECTIVE WITH ACCRETED ICE MASS THAT WAS MEASURED

[Shaded orange cells indicate condition or heater setting that varied for that test objective block.]

Test run conditions							Heater settings						Accreted ice mass measurements			
Column 1	Column 2	Column 3	Column 4	Column 5	Column 6	Column 7	Column 8	Column 9	Column 10	Column 11	Column 12	Column 13	Column 14	Column 15	Column 16	Column 17
Test run, no.	Spray duration, min	T_0, °C	U, knots	AOA, °	MVD, µm	IWC, g/m^3	Zone 1 flux, W/in^2	Zone 2 flux, W/in^2	Zone 3 flux, W/in^2	Zone 4 flux, W/in^2	Zone 5 flux, W/in^2	Zone 6 flux, W/in^2	Instrument casing, g	Non-instrument casing, g	Leading edge, g	Ice mass total, g
Block 1: Repeat of 2022 Test Conditions at T_0 = –15 °C																
UG3596	10.0	–15	152.5	0	27	1.9	7.1	2.8	3.3	3.2	6.3	4.0	17	18	---	35
UG3592	10.0	–15	152.5	2	27	1.9	7.1	2.8	2.7	3.2	6.3	4.0	26	7	---	33
UG3581	10.0	–15	152.5	4	27	1.9	7.1	2.3	2.5	3.2	6.3	4.0	18	--------------	17	35
Block 2: Repeat of 2022 test conditions at T_0 = –20 °C																
UG3599	10.0	–20	152.5	0	26	2.2	8.9	3.6	4.2	4.0	7.9	4.6	22	16	---	38
UG3595	10.0	–20	152.5	2	26	2.2	8.9	3.6	3.3	4.0	7.9	4.6	26	Not weighed	---	26
UG3594	10.0	–20	152.5	4	26	2.2	8.9	3.1	3.3	4.0	7.9	4.6	17	--------------	17	34
UG3626	10.0	–20	152.5	4	26	2.2	8.9	3.1	3.3	4.0	7.9	4.6	12.5	--------------	10.4	22.9
Block 3: Heater surface heat flux evaluation																
UG3629	10.0	–20	152.5	4	26	2.2	7.1	3.1	3.3	4.4	7.5	5.3	17.1	--------------	10.1	27.2
UG3627	10.0	–20	152.5	4	26	2.2	9.9	3.1	3.3	4.4	7.5	5.3	28.2	--------------	27.6	55.8
UG3637	10.0	–20	152.5	4	26	2.2	12.0	3.1	3.3	4.4	7.5	5.3	46.4	28.2		74.6
UG3630	10.0	–20	152.5	4	26	2.2	12.0	3.6	3.9	4.4	7.5	5.3	28.3	9.7	---	38
Block 4: Spray Duration Time Sweep																
UG3622	5.0	–20	152.5	0	41	3.0	16.7	3.9	4.2	6.1	7.5	5.3	11.8	13	---	24.8
UG3624	10.0	–20	152.5	0	41	3.0	16.7	3.9	4.2	6.1	7.5	5.3	31.6	33.9	---	65.5
Block 5: AOA sweep at T_0 = –15 °C and U = 207 knots																
UG3600	10.0	–15	207	0	28	2.0	9.9	3.1	3.3	4.4	7.5	5.3	----	3.5	---	3.5
UG3601	10.0	–15	207	2	28	2.0	9.9	3.1	3.3	4.4	7.5	5.3	4.2	--------------	---	4.2
UG3597	10.0	–15	207	4	28	2.0	9.9	3.1	3.3	4.4	7.5	5.3	11	--------------	8	19
UG3623	10.0	–15	207	4	28	2.0	9.9	3.1	3.3	4.4	7.5	5.3	13.6	--------------	6.5	20.1
Block 6: AOA sweep at T_0 = –20 °C and U = 152.5 knots																
UG3611	5.0	–20	152.5	0	41	3.0	9.9	3.1	3.3	4.4	7.5	5.3	1.2	1.4	---	2.6
UG3610	5.0	–20	152.5	2	41	3.0	9.9	3.1	3.3	4.4	7.5	5.3	8.1	--------------	2.9	11.0
UG3609	5.0	–20	152.5	4	41	3.0	9.9	3.1	3.3	4.4	7.5	5.3	13.6	--------------	6.6	20.2
UG3636	5.0	–20	152.5	4	41	3.0	9.9	3.1	3.3	4.4	7.5	5.3	11.8	--------------	5.8	17.6

For reference, the steady state surface temperature prior to spray activation is provided in Table A.9 in the appendix. The measurements listed provide additional insight into the resulting temperatures for the given aerothermal test conditions and heater settings per individual test run.

A key requirement for the ice crystal icing tests was to generate accretions without shedding ice or limit the amount of shedding. This was desired so the scanning and weighing of the accreted ice at the end of a test run would represent the entire accretion process. Conditions that produced ice but had one or more significant sheds provided less valuable quantitative data.

6.2 Testing Procedures—Scanning and Weighing of Ice Mass

The testing procedures for the ice crystal accretion tests are outlined below.

1. Run up IRT to target test airspeed and air temperature.
2. Activate SIDRM heaters to target heat flux values and wait until thermocouples read steady values.
3. Start recording data 30 s prior to spray activation.
4. Turn on ice crystal cloud (spray on).
5. Turn off ice crystal cloud per the time specified on the test matrix (SIDRM heaters turned off simultaneously with spray off).
6. Continue holding tunnel airspeed and air temperature constant as data systems continue recording 30 s post spray.
7. Stop data recording systems and shut down drive fan.
8. Enter test section and take photographs of accreted ice.
9. Perform 3D scan of mid 10-in. span of accreted ice.
10. Using heated knife, cut out mid 8-in. span of accreted ice on casing and scrape ice into tray for weighing.
11. Remove all ice from SIDRM and clean test article, preparing for next test point.

The primary measurements to assess ice crystal ice accretion size were 3D laser scans of the final ice accretion and weighing of the accreted ice. As discussed in the supercooled liquid icing sections, the accreted ice geometry was measured after each test run utilizing a 3D laser scanner. The center 10-in. (0.25-m) span was scanned from the leading edge to the extent of ice on either side of the test article. After scanning, the center 8-in. (0.20-m) span of accreted ice on the casing was cut from the leading edge to the extent of icing on both sides, removed, and weighed. Ice generally accreted on the main body casing in three isolated areas, and they were weighed separately. Figure 28 shows the locations where ice was removed and weighed on the instrumented side casing (yellow box in Panel (A)), the leading edge (sum of green boxes in Panels (A) and (B)), and the non-instrumented side casing (red box in Panel (C)). The instrumented side casing ice mass, non-instrumented side casing ice mass, leading edge ice mass, and the combined total ice mass are provided in Columns 14 to 17, respectively, in Table 6.

Ice crystal icing accretions were generally small as can be seen in Figure 28. Due to the shallow ice accretion geometry, this report will show photos of the accreted ice as they are easier to visualize and are more informative than the cross section from the laser scans.

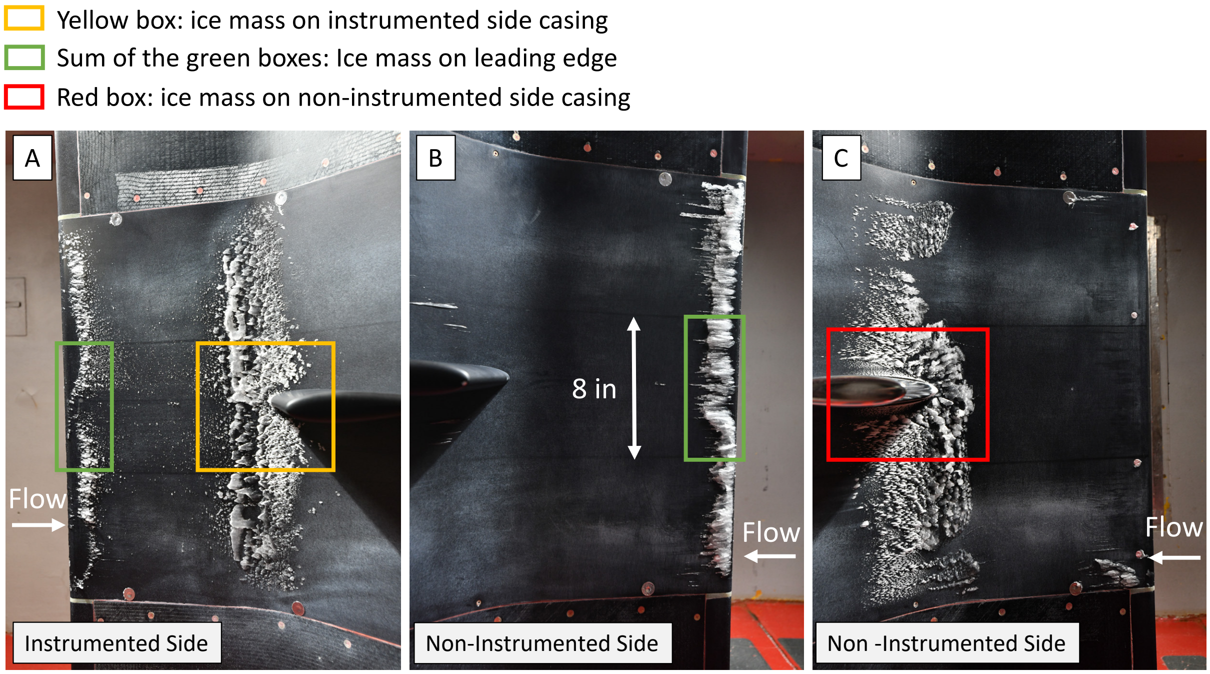

Figure 28.—Images indicating the locations that ice was removed and weighed (A) on the instrumented side casing, (A and B) the leading edge, and (C) the non-instrumented side casing.

6.3 Block 1: Repeat of 2022 Test Conditions at T_0 = –15 °C

Three test points were repeated from the SIDRM 2022 test entry where T_0 = –15 °C (Block 1 of Table 6). There are small differences in heat flux for heating Zones 2 and 3 between the three test points. The AoA varied for where AOA = 0, 2 and 4°. As a reminder, due to the reference pressure issue, airspeed was U = 152.5 knots for 2023 and U = 150 knots for 2022. Whereas this is a small airspeed difference, it was recognized that the steady state SIDRM surface temperatures prior to icing cloud activation were 0.5 to 1.0 °C lower during 2023 testing compared to the 2022 tests, for the same heater setting. The slightly greater airspeed in 2023 may have accounted for this surface temperature difference.

Figure 29 shows ice accretions on the instrumented side, comparing 2023 test runs (Panels (A) to (C)) to 2022 test runs (Panels (D) to (F)). The corresponding repeated test conditions between the 2023 and 2022 tests are indicated with red double-sided arrows. Overall, the location and physical appearance of ice accretions were similar between the repeated test conditions. For, the AOA = 0° test runs (Panels (A) and (D)), the ice only accreted at the ramp base and appeared like frozen runback and amorphous in appearance. Not shown in the figure, ice accreted similarly on the non-instrumented side for these AOA = 0° test runs. For the AOA = 4° test runs (Panels (C) and (F)), ice at first accreted at the ramp base, then around the leading edge later into the test. The accreted ice was more orderly with shark teeth features at AOA = 4°. It is worth noting that shark teeth-like ice accretion features were also observed during the full-scale engine icing tests conducted at GRC (Refs. 29 and 30), suggesting that some basic icing physics were replicated with this component-level test article. More ice is visible for the 2022 test run. No ice accreted on the non-instrumented side (suction side) ramp base for these AOA = 4° test runs.

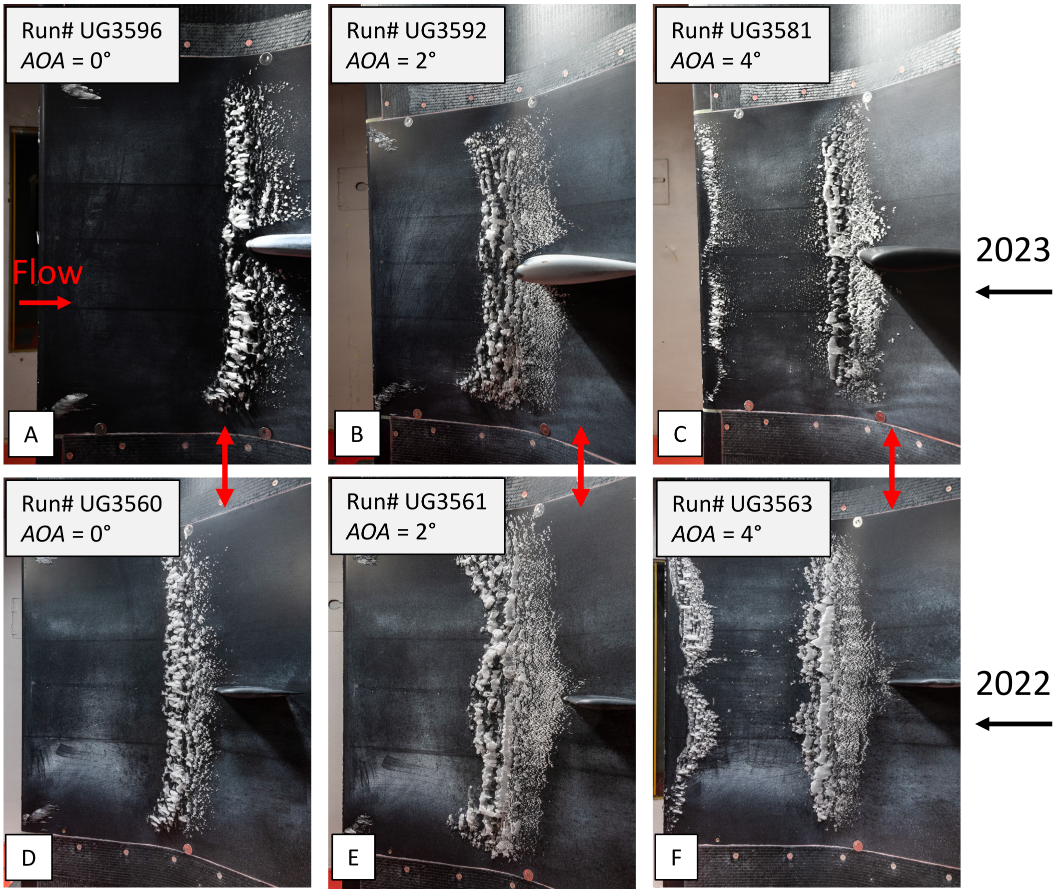

Figure 29.—Images of instrumented side ice accretions comparing 2023 test runs (A) to (C) to 2022 test runs (D) to (F). The corresponding repeated test conditions between the 2023 and 2022 tests are indicated with red double-sided arrows.

The 2022 tests utilized struts that were NACA 0012 in geometry and 4 in. in chord length. Panels (D) to (F) of Figure 29 show how all the ice accreted at the ramp base, just upstream of the strut. These struts did not impact ice crystal ice accretions. The 2023 tests utilized larger struts (NACA 0018 geometry, 7-in. chord) and were also pushed forward 3 in. into the ramp base on the casing. There were expectations that these modified struts would impact ice accretion, with struts acting as a physical anchoring point where more ice would accrete around the strut-casing junction. Panels (A) to (C)of Figure 29 show that this was not the case for this test block. The strut generally displaced ice that had accreted in that location in the 2022 tests. Panels (A) and (B) of Figure 29 show a boundary region around the strut where ice did not accrete. It is not clear if this was due to aerodynamic impacts of the larger strut deflecting impinging ice crystals from the area on the casing around the strut junction, or if it was a thermal impact of the solid unheated strut that cooled the casing around the strut junction to temperatures not suitable for accreting ice.

Table 7 compares accreted ice mass between the 2023 and 2022 SIDRM test entries. The ice mass on the instrumented side casing, non-instrumented side casing, and leading edge for the 2023 and 2022 SIDRM test entries are provided in Columns 2 to 4 and 6 to 8, respectively. Dashes indicates that ice did not accrete in that region. Table 7 shows that less ice accreted on the casing for the 2023 test runs. In part, the 2023 lower ice mass values on the casing may be due to the larger strut displacing ice that had accreted in that location in the 2022 tests. In addition, the slightly higher airspeed tested in 2023 reduced surface temperatures a small amount, where small changes in the overall thermal balance at the surface can critically impact overall ice accretion.

TABLE 7.—COMPARISON OF ACCRETED ICE MASS ON THE INSTRUMENTED SIDE CASING, NON-INSTRUMENTED SIDE CASING, AND LEADING EDGE BETWEEN THE 2023 AND 2022 SIDRM TEST ENTRIES FOR TEST CONDITIONS WHERE $T_0 = -15$ °C

	2023				2022			
	Column 1	Column 2	Column 3	Column 4	Column 5	Column 6	Column 7	Column 8
AOA, °	Test run, no.	Instrument casing, g	Non-instrument casing, g	Leading edge, g	Test run, no.	Instrument casing, g	Non-instrument casing, g	Leading edge, g
0	UG3596	17	18	--	UG3560	30	33	--
2	UG3592	26	7	--	UG3561	39	11	--
4	UG3581	18	--	17	UG3563	24	--	16

6.4 Block 2: Repeat of 2022 Test Conditions at $T_0 = -20$ °C

Three test points were repeated from the SIDRM 2022 test entry where $T_0 = -20$ °C (Block 2 of Table 6). There are small differences in heat flux for heating Zones 2 and 3 between the test points. The AoA varied where $AOA = 0$, 2 and 4°. The $AOA = 4°$ test condition was repeated in 2023 (i.e., two test runs in 2023, and one test run in 2022 for the $AOA = 4°$ test condition). Like with the previous subsection, due to the reference pressure issue, airspeed was $U = 152.5$ knots for 2023 and $U = 150$ knots for 2022.

Figure 30 shows ice accretions on the instrumented side, comparing 2023 test runs (Panels (A) to (D)) to 2022 test runs (Panels (E) to (G)). The corresponding repeated test conditions between the 2023 and 2022 tests are indicated with red double-sided arrows. The two test runs at $AOA = 4°$ in 2023 are shown in Panels (C) and (D), whereas the corresponding repeated test run in 2022 is shown in Panel (G). Overall, the location and physical appearance of ice accretions are similar between the repeated test conditions. For, the $AOA = 0°$ test runs (Panels (A) and (E)), the ice only accreted at the ramp base and its form was amorphous in appearance. For the $AOA = 4°$ test runs (Panels (C)/(D) and (F)), ice at first accreted at the ramp base, then around the leading edge later into the test. The ice accreted as more orderly with shark teeth features at $AOA = 4°$. Some variation in amounts of accreted ice is noticeable between the three test runs at $AOA = 4°$.

Table 8 compares accreted ice mass between the 2023 and 2022 SIDRM test entries. The ice mass on the instrumented side casing, non-instrumented side casing, and leading edge for the 2023 and 2022 SIDRM test entries are provided in Columns 2 to 4 and 6 to 8, respectively. Table 8 shows that less ice mass was measured on both sides on the casing for the $AOA = 0°$ test run in 2023. Figure 30 suggests that this may be due to the larger strut displacing ice that had accreted in that location in the 2022 tests. Table 8 shows that similar ice mass was measured on the instrumented side casing for the $AOA = 2°$ test runs between the years. Ice had accreted on the non-instrumented side casing (not shown in this report) in the 2023 test run but was not weighed. The two test runs conducted in 2023 at $AOA = 4°$ shows the variability that can occur between repeat test runs just 14 days apart. The ice mass measured during the 2022 test series falls between the values measured during the two 2023 tests.

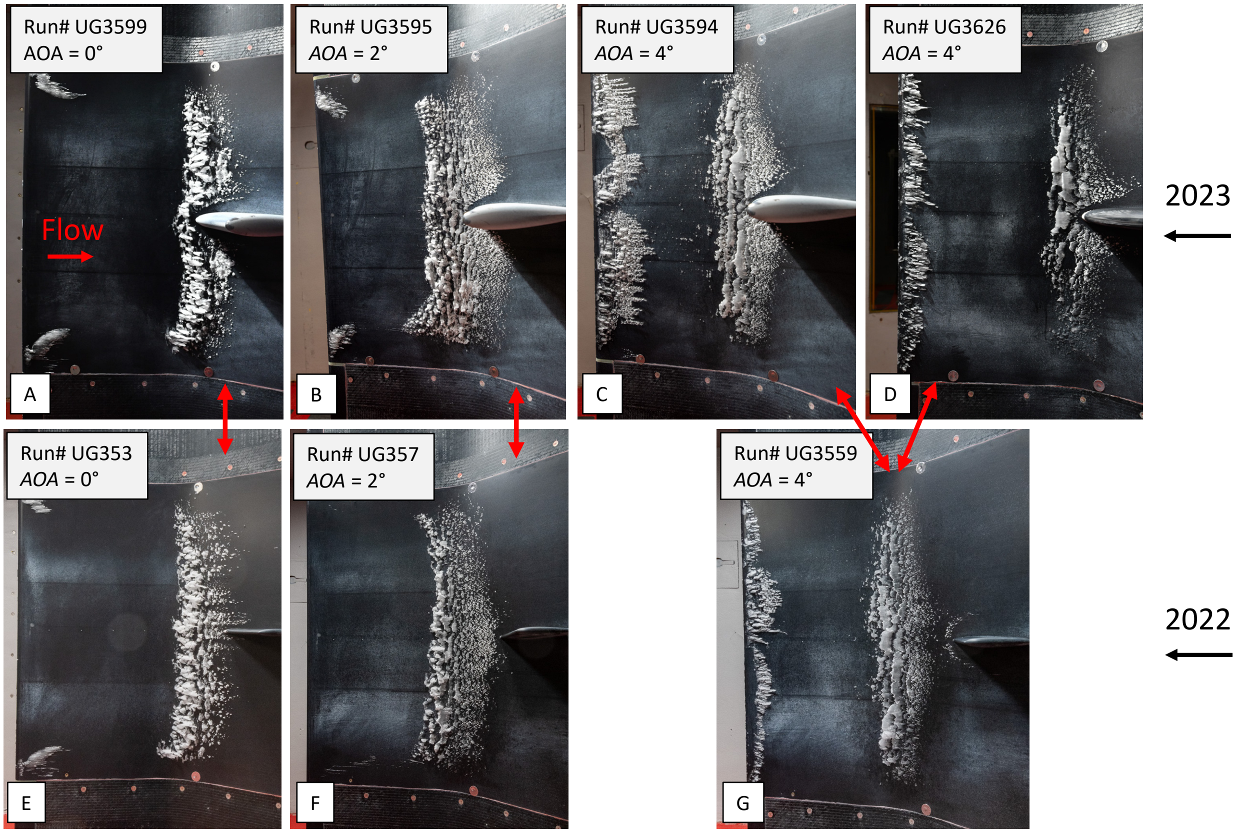

Figure 30.—Images of ice accretions comparing 2023 test runs ((A) to (D)) to 2022 test runs ((E) to (G)). The corresponding repeated test conditions between the 2023 and 2022 test are indicated with red double-sided arrows.

TABLE 8.—COMPARISON OF ACCRETED ICE MASS ON THE INSTRUMENTED SIDE CASING, NON-INSTRUMENTED SIDE CASING, AND LEADING EDGE BETWEEN THE 2023 AND 2022 SIDRM TEST ENTRIES FOR TEST CONDITIONS WHERE $T_0 = -20$ °C

	2023				2022			
	Column 1	Column 2	Column 3	Column 4	Column 5	Column 6	Column 7	Column 8
AOA, °	Test run, no.	Instrument casing, g	Non-instrument casing, g	Leading edge, g	Test run, no.	Instrument casing, g	Non-instrument casing, g	Leading edge, g
0	UG3599	22	16	-----	UG3553	32	33	---
2	UG3595	26	Not weighed	-----	UG3557	23	10	---
4	UG3594	17	----------------	17	UG3559	18	---	14
4	UG3626	12.5	----------------	10.4				

6.5 Block 3: Heater Surface Heat Flux Evaluation

A series of test runs were conducted to evaluate the impact of heat flux on ice accretion (Block 3 of Table 6). Figure 31 illustrates the impact of heat flux on accreted ice mass and location. Heat flux for Zones 1 to 3 varied, with all other test conditions held constant. The shorthand “low”, “medium”, “optimized”, and “high” are used to describe the heater settings used for Zones 1 to 3, and are shown in Panels (A) to (D), respectively. Panel A shows ice accretion that resulted from a test run conducted at the low heat flux

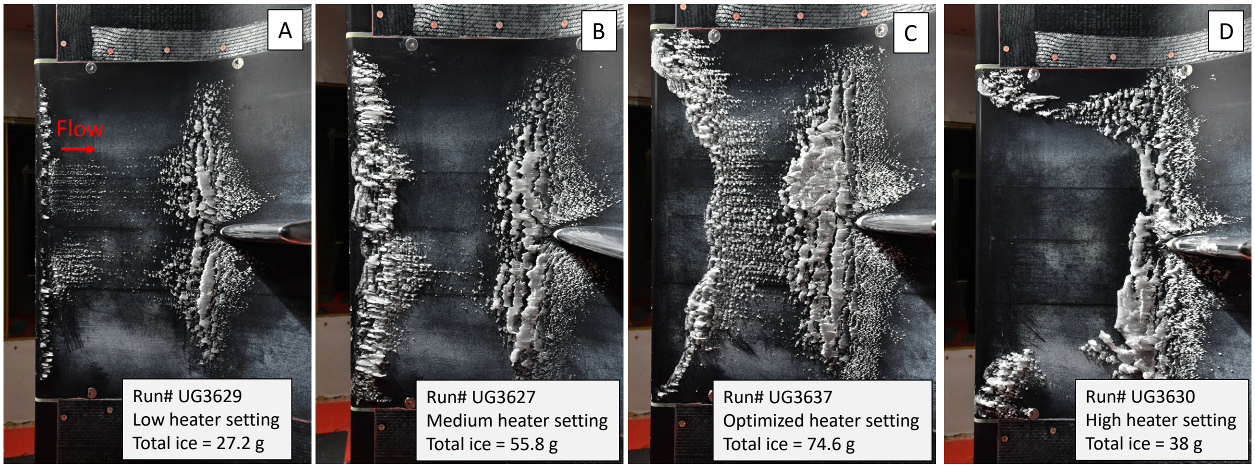

Figure 31.—End of test run images showing the resulting ice accretion at (A) low, (B), medium, (C), optimizes, and (D) high heater settings in terms of accreting ice.

setting, which resulted in the lowest total accreted ice mass. The leading edge became iced about 8 min into the test run limiting the supply of runback melt to the ramp base where impinging ice crystals are better captured by the liquid melt. The leading edge (Zone 1) heat flux was increased for the test run shown in Panel (B), which shows a greater amount of ice that accreted. The warmer leading edge generated more runback melt that captured more of the impinging ice crystals at the ramp base. The leading edge became fully iced near the end of the 10 min test run. The leading edge heat flux was increased even higher for the test run shown in Panel (C). This heater setting resulted in the greatest total accretion ice mass, and for this reason this heater setting is considered optimized for this test block. The higher heat flux for Zone 1 kept the region near the leading edge sufficiently warm that it did not freeze, which provided a continues supply of liquid melt to the ramp base throughout the duration of the test runs. The continuous supply of liquid melt at the ramp base aided in the capture/sticking of impinging ice particles at this higher collision efficiency area of the ramp, resulting in the greatest accretion mass. Panel (D) shows ice accretions resulting from a test run conducted at high heater settings, which resulted in repeated build and shed events throughout the test run. The total accreted ice mass weighed after the test run was lower than others in this test block, however with the continuous build and sheds that occurred throughout the test run, it may have accreted more ice overall but the ice that had shed could not be measured. These test runs demonstrate how upstream heat sources that supply liquid melt to critical regions downstream can lead to larger ice accretions. For reference, Table A.9 in the Appendix lists steady state surface temperatures prior to spray activation and shows how temperatures climbed higher for higher heater settings for this sweep. The ice accretion was orderly with shark teeth features for the first three test runs (Panels (A) to (C)), but was a mixture of order and amorphous disorder for the high heater setting (Panel (D)) from the significant amount of runback melt that was generated and frozen.

6.6 Block 4: Spray Duration Time Sweep

Two test runs were conducted to evaluate the impact of spray duration time (Block 4 of Table 6). Figure 32 shows the resulting ice accretions conducted for 5 min of spray duration time in Panel (A) and 10 min of spray duration time in Panel (B). These were two separate tests that started with a clean test article (i.e., not a continuation of the 5-min spray). The inset in Panel (B) shows the ice accretion midway into the 10-min spray to compare with the 5-min test run. Comparing the two test runs at 5 min, the ice accretion location and size are similar, indicating good repeatability. The 10-min run resulted in a greater accretion size and more than twice the ice mass as ice accreted throughout the test run (see Table 6, Column 17) . It should be noted that the leading edge is clear of ice and was able to provide a continuous supply of liquid melt to the ramp base around the strut. For reference, of all test runs presented in this report, these tests used the highest heat flux setting for Zones 1 to 4 (the forward half of the SIDRM test article where all icing occurred). These test runs demonstrate how engines exposed to ice crystal clouds for longer durations can result in greater amounts of ice accretions if engine surfaces are sufficiently warm and provide a continuous heat supply.

These tests showed that the strut had some impact on the ice accretion. Ice began accreting around the strut at the start of the test run and slowly grew further out in the span and axial directions. The regions lateral to the strut were largely clear of ice after 5 min, suggesting that without the strut presence, ice would not have accreted. There are three factors that may have contributed to the ice accretion near the strut. The first is the strut's physical presence which could have acted as a backstop for some of the runback melt and impinging ice crystal cloud. Secondly, the solid unheated strut may have aided cooling locally on the main body by acting like a fin heatsink. The runback melt with impinging ice crystal cloud may have been cooled down enough to freezing temperatures and began accreting around the strut. Finally, there is a hole in the thin film heater under the struts as there is structural support on the underside of the main body under the strut. This will naturally result in cooler surface temperatures locally around the strut. Despite this heater "dead zone" under the strut, it did not seem to impact accretion for most of the other tests, as most other tests resulted in more uniform accretions across the span. The ice accretions in both test runs were amorphous in appearance.

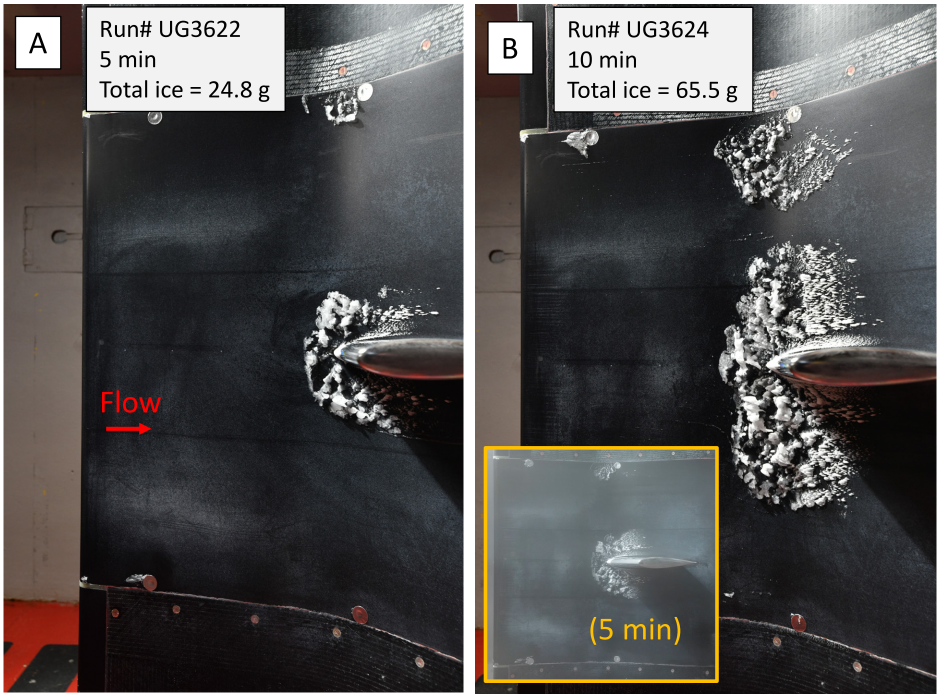

Figure 32.—End of test run images showing the resulting ice accretion for spray duration times of (A) 5 min and (B) 10 min, with inset showing accretion midway into the 10-min spray for comparison.

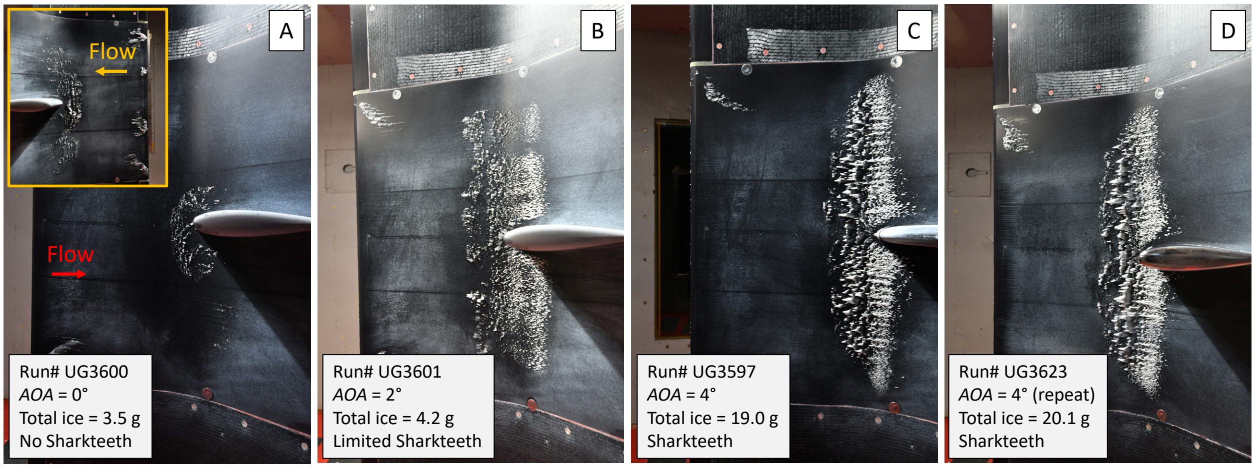

Figure 33.—End of test run images showing the resulting ice accretion from test runs conducted at (A) *AOA* = 0°, (B) *AOA* = 2°, (C) *AOA* = 4°, and (D) a repeat run at *AOA* = 4°. The inset in Panel (A) for the *AOA* = 0° test run shows the non-instrumented side ice accretion for comparison.

6.7 Block 5: Angle of Attack Sweep at T_0 = –15 °C and U = 207 knots

An *AOA* sweep was conducted at T_0 = –15 °C and U = 207 knots to evaluate that parameter's impact on ice accretion (Block 5 of Table 6). All other test conditions, including heater settings, were fixed for this *AOA* sweep. Figure 33 shows the resulting ice accretions conducted at *AOA* = 0° (Panel (A)), *AOA* = 2° (Panel (B)), *AOA* = 4° (Panel (C)), and a repeat run at *AOA* = 4° (Panel (D)). The inset in Panel (A) shows the non-instrumented side for comparison against the instrumented side ice accretion. Slightly more ice accreted on the non-instrumented side for the *AOA* = 0°. Due to the negligible amount of ice on the instrumented side, only the non-instrumented side ice was weighed. Overall, very little ice accreted for the *AOA* = 0° test run. Accreted ice mass increased with increasing *AOA*. A higher collision efficiency at the ramp base is expected at larger *AOA*, which was likely a factor in the greater ice mass that was measured. This has implications for designs that have sharper gooseneck angles in the compressor core that can promote higher collision efficiencies. Figure 33 shows that ice accretions with shark teeth features were more prominent at larger angles of attack. No shark teeth ice features were observed for tests conducted at *AOA* = 0° (Panel (A)), a limited amount of shark teeth features appear at *AOA* = 2° (Panel (B)), and more prominent shark teeth features can be seen at *AOA* = 4° (Panels (C) and (D)). Repeatability was good as similar ice mass, location, and appearance accreted for the two tests conducted at *AOA* = 4°. The strut had little impact on ice accretion throughout the test.

6.8 Block 6: Angle of Attack Sweep at T_0 = –20 °C and U = 152.5 knots

An *AOA* sweep was conducted at T_0 = –20 °C and U = 152.5 knots to evaluate that parameter's impact on ice accretion (Block 6 of Table 6). Figure 34 shows the resulting ice accretions conducted at *AOA* = 0° (Panel (A)), *AOA* = 2° (Panel (B)), *AOA* = 4° (Panel (C)), and a repeat run at *AOA* = 4° (Panel (D)). Accreted ice mass increased with increasing *AOA*, where higher collision efficiency at the ramp base at a greater *AOA* was likely the reason for this trend. Figure 34 shows that ice accretions with shark teeth features were more prominent at larger angles of attack. No shark teeth ice features were observed for tests conducted at *AOA* = 0° (Panel (A)), a limited amount of shark teeth features appear at *AOA* = 2° (Panel (B)), and more prominent shark teeth features can be seen at *AOA* = 4° (Panels (C) and (D)). Repeatability was good as similar ice mass, location, and appearance accreted for the two tests conducted at *AOA* = 4°. The strut had little impact on ice accretion throughout the test. Compared to the *AOA* sweep in the previous subsection (Section 6.7),

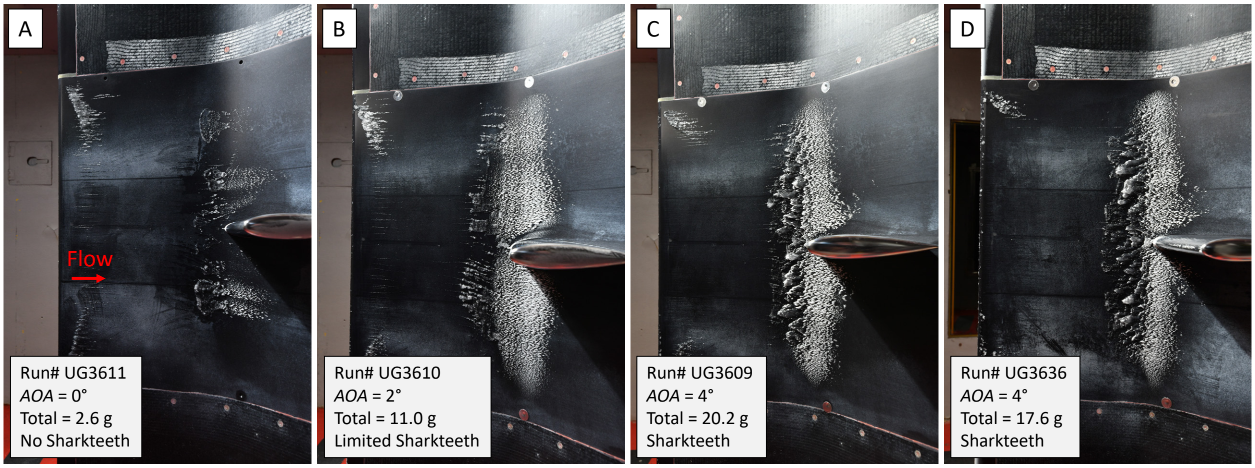

Figure 34.—End of test run images showing the resulting ice accretion from test runs conducted at (A) *AOA* = 0°, (B) *AOA* = 2°, (C) *AOA* = 4°, and (D) a repeat run at *AOA* = 4°.

this *AOA* sweep was conducted at a colder total air temperature (–20 vs. –15 °C), slower airspeed (152.5 vs. 207 knots), higher *IWC* (3.0 vs. 2.0 g/m^3) and larger *MVD* (41 vs. 28 µm), but with identical heater heat flux settings. Despite the differences in test conditions, the ice accretion mass, location, and appearance for all *AOA* test runs in this sweep were very similar to the respective test runs in the *AOA* sweep in the previous subsection. This may be, in part, because the surface energy balance at the ramp base was similar. The energy balance includes convection, conduction, evaporative mass transfer, and kinetic energy from impacting cloud particles. The slower airspeed (lower convective heat transfer) countered the colder total air temperature (greater convective heat transfer) between the two tests. The ice accretion process at the ramp base is complex as it requires bookkeeping energy and mass balances upstream from runback melt production, accounting for collision efficiency at all chord surfaces, and is transient in nature.

7.0 Heat Flux Icing Threshold Tests

7.1 Heat Flux Icing Threshold Objectives and General Test Matrix

A series of tests were conducted that investigated surface heat flux and the threshold values that differentiated between liquid runback (“running wet” conditions) and ice accretion. These heated surfaces when running wet act like an ice protection system. The tests provide data for heat transfer at surfaces that generate running wet conditions. Multiple objectives where set for these heat flux icing threshold tests and are listed below.

- Identify approximate minimum heat flux setting that produces full liquid melt/runback in each heater zone (with a focus on Zones 1 to 4) for an impinging icing cloud, and measure resulting surface temperatures.
- Conduct two supercooled liquid icing threshold tests at different airspeeds to compare heat fluxes and resulting icing measurements.
- Conduct two ice crystal icing threshold tests at different airspeeds to compare heat fluxes and resulting icing measurements.
- Conduct dry (no icing cloud) tests at same aerothermal conditions and heater settings conducted during the SCL and IC icing threshold tests and measure corresponding surface temperatures.

TABLE 9.—TEST CONDITIONS FOR THE TWO SCL AND TWO IC ICING THRESHOLD TESTS ARE SHOWN
[Multiple heat flux values were set in each heating zone to find the icing and running-wet threshold.]

Test run ID no.	Cloud type, SCL or IC	T_0, °C	U, knots	AOA, °	MVD, µm	TWC, g/m^3	Zone 1 heat flux, W/in^2	Zone 2 heat flux, W/in^2	Zone 3 heat flux, W/in^2	Zone 4 heat flux, W/in^2	Zone 5 heat flux, W/in^2	Zone 6 heat flux, W/in^2
UG3625	SCL	–6	152.5	0	30	0.44	Various	Various	Various	Various	Various	Various
UG3639	SCL	–6	207.0	0	30	0.44	Various	Various	Various	Various	Various	Various
UG3617	IC	–15	152.5	0	27	1.9	Various	Various	Various	Various	Various	Various
UG3618	IC	–15	207.0	0	28	2.0	Various	Various	Various	Various	Various	Various

Table 9 shows the four conditions that were tested for the heat flux threshold tests. The two SCL and two IC icing threshold tests were conducted at airspeeds of 152.5 and 207 knots. All other test conditions (T_0, AOA, MVD, and TWC) were held constant for the respective icing cloud tests. Due to limited characterized ice crystal icing clouds, small variations in MVD (27 vs. 28 µm) and TWC (1.9 vs. 2.0 g/m^3) exist between the two IC tests. Each test run utilized multiple heat flux settings and is indicated with “Various” in Table 9 for the six heater zones. After conducting the icing threshold tests, the same test conditions and heater settings were run without the icing cloud to record the corresponding surface temperatures in dry conditions for comparison.

7.2 Testing Procedures

The icing threshold tests began with all six heating zones of the SIDRM test article heated to elevated temperatures such that when the SCL or IC cloud was activated, there was full liquid runback on the main body. The heat flux was systematically reduced in intervals starting from the back end moving forward until that zone began to accrete ice. Each new heater setting was held for approximately 3 min until thermocouples read new steady state temperatures. The test was run as a continuous spray from one heater setting to the next, so only power to the heaters, heat flux gauge (not provided in this report), thermocouple, and visual data was acquired for these tests. The final accreted ice mass and ice shape geometry were not recorded for these tests. The general testing procedures for the heat flux icing threshold tests (icing cloud activated) are outlined below.

1. Run up IRT to target test airspeed and air temperature.
2. Activate SIDRM heaters to (elevated) target heat flux values and wait until thermocouples read steady values.
3. Start recording data 30 s prior to spray activation.
4. Turn on ice cloud (spray on).
5. Verify all heater zones ice free after initial (elevated) heater setting (all liquid runback).
6. Verify all thermocouple measurements read steady state for at least 30 s.
7. Reduce heat flux in aft sections of SIDRM until ice accretes in or near heater Zone 4.
8. Verify all thermocouple measurements read steady state for at least 30 s.
9. Reduce heat flux systematically moving forward (from Zone 3 to Zone 2 to Zone 1) until ice accretes in each respective zone and verify steady state thermocouple measurements for at least 30 s.
10. Turn off icing cloud (SIDRM heaters turned off simultaneously with spray off).
11. Continue holding tunnel airspeed and air temperature constant as data systems continue recording 30 s post spray.
12. Stop data recording systems and shut down drive fan.

13. Enter test section and take photographs of accreted ice.
14. Remove all ice from SIDRM and clean test article, preparing for next test point.

After the icing threshold tests were completed, the corresponding dry (no icing cloud) tests were conducted. The heater settings used during the icing threshold tests are repeated for these dry tests to measure the corresponding surface temperatures. The testing procedures for these dry tests are outlined below.

1. Run up IRT to target test airspeed and air temperature.
2. Activate SIDRM heaters to initial heat flux values and wait until thermocouples read steady values.
3. Start recording data.
4. Verify all thermocouple measurements read steady state for at least 30 s.
5. Reduce heat flux following the same order as was systematically done for the icing threshold tests, verifying steady state thermocouple measurements for at least 30 s at each heater setting.
6. After conducting final heater setting and holding for 30 s at steady state temperatures, turn off heaters.
7. Stop data recording systems and shut down drive fan.

7.3 Heat Flux Threshold Tests—Supercooled Liquid Icing at 152.5 knots

Table 10 provides heat flux values used during the SCL icing heat flux threshold test conducted at 152.5 knots (Run no. UG3625), with resulting icing descriptions and steady state surface temperatures. Data was collected for nine heater settings where heater settings listed “a” through “i” occurred chronologically. Efforts were made to systematically reduce heat flux setting from the highest (Heater Setting “a”) to lowest setting (Heater Setting “i”), however identifying the icing threshold methodically from Zone 4 to Zone 1 was imperfectly executed for this test run. Cells shaded in light green indicate the approximate heat flux threshold between icing and liquid runback in that heater zone. Table 10 shows how icing in Zone 2 unintentionally occurred first in the sequence. Despite that, it is not believed to have impacted the approximate heat flux icing threshold for the downstream zones. The corresponding steady state surface temperatures from the dry test runs (no icing cloud) are provided at the bottom half of the table. Note that not all heater settings conducted during the icing test run were conducted during the dry test runs. Icing threshold test runs with a corresponding dry test are indicated with a shaded orange cell in the first column of Table 10. As an example, there was a corresponding dry test run for Heater Setting “a”, but not for Heater Setting “b”. Of note, the thermocouple located at the centerline leading edge, T301, was not functioning properly during any of the heat flux threshold tests and is not provided in the tables in this section. Also, the thermocouple labeled T307 is located directly under the strut. Due to the absence of heating directly under the strut, T307 measured lower temperatures compared to surrounding thermocouples.

TABLE 10.—HEAT FLUX VALUES FOR ALL HEATER SETTINGS WITH A DESCRIPTION OF RESULTING ICE FOR THE SUPERCOOLED LIQUID ICING THRESHOLD TEST AT 152.5 KNOTS

[Several surface thermocouple temperature readings are provided for “wet” (exposed to icing cloud), and corresponding “dry” (no icing cloud) test conditions.]

	Heater settings							Steady state surface TC temperatures (during icing test run or for corresponding “dry” test run)															
Heater setting, letter	Zone 1 heat flux, W/in^2	Zone 2 heat flux, W/in^2	Zone 3 heat flux, W/in^2	Zone 4 heat flux, W/in^2	Zone 5 heat flux, W/in^2	Zone 6 heat flux, W/in^2	Zones where iced, heater zone	Zone 1		Zone 2				Zone 3				Zone 4			Zone 5		Zone 6
								T201, °C	T40, °C	T302, °C	T303, °C	T304, °C	T305, °C	T306, °C	T207, °C	T307, °C	T407, °C	T310, °C	T311, °C	T312, °C	T313, °C	T314, °C	T315, °C
Cloud on tests (“wet”)																							
a	7.1	2.1	2.8	3.7	6.4	4.5	Local strut	11.5	10.8	6.1	5.1	5.2	5.7	5.1	4.8	–0.1	4.5	5.4	6.9	8.0	21.0	25.8	28.2
b	5.5	1.7	2.3	3.2	6.4	4.5	Local strut	8.0	7.4	3.7	3.1	3.2	3.7	2.9	2.8	–1.2	2.5	3.5	4.8	6.2	21.2	26.5	28.7
c	4.2	1.3	1.8	2.6	6.4	4.5	Local strut	4.7	4.4	1.6	1.3	1.4	1.7	1.1	0.8	–2.1	0.5	1.7	3.4	5.1	22.0	27.3	28.9
d	3.5	1.2	1.8	2.6	6.4	4.5	2, 4, strut	3.1	2.8	0.5	–0.2	–0.2	0.4	0.3	0.2	–2.4	–0.1	1.5	3.2	5.1	22.7	28.1	29.1
e	3.5	1.2	1.8	2.2	6.3	4.5	2, 4, strut	3.0	2.8	0.4	–0.7	–0.9	–0.5	0.0	0.0	–2.5	–0.3	0.4	1.8	4.1	23.5	29.3	31.9
f	3.5	1.2	1.4	1.7	6.3	4.5	2, 3, 4	3.1	2.9	0.5	–0.8	–1.2	–1.2	–0.9	–1.1	–3.1	–1.5	–1.1	0.3	2.9	23.6	30.3	34.2
g	2.5	1.2	1.4	1.7	2.7	2.8	2, 3, 4	1.2	1.1	0.1	–0.9	–1.3	–1.4	–1.0	–1.4	–3.1	–1.8	–1.4	–0.3	1.1	10.6	13.9	24.0
h	1.6	1.2	1.4	1.7	1.9	1.9	2, 3, 4	0.4	0.3	–0.6	–0.8	–1.1	–1.5	–1.0	–1.4	–3.2	–1.8	–1.6	–0.9	–0.3	4.3	5.9	14.1
i	1.2	1.2	1.4	1.5	1.3	1.3	1, 2, 3, 4	–0.2	–0.3	–1.1	–0.9	–1.1	–1.5	–1.1	–1.5	–3.3	–1.8	–2.3	–1.6	–1.2	1.4	2.4	8.3
Cloud off tests (“dry”)																							
a	7.1	2.1	2.8	3.7	6.3	4.4	N/A	22.0	21.3	14.5	13.1	13.3	14.1	14.2	12.8	7.3	12.7	11.0	11.7	12.6	26.4	30.7	38.9
c	4.2	1.3	1.8	2.6	6.3	4.4	N/A	11.0	10.6	6.8	6.1	6.4	7.2	7.6	6.8	3.1	6.7	6.0	6.6	7.9	24.6	29.6	38.2
d	3.5	1.2	1.8	2.6	6.3	4.4	N/A	8.6	8.3	5.1	4.6	5.0	6.0	6.8	6.3	2.6	6.1	5.8	6.3	7.6	24.4	29.4	38.1
e	3.5	1.2	1.8	2.2	6.3	4.4	N/A	8.5	8.1	4.9	4.5	4.9	5.8	6.6	6.1	2.5	6.0	4.6	4.8	6.2	24.1	29.2	38.0
f	3.5	1.2	1.4	1.7	6.3	4.4	N/A	8.5	8.1	4.9	4.3	4.5	5.0	5.0	4.2	1.2	4.1	2.7	2.9	4.4	23.4	28.8	37.8
g	2.5	1.2	1.4	1.7	2.7	2.8	N/A	5.2	4.9	3.3	3.4	3.9	4.5	4.5	3.9	0.9	3.7	2.3	2.1	2.4	8.6	10.3	21.8
i	1.2	1.2	1.4	1.5	1.3	1.3	N/A	1.3	1.2	1.3	2.4	3.2	4.0	4.2	3.5	0.6	3.4	1.6	1.2	1.1	2.1	2.5	8.1

Figure 35 graphically shows the heat flux settings and resulting surface temperatures of representative thermocouples in heating Zones 1 to 4 from Table 10. Panels (B) and (A), respectively, show the heat flux and resulting temperatures for Zones 1 to 4 when the SCL cloud was activated (“wet”). Similarly, Panels (D) and (C), respectively, show the corresponding heat fluxes and surface temperatures for the “dry” tests (no cloud). Heater settings listed “a” through “i” occurred chronologically. To avoid repeating descriptions of this figure layout again, each of the remaining subsections in this section (Section 7.0) will have the same figure layout presented. Both Figure 35 and Table 10 show that surface temperatures of heating zones where ice accretion occurred were near or below freezing values (see second row of table for thermocouple and heater zone relations). They also shows that cloud activated temperatures are lower than dry temperatures for identical heater settings. This is expected as the surface for running-wet tests experienced the additional evaporative cooling energy flux in addition to the convective cooling heat flux at the surface.

Figure 36 shows snapshots of ice accretions throughout the duration of the SCL icing heat flux threshold test conducted at 152.5 knots. Panel (A) shows the approximate location of Heating Zones 1 to 4 with transparently colored boxes, along with the representative thermocouple location in each zone for reference. Panel (A) shows ice that had accreted in Zone 2 for heater setting “d”. As mentioned earlier, the intent was to systematically work back to front, but the icing threshold was unintentionally reached first in Zone 2 . Ice had also accreted locally around the strut in Panel (A). The absence of a thin film heater directly under the struts resulted in a colder surface around the struts if the Zone 3 heater was activated. For these tests, Zone 3 was only considered iced if there was ice that had accreted lateral to and away from the struts. Ice accreted on the unheated extensions, and on the leading edge of the struts, but are not considered for these tests as the focus was the heated main body. Panel (B) shows Heater Setting “e”, where icing was observed to occur in Zone 4. Zone 3 was still considered clear of ice for Heater Setting “e”. Panel (C) shows Heater Setting “f”, where the Zone 3 heat flux was reduced sufficiently to result in ice in that zone (now Zones 2, 3, and 4 are iced). Panel (D) shows Heater Setting “i”, where Zone 1 became iced.

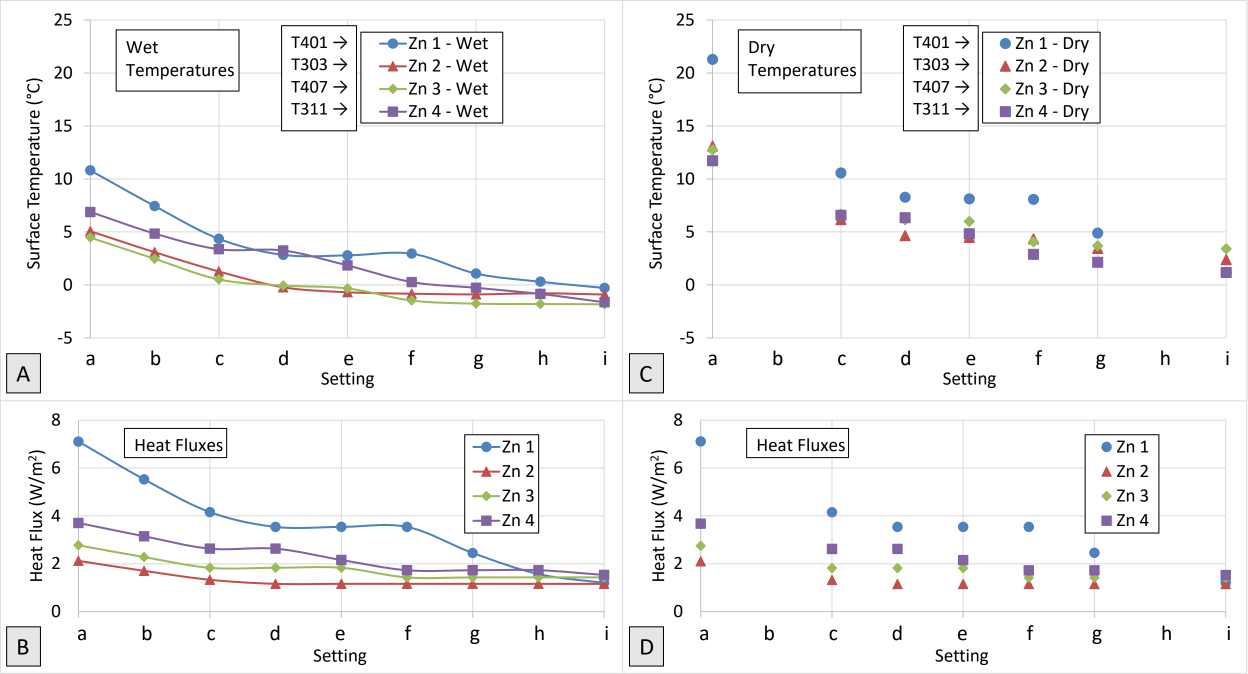

Figure 35.—(A) Representative wet surface temperatures for Zones 1 to 4, (B) resulting from the various heat flux settings tested, (C) along with the corresponding dry surface temperatures (D) for the same heat flux settings for the SCL icing threshold test conducted at 152.5 knots.

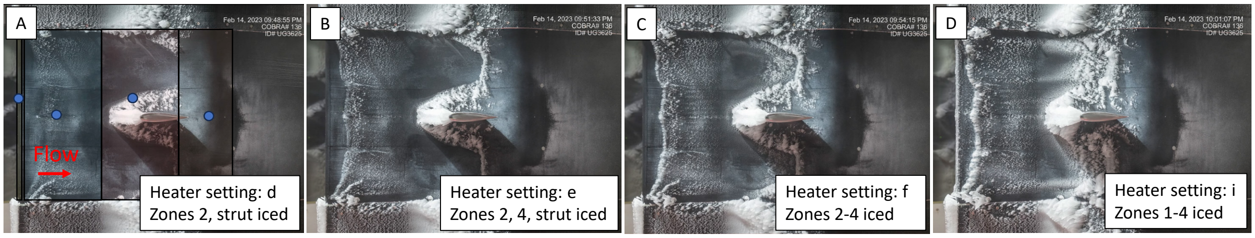

Figure 36.—A sequence of ice accretions resulting from the supercooled liquid icing threshold test at 152.5 knots (Run no. UG3625), where the heat flux was largely systematically reduced in intervals from the back end moving forward (from Panel A to D).

7.4 Heat Flux Threshold Tests—Supercooled Liquid Icing at 207 knots

Table 11 provides heat flux values used during the SCL icing heat flux threshold test conducted at 207 knots (Run no. UG3639), with resulting icing descriptions and steady state surface temperatures. Data was collected for 16 heater settings that were systematically reduced from the highest heat flux setting (Heater Setting “a”) to lowest flux setting (Heater Setting “p”). Again, not all heater settings conducted during the icing test run have a corresponding dry test run. Those that do are indicated with a shaded orange cell in the first column. Cells shaded in light green indicate the approximate heat flux threshold between icing and liquid runback in that heater zone.

Figure 37 graphically shows the heat flux settings and resulting surface temperatures of representative thermocouples in heating Zones 1 to 4 from Table 11. As before, both Figure 37 and Table 11 show that surface temperatures of heating zones where ice accretion occurred were near or below freezing values. Similarly, the table also shows that cloud activated temperatures are lower than dry temperatures for identical heater settings due to the additional evaporative cooling at the surface. The icing threshold heat flux values in Zones 1, 2, and 3 are greater for this higher airspeed test run compared to the 152.5 knot test run in the previous subsection (Section 7.3). This is inline when considering the energy balance at those surfaces. The greater airspeed increased convective heat transfer from the heated surface. Therefore, a greater supply of heat is required to elevate the surface temperatures high enough above freezing to keep the impinging supercooled liquid cloud as a runback liquid. In addition, the water mass flow rate of the freestream icing cloud was about 36% greater for the higher airspeed test (for the same *TWC*, the water mass flow rate will be the ratio of airspeeds of 207 to 152.5 knots). This too will require a greater supply of heat to keep the greater impinging water mass flux as a runback liquid on the surfaces. The icing threshold heat flux for Zone 4 was equal (2.2 W/m^2) between the two airspeed test runs. It is possible that the Zone 4 threshold value for the 207 knot test run is higher than what was measured. The heat flux step decrement taken in Zone 4 was large (from 2.9 to 2.2 W/m^2 for Heater Setting “f” to “g”), and it is possible that a more accurate threshold value is greater than what was determined.

Figure 38 shows the sequence of ice accretions throughout the duration of the SCL icing threshold test conducted at 207 knots. The snapshots show the heater setting at which the heat flux threshold between how icing and liquid runback was crossed. The figure shows how ice accreted in Zone 4 in Panel (A), and then progressed forward at sequentially lower heat flux settings in Zones 3, 2, and then 1 in Panels (B), (C), and (D), respectively.

TABLE 11.—HEAT FLUX VALUES FOR ALL HEATER SETTINGS WITH A DESCRIPTION OF RESULTING ICE FOR THE SUPERCOOLED LIQUID ICING THRESHOLD TEST AT 207 KNOTS

[Several surface thermocouple temperature readings are provided for “wet” (exposed to icing cloud), and corresponding “dry” (no icing cloud) test conditions.]

	Heater settings							Steady state surface TC temperatures (during icing test run or for corresponding “dry” test run)															
Heater setting, letter	Zone 1 heat flux, W/in^2	Zone 2 heat flux, W/in^2	Zone 3 heat flux, W/in^2	Zone 4 heat flux, W/in^2	Zone 5 heat flux, W/in^2	Zone 6 heat flux, W/in^2	Zones where iced, heater zone	Zone 1		Zone 2				Zone 3				Zone 4			Zone 5		Zone 6
								T201, °C	T40, °C	T302, °C	T303, °C	T304, °C	T305, °C	T306, °C	T207, °C	T307, °C	T407, °C	T310, °C	T311, °C	T312, °C	T313, °C	T314, °C	T315, °C
Cloud on tests (“wet”)																							
a	15.4	3.6	3.9	5.3	6.4	4.5	All clear	23.4	21.9	13.0	11.0	11.1	10.5	7.7	6.8	1.0	6.0	6.7	8.1	9.0	17.3	20.3	22.2
b	13.0	3.4	4.2	5.0	5.7	3.9	All clear	19.2	18.0	10.2	8.5	8.7	8.5	6.7	6.5	1.1	5.7	6.4	7.3	7.9	15.0	17.7	18.9
c	10.8	3.1	4.2	4.6	5.0	3.3	All clear	15.8	14.7	8.2	6.9	7.1	6.8	6.0	6.1	1.1	5.5	5.9	6.6	7.1	13.1	15.3	16.1
d	8.9	2.6	4.2	4.0	4.4	2.8	All clear	12.2	11.3	5.7	4.7	4.8	4.6	5.2	5.7	0.9	5.1	4.5	4.7	5.0	10.5	12.4	12.5
e	7.1	2.1	4.2	3.4	3.8	2.4	All clear	8.8	8.0	3.5	2.7	2.9	2.7	4.6	5.4	0.8	4.6	3.7	3.3	3.5	8.3	9.9	9.5
f	5.5	2.1	4.2	2.9	3.3	1.9	All clear	6.1	5.5	2.4	2.2	2.5	2.2	4.5	5.2	0.8	4.5	2.4	1.6	1.7	6.0	7.4	6.2
g	4.8	1.9	4.2	2.2	2.8	1.5	4	4.6	4.0	1.4	1.3	1.6	1.3	4.2	4.9	0.7	4.3	1.1	–0.8	–1.3	2.8	4.6	4.0
h	4.8	1.9	3.6	2.2	2.5	1.3	4	4.5	4.1	1.4	1.3	1.4	0.6	2.9	3.6	0.0	3.0	0.4	–1.7	–1.8	1.3	2.9	2.3
i	4.8	1.9	3.1	2.2	2.3	1.2	4	4.6	4.1	1.4	1.3	1.2	0.1	2.4	2.4	–0.4	2.1	–0.7	–1.9	–2.4	0.9	2.3	1.5
j	4.8	1.9	2.5	2.2	2.3	1.2	4	4.6	4.1	1.4	1.3	1.2	0.0	1.7	1.6	–0.9	1.2	–1.0	–1.7	–2.1	0.6	2.1	1.2
k	4.8	1.9	2.1	2.2	2.3	1.2	3, 4	4.6	4.2	1.5	1.4	1.3	0.0	0.9	0.8	–1.5	0.6	–1.2	–1.8	–2.3	0.4	2.0	1.2
l	4.8	1.9	1.6	2.2	2.3	1.2	3, 4	4.6	4.1	1.5	1.4	1.2	–0.1	0.1	–0.1	–2.3	–0.5	–2.1	–2.2	–2.0	1.6	3.2	0.8
m	4.2	1.5	1.6	2.2	2.3	1.2	2, 3, 4	3.3	2.8	0.1	–0.6	–0.4	–0.6	–0.1	–0.6	–2.5	–1.3	–1.9	–1.6	–1.3	2.2	3.9	0.9
n	3.0	1.5	1.6	2.2	2.3	1.2	2, 3, 4	1.2	0.9	–0.9	–1.3	–1.2	–0.9	–0.1	–0.8	–2.5	–1.5	–1.8	–1.4	–1.1	2.4	3.9	1.2
o	2.0	1.5	1.6	2.2	2.3	1.2	1, 2, 3, 4	0.2	0.1	–1.6	–1.6	–1.3	–1.0	–0.1	–0.9	–2.6	–1.5	–1.8	–1.4	–1.1	2.5	4.1	1.1
p	1.6	1.5	1.6	2.2	2.3	1.2	1, 2, 3, 4	–0.4	–0.2	–1.7	–1.5	–1.3	–1.0	–0.1	–1.0	–2.6	–1.4	–1.7	–1.3	–1.1	2.6	4.2	1.5
Cloud off tests (“dry”)																							
a	15.3	3.6	3.9	5.3	6.4	4.5	N/A	41.8	41.1	25.1	20.9	20.1	19.9	18.4	15.6	8.1	15.5	12.9	13.7	13.9	21.4	24.0	30.2
b	13.0	3.3	4.2	4.9	5.7	3.9	N/A	35.8	35.0	21.8	18.7	18.6	19.3	19.1	16.8	9.2	16.6	12.8	12.9	13.0	19.1	21.2	26.5
d	8.9	2.6	4.2	4.0	4.4	2.8	N/A	23.6	22.9	14.4	12.8	13.4	15.3	17.1	15.9	8.7	15.6	10.5	9.7	9.5	14.0	15.4	18.3
f	5.5	2.1	4.2	2.9	3.3	1.9	N/A	13.7	13.2	8.7	8.5	9.8	12.4	15.5	14.9	8.0	14.6	7.7	5.9	5.6	9.0	10.0	11.0
h	4.8	1.9	3.6	2.2	2.5	1.3	N/A	11.3	10.8	6.9	6.9	8.0	10.2	12.8	12.2	6.2	11.8	5.1	3.1	2.8	5.6	6.3	6.4
k	4.8	1.9	2.0	2.2	2.3	1.2	N/A	11.3	10.8	6.9	6.6	7.0	7.5	7.4	6.0	2.1	5.6	2.7	1.8	1.7	4.1	4.9	4.6
l	4.8	1.9	1.6	2.2	2.3	1.2	N/A	11.2	10.8	6.8	6.5	6.8	6.8	5.9	4.3	1.0	3.9	2.1	1.4	1.4	3.9	4.7	4.4
m	4.2	1.5	1.6	2.2	2.3	1.2	N/A	8.7	8.3	4.7	4.3	4.6	4.9	4.8	3.6	0.5	3.3	1.8	1.2	1.2	3.7	4.6	4.2
n	3.0	1.5	1.6	2.2	2.3	1.2	N/A	5.5	5.2	3.3	3.6	4.1	4.6	4.6	3.4	0.4	3.1	1.7	1.1	1.1	3.6	4.5	4.1
o	2.0	1.5	1.6	2.2	2.3	1.2	N/A	2.9	2.7	2.1	3.0	3.7	4.3	4.4	3.3	0.3	2.9	1.6	1.0	1.0	3.5	4.4	4.1
p	1.6	1.5	1.6	2.2	2.3	1.2	N/A	1.7	1.5	1.5	2.6	3.5	4.1	4.2	3.2	0.3	2.8	1.5	0.9	1.0	3.5	4.4	4.0

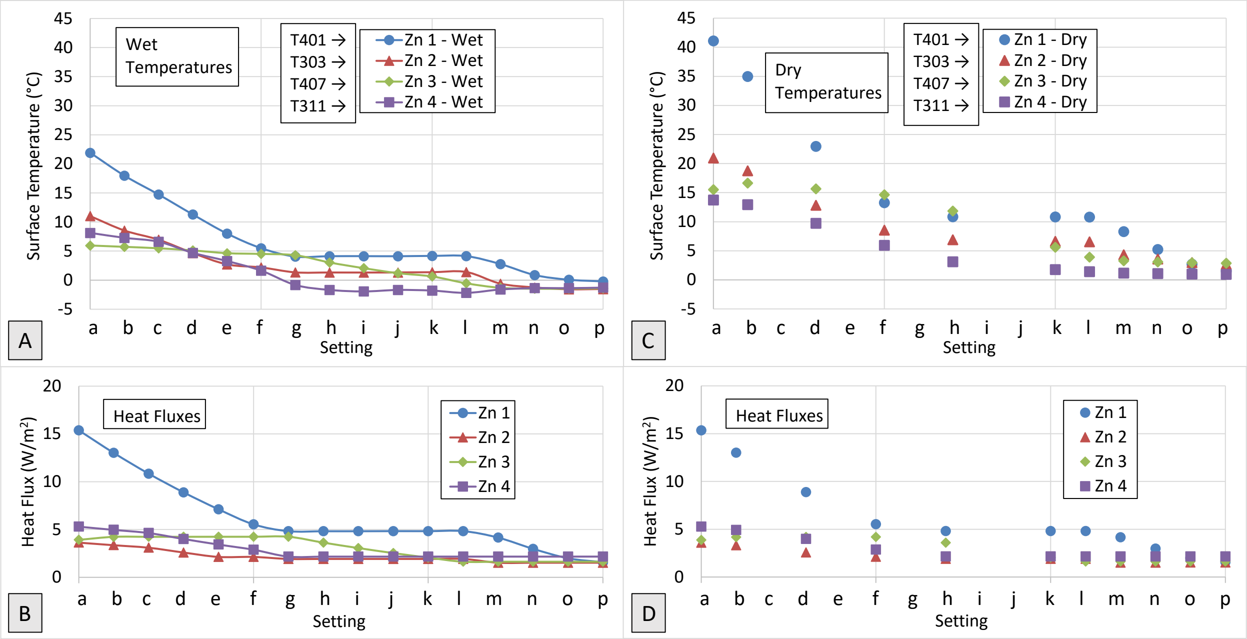

Figure 37.—(A) Representative wet surface temperatures for Zones 1 to 4, (B) resulting from the various heat flux settings tested, (C) along with the corresponding dry surface temperatures (D) for the same heat flux settings for the SCL icing threshold test conducted at 207 knots.

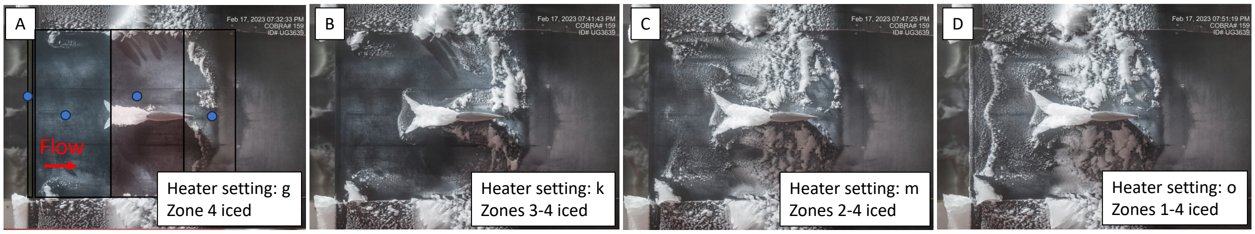

Figure 38.—A sequence of ice accretions resulting from the supercooled liquid icing threshold test at 207 knots (Run no. UG3639), where the heat flux was systematically reduced in intervals from the back end moving forward (from Panel (A) to (D)).

7.5 Heat Flux Threshold Tests—Ice Crystal Icing at 152.5 knots

Table 12 provides heat flux values used during the ice crystal icing heat flux threshold test conducted at 152.5 knots (Run no. UG3617), with resulting icing descriptions and steady state surface temperatures. Data was collected for 14 heater settings that were systematically reduced from the highest heat flux setting (Heater Setting "a") to lowest flux setting (Heater Setting "n"). A corresponding dry test run was conducted for all heater settings performed during the icing test runs. Cells shaded in light green indicate the approximate heat flux threshold between icing and liquid runback in that heater zone. Ice accretion was observed to occur only in Zones 2 and 3 and the threshold is reflected in the table with just two light green shaded cells.

TABLE 12.—HEAT FLUX VALUES FOR ALL HEATER SETTINGS WITH A DESCRIPTION OF RESULTING ICE FOR THE ICE CRYSTAL ICING THRESHOLD TEST AT 152.5 KNOTS

[Several surface thermocouple temperature readings are provided for “wet” (exposed to icing cloud), and corresponding “dry” (no icing cloud) test conditions.]

	Heater settings							Steady state surface TC temperatures (during icing test run or for corresponding “dry” test run)															
Heater setting, letter	Zone 1 heat flux, W/in^2	Zone 2 heat flux, W/in^2	Zone 3 heat flux, W/in^2	Zone 4 heat flux, W/in^2	Zone 5 heat flux, W/in^2	Zone 6 heat flux, W/in^2	Zones where iced, heater zone	Zone 1		Zone 2				Zone 3				Zone 4			Zone 5		Zn 6
								T201, °C	T40, °C	T302, °C	T303, °C	T304, °C	T305, °C	T306, °C	T207, °C	T307, °C	T407, °C	T310, °C	T311, °C	T312, °C	T313, °C	T314, °C	T315, °C
Cloud on tests (“wet”)																							
a	9.8	4.2	5.6	5.6	6.0	3.9	Local strut	10.7	9.3	11.2	13.3	15.2	15.8	11.0	6.3	–0.9	6.4	9.5	10.7	11.3	17.8	20.3	23.0
b	8.9	3.9	6.3	5.6	6.0	3.9	Local strut	7.8	6.8	8.7	10.9	13.1	14.7	11.7	7.0	–0.3	9.3	9.9	10.6	11.0	17.5	20.0	22.4
c	8.9	3.4	7.1	5.0	6.0	3.9	Local strut	6.4	5.7	6.3	8.0	10.2	13.0	12.1	8.0	0.6	10.4	8.9	8.6	9.1	17.1	19.6	21.4
d	8.0	2.8	7.5	4.6	5.0	3.3	Local strut	2.8	2.4	3.4	4.8	7.1	10.9	11.6	9.3	0.9	10.1	8.3	7.4	7.5	13.1	14.9	17.0
e	7.1	2.4	6.7	4.0	4.4	2.8	Local strut	2.9	2.2	1.5	2.3	4.2	7.7	8.9	5.8	–0.3	8.1	5.9	4.8	4.9	10.0	11.5	12.5
f	6.3	2.4	6.3	3.7	3.8	2.3	Local strut	2.4	1.9	1.2	2.0	3.9	7.1	7.9	4.7	–0.9	6.8	4.6	3.4	3.4	7.4	8.5	9.0
g	6.3	2.4	5.6	3.7	3.3	1.9	Local strut	2.5	1.9	1.2	1.9	3.5	5.7	4.4	2.5	–2.3	3.0	3.5	2.7	2.7	4.9	5.6	5.4
h	6.3	2.4	4.9	3.4	2.8	1.5	Lateral of strut	2.4	1.9	1.1	1.8	3.1	4.7	3.0	1.1	–3.5	1.2	2.2	1.5	1.5	2.8	3.3	2.6
i	6.3	2.4	4.2	3.4	2.8	1.5	Lateral of strut	2.4	1.8	1.1	1.6	2.7	3.7	1.6	–0.2	–4.5	–0.1	1.5	1.0	0.9	2.3	2.8	1.8
j	6.3	2.4	3.6	3.4	2.8	1.5	Lateral of strut	2.2	1.9	1.0	1.5	2.3	2.5	0.2	–1.4	–5.6	–1.4	0.7	0.5	0.4	1.9	2.5	1.5
k	6.3	2.4	3.1	3.4	2.8	1.5	3	2.3	1.8	1.0	1.4	1.9	1.7	–1.0	–2.6	–6.5	–2.5	0.1	0.0	0.1	1.5	2.3	1.3
l	6.3	1.9	3.1	3.4	2.8	1.5	2, 3	2.0	1.6	–0.3	–0.1	0.3	0.2	–1.8	–2.8	–6.8	–2.7	–0.1	–0.1	–0.1	1.3	2.1	1.2
m	4.8	1.9	3.1	3.4	2.8	1.5	2, 3	1.2	0.9	–1.1	–0.5	0.1	0.1	–1.8	–2.6	–6.8	–2.6	–0.1	–0.1	–0.1	1.3	2.1	1.2
n	3.5	1.9	3.1	3.4	2.8	1.5	2, 3	–0.9	–0.8	–2.0	–1.1	–0.2	0.1	–1.7	–2.5	–6.8	–2.4	–0.1	–0.1	–0.1	1.3	2.1	1.1
Cloud off tests (“dry”)																							
a	9.8	4.2	5.5	5.6	6.0	3.9	N/A	27.1	26.2	19.0	18.9	20.5	22.7	23.2	20.4	10.0	20.5	13.0	13.1	12.9	19.9	22.5	26.1
b	8.9	3.9	6.3	5.6	6.0	3.9	N/A	23.5	22.7	16.5	16.8	18.9	22.5	25.2	23.3	11.9	23.4	14.2	13.7	13.2	20.1	22.6	26.2
c	8.9	3.3	7.0	4.9	6.0	3.9	N/A	21.8	21.0	14.1	13.8	16.1	21.2	26.6	26.1	13.7	26.3	13.6	11.9	11.4	19.8	22.5	26.1
d	8.0	2.8	7.4	4.6	5.0	3.3	N/A	17.7	17.0	10.4	10.2	12.9	19.2	26.6	27.3	14.6	27.5	13.3	10.9	9.9	15.5	17.2	21.0
e	7.1	2.3	6.6	4.0	4.4	2.8	N/A	13.7	13.1	7.0	6.5	8.9	14.8	22.1	23.0	11.8	23.1	10.1	7.7	6.8	11.8	13.3	15.8
f	6.3	2.4	6.3	3.7	3.8	2.4	N/A	10.9	10.2	5.3	5.3	7.6	13.0	19.5	20.2	9.5	20.3	8.1	5.7	4.8	8.4	9.6	10.6
g	6.3	2.4	5.5	3.7	3.3	1.9	N/A	11.1	10.4	5.5	5.4	7.3	11.8	17.1	17.3	7.7	17.3	7.0	5.1	4.2	6.0	6.7	6.9
h	6.3	2.4	4.9	3.4	2.8	1.5	N/A	11.1	10.4	5.5	5.2	6.9	10.5	14.4	14.1	5.6	14.0	5.1	3.4	2.6	3.4	3.8	3.2
i	6.3	2.4	4.2	3.4	2.8	1.5	N/A	11.0	10.4	5.4	5.0	6.3	9.0	11.8	11.0	3.5	10.9	3.9	2.7	2.0	2.9	3.4	2.7
j	6.3	2.4	3.6	3.4	2.8	1.5	N/A	11.0	10.3	5.3	4.8	5.7	7.6	9.1	7.8	1.2	7.7	2.5	1.9	1.4	2.5	3.1	2.4
k	6.3	2.4	3.0	3.4	2.8	1.5	N/A	11.0	10.3	5.2	4.6	5.3	6.4	6.8	5.2	–0.6	5.0	1.5	1.3	1.0	2.2	2.9	2.2
l	6.3	1.9	3.1	3.4	2.8	1.5	N/A	9.8	9.1	3.3	2.1	2.6	4.1	5.4	4.4	–1.3	4.2	1.2	1.0	0.7	2.0	2.6	2.0
m	4.8	1.9	3.1	3.4	2.8	1.5	N/A	5.4	4.9	1.2	1.0	1.9	3.6	5.0	4.1	–1.5	4.0	1.0	0.9	0.6	1.9	2.6	1.9
n	3.5	1.9	3.1	3.4	2.8	1.5	N/A	1.5	1.1	–0.7	0.0	1.2	3.2	4.7	3.9	–1.6	3.8	0.9	0.8	0.5	1.8	2.5	1.9

Figure 39 graphically shows the heat flux settings and resulting surface temperatures of representative thermocouples in heating Zones 1 to 4 from Table 12. Both Figure 39 and Table 12 show that surface temperatures for Zones 2 and 3 were near or below freezing values when ice accretion occurred. The table also shows that cloud activated temperatures are lower than dry temperatures for identical heater settings due to the additional evaporative cooling at the surface.

Figure 40 shows snapshots of ice accretions throughout the duration of the IC icing threshold test conducted at 152.5 knots. Panels (A) and (B) show how the main body is clear of ice except for locally around the strut for Heater Settings “g” and “h”. Again, Zone 3 was only considered iced if there was ice that had accreted lateral to and away from the struts. Panel (C) shows Heater Setting “k”, where icing was observed to occur in Zone 3. Ice accretion progressed forward into Zone 2 and is shown in Panel (D). Decreasing heat flux in Zone 1 did not result in any observed icing in the middle section of the span (ice near the extensions is neglected). When sufficiently warm, Zone 1 is generally used to generate liquid melt for accretion to occur in downstream zones. When Zone 1 heat flux was sufficiently reduced, the surface temperatures were too cool to produce melt and the impinging ice crystals simply bounced off the small radius surface. Ice accretion in Zone 4 was not observed as this area is aft of the strut and represents the thickest area of the test article where air speeds accelerate resulting in greater shear at the surface. The changing geometry into a convex surface is also less conducive to ice crystal icing in Zone 4.

It should be noted the limitations in conducting these ice crystal heat flux threshold tests. These tests were performed sequentially between different heater settings, with the cloud running continuously. As had been previously reported by Bartkus (Ref. 35), due to the closed loop wind tunnel, ice crystal clouds recirculated and *IWC* slowly increased over extended periods of spray time. These tests were performed as efficiently as possible to minimize *IWC* drift. Best efforts were taken during testing to run heat flux decrements between settings to reduce overall time and achieve sufficiently fine enough steps to identify the thresholds.

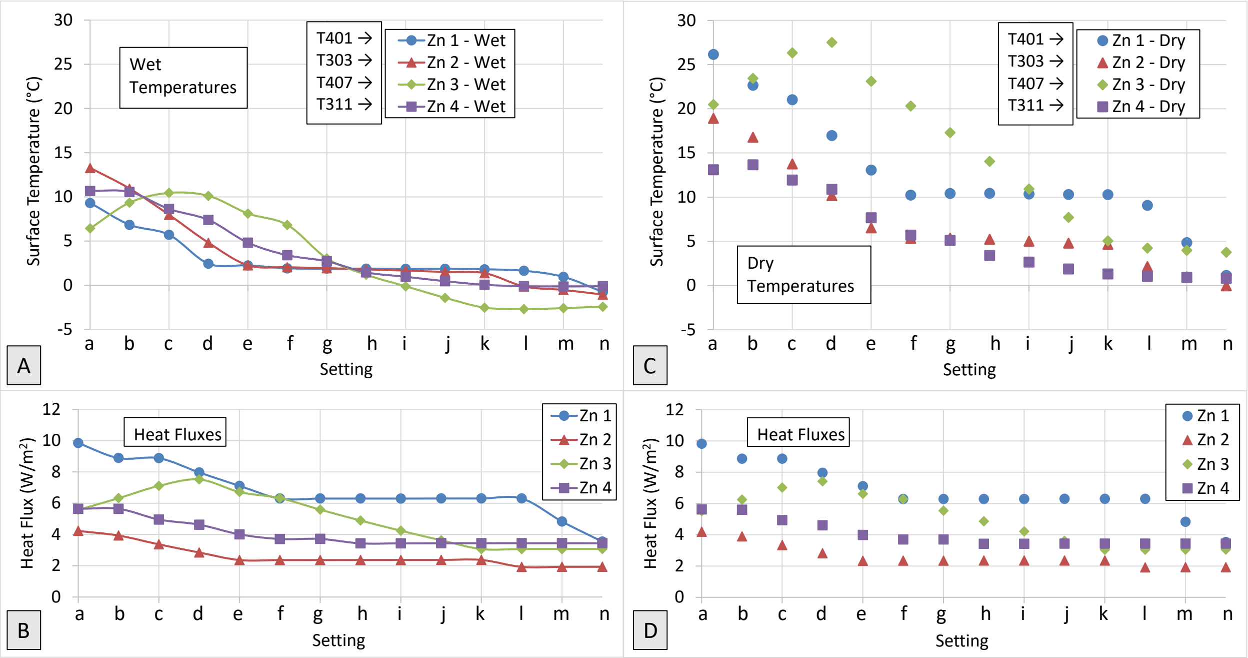

Figure 39.—(A) Representative wet surface temperatures for Zones 1 to 4, (B) resulting from the various heat flux settings tested, (C) along with the corresponding dry surface temperatures (D) for the same heat flux settings for the IC icing threshold test conducted at 152.5 knots.

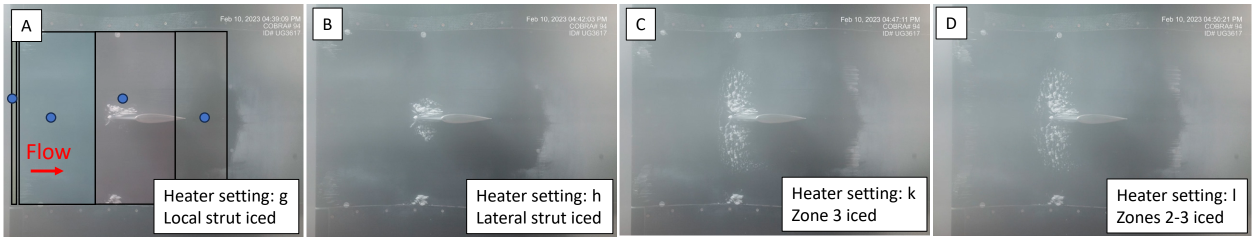

Figure 40.—A sequence of ice accretions resulting from the ice crystal icing threshold test at 152.5 knots (Run no. UG3617), where the heat flux was systematically reduced in intervals from the back end moving forward (from Panel (A) to (D)).

7.6 Heat Flux Threshold Tests—Ice Crystal Icing at 207 knots

Table 13 provides heat flux values used during the IC icing heat flux threshold test conducted at 207 knots (Run no. UG3618), with resulting icing descriptions and steady state surface temperatures. Data was collected for 13 heater settings that were systematically reduced from the highest heat flux setting (Heater Setting “a”) to lowest flux setting (Heater Setting “m”). A corresponding dry test run was conducted for all heater settings performed during the icing test runs. Ice accretion occurred only in Zone 3, and the heat flux threshold is reflected in the table with just the single light green shaded cell.

Figure 41 graphically shows the heat flux settings and resulting surface temperatures of representative thermocouples in heating Zones 1 to 4 from Table 13. Both Figure 41 and Table 13 shows that surface temperatures for Zone 3 were below freezing values when ice accreted. The table also shows that cloud activated temperatures are lower than dry temperatures for identical heater settings due to the additional evaporative cooling at the surface. The same heat flux setting was conducted for the final heater setting for the 207 knot test run (Heater setting “m”) and 152.5 knot test run (Heater setting “n”). Comparing the surface temperatures between those corresponding dry test runs, temperatures were lower for the faster airspeed tests. Again, the greater airspeed increased convective heat transfer from the heated surface, reducing the surface temperatures.

Figure 42 shows snapshots of ice accretions throughout the duration of the IC icing threshold test conducted at 207 knots. Panel (A) shows negligible ice at the strut and Panel (B) shows a small amount of ice growth local to the strut. Panel (C) shows Heater Setting “j”, where icing is considered to have accreted in Zone 3. Faint streaks of ice are visible and pointed out in Panel (C). Decreasing heat flux in Zones 1 and 2 did not result in any observed icing in the middle section of the span (ice near the extensions is neglected). Overall, very little ice accreted for this IC icing threshold test run. The elevated airspeed of 207 knots may have caused more particle bounce and reduced sticking to the surface, resulting in a small amount of ice accretion.

TABLE 13.—HEAT FLUX VALUES FOR ALL HEATER SETTINGS WITH A DESCRIPTION OF RESULTING ICE FOR THE ICE CRYSTAL ICING THRESHOLD TEST AT 207 KNOTS

[Several surface thermocouple temperature readings are provided for “wet” (exposed to icing cloud), and corresponding “dry” (no icing cloud) test conditions.]

	Heater settings							Steady state surface TC temperatures (during icing test run or for corresponding “dry” test run)															
Heater setting, letter	Zone 1 heat flux, W/in^2	Zone 2 heat flux, W/in^2	Zone 3 heat flux, W/in^2	Zone 4 heat flux, W/in^2	Zone 5 heat flux, W/in^2	Zone 6 heat flux, W/in^2	Zones where iced, heater zone	Zone 1		Zone 2				Zone 3				Zone 4			Zone 5		Zone 6
								T201, °C	T40, °C	T302, °C	T303, °C	T304, °C	T305, °C	T306, °C	T207, °C	T307, °C	T407, °C	T310, °C	T311, °C	T312, °C	T313, °C	T314, °C	T315, °C
Cloud on tests (“wet”)																							
a	9.9	4.5	8.3	6.0	6.1	3.9	Negligible	5.7	5.2	6.7	9.5	12.8	17.0	18.8	19.1	6.2	19.3	12.0	10.6	10.2	14.1	15.3	18.3
b	8.9	3.9	7.5	5.3	5.1	2.8	Negligible	3.4	2.8	4.1	6.4	9.2	13.4	15.8	15.5	4.3	16.5	9.0	7.5	7.2	10.0	10.8	11.3
c	8.9	3.7	6.7	4.6	4.4	2.4	Negligible	3.1	2.7	3.4	5.2	7.6	10.8	11.7	12.5	1.9	12.6	6.4	4.8	4.6	7.1	7.7	7.1
d	8.0	3.4	6.0	4.0	3.8	1.9	Negligible	2.7	2.4	2.5	3.9	5.9	8.6	9.3	9.1	0.2	9.1	3.9	2.2	2.1	4.3	4.8	3.6
e	7.1	3.1	5.2	3.4	3.3	1.5	Negligible	2.2	1.9	1.5	2.8	4.5	6.8	6.5	6.5	–1.4	7.1	1.5	–0.4	–0.4	1.7	2.0	0.3
f	7.1	2.9	4.6	3.4	3.0	1.5	Local strut	2.1	1.8	0.9	1.7	3.2	5.2	5.3	4.4	–2.4	4.8	0.6	–0.8	–0.8	0.5	0.7	–0.4
g	7.1	2.9	3.9	3.4	3.0	1.5	Local strut	2.1	1.8	0.8	1.6	2.8	3.8	2.0	1.4	–4.1	2.1	–0.3	–1.3	–1.2	0.2	0.5	–0.7
h	7.1	2.9	3.3	3.4	3.0	1.5	Local strut	2.0	1.8	0.8	1.5	2.4	2.5	0.2	–0.7	–5.5	–0.3	–1.2	–1.9	–1.7	–0.1	0.3	–0.9
i	7.1	2.9	2.8	3.4	3.0	1.5	Local strut	2.0	1.8	0.7	1.5	2.1	1.9	–0.6	–1.9	–6.4	–2.0	–2.1	–2.5	–2.2	–0.5	0.1	–1.0
j	7.1	3.1	2.3	3.4	3.0	1.5	3	2.2	1.8	1.3	2.2	2.9	2.1	–1.3	–3.3	–7.3	–3.5	–2.8	–2.9	–2.5	–0.7	–0.1	–1.1
k	5.5	3.1	2.3	3.4	3.0	1.5	3	1.5	1.3	1.1	2.5	3.2	2.4	–1.0	–3.0	–7.3	–3.3	–2.9	–2.9	–2.6	–0.8	–0.2	–1.2
l	4.2	2.6	2.3	3.4	3.0	1.5	3	0.5	0.4	–0.4	0.7	1.4	1.3	–1.0	–2.6	–7.1	–2.9	–2.8	–2.9	–2.6	–0.8	–0.2	–1.2
m	3.5	1.9	3.1	3.4	2.8	1.5	3	–1.9	–2.0	–3.3	–2.6	–1.7	–0.3	0.2	–0.5	–5.7	–0.8	–2.1	–2.6	–2.4	–1.5	–1.1	–1.4
Cloud off tests “dry”																							
a	9.8	4.5	8.3	6.0	6.1	3.9	N/A	21.1	20.3	13.3	14.0	16.8	21.8	27.2	25.9	14.2	25.7	12.9	10.9	10.0	14.0	15.4	18.4
b	8.9	3.9	7.5	5.3	5.1	2.8	N/A	17.3	16.6	10.1	10.6	13.0	17.7	23.2	22.0	11.5	21.7	9.9	7.7	7.0	9.7	10.6	10.8
c	8.9	3.6	6.7	4.6	4.4	2.4	N/A	16.8	16.0	9.1	9.2	11.2	15.2	19.9	18.7	9.2	18.3	7.3	5.1	4.4	7.0	7.7	7.0
d	8.0	3.4	5.9	4.0	3.8	1.9	N/A	13.7	12.9	6.9	7.1	8.9	12.4	16.5	15.1	6.6	14.7	4.5	2.2	1.6	3.9	4.5	3.1
e	7.1	3.1	5.2	3.4	3.3	1.5	N/A	10.6	9.8	4.7	4.9	6.4	9.2	12.6	11.3	3.6	10.7	1.7	–0.6	–1.1	0.8	1.4	–0.6
f	7.1	2.8	4.6	3.4	3.0	1.5	N/A	10.1	9.4	3.9	3.7	4.9	7.3	10.0	8.6	1.9	8.1	0.7	–1.1	–1.5	–0.3	0.2	–1.0
g	7.1	2.8	3.9	3.4	3.0	1.5	N/A	10.2	9.4	3.9	3.6	4.6	6.2	7.9	6.1	0.2	5.6	–0.1	–1.6	–1.9	–0.5	0.0	–1.1
h	7.1	2.8	3.3	3.4	3.0	1.5	N/A	10.2	9.4	3.9	3.5	4.2	5.2	5.8	3.7	–1.5	3.2	–1.0	–2.1	–2.3	–0.8	–0.2	–1.2
i	7.1	2.8	2.8	3.4	3.0	1.5	N/A	10.1	9.4	3.8	3.4	3.9	4.2	3.8	1.5	–3.1	0.9	–1.9	–2.6	–2.7	–1.1	–0.4	–1.3
j	7.1	3.1	2.3	3.4	3.0	1.5	N/A	10.6	9.8	4.6	4.4	4.8	4.3	2.4	–0.3	–4.4	–0.9	–2.6	–2.9	–2.9	–1.2	–0.5	–1.4
k	5.5	3.1	2.3	3.5	3.0	1.5	N/A	6.7	6.1	3.0	3.7	4.4	4.1	2.2	–0.6	–4.6	–1.1	–2.7	–3.1	–3.0	–1.3	–0.6	–1.5
l	4.1	2.6	2.3	3.5	3.0	1.5	N/A	1.9	1.5	–0.5	0.5	1.4	1.7	0.9	–1.3	–5.1	–1.8	–3.0	–3.3	–3.3	–1.5	–0.8	–1.6
m	3.5	1.9	3.1	3.4	2.8	1.5	N/A	–1.2	–1.6	–3.6	–3.0	–1.9	–0.2	1.8	0.9	–3.7	0.4	–2.2	–2.9	–3.1	–2.3	–1.8	–1.8

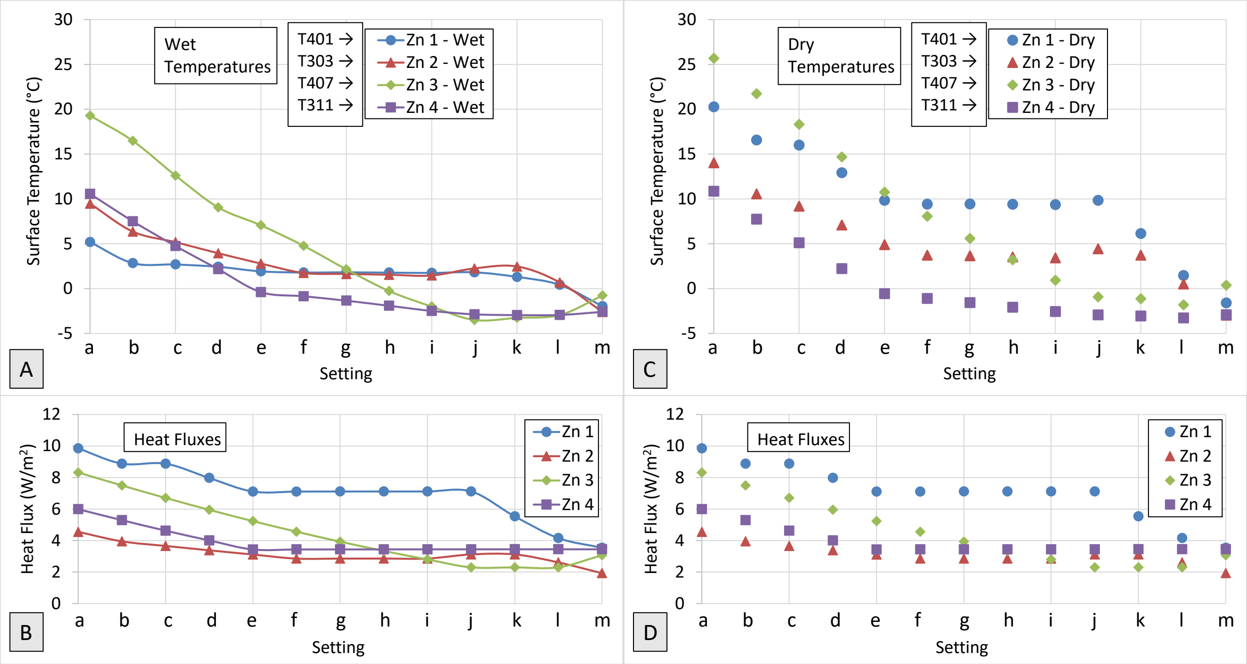

Figure 41.—(A) Representative wet surface temperatures for Zones 1 to 4, (B) resulting from the various heat flux settings tested, (C) along with the corresponding dry surface temperatures (D) for the same heat flux settings for the IC icing threshold test conducted at 207 knots.

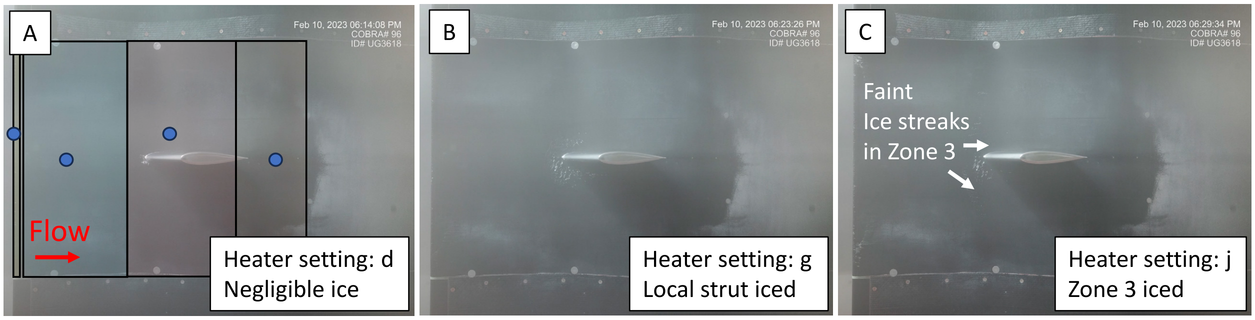

Figure 42.—A sequence of ice accretions resulting from the ice crystal icing threshold test at 207 knots (Run no. UG3618), where the heat flux was systematically reduced in intervals from the back end moving forward (from Panel (A) to (C)).

8.0 Conclusion

This report discusses data collected from icing tests conducted in 2023 using the SIDRM test article at the NASA Icing Research Tunnel. The 2023 tests utilized modified 7-in. NACA 0018 struts, which were larger compared to the 4-in. NACA 0012 struts used in the counterpart 2022 tests, for the purpose of impacting ice crystal ice accretions. Due to facility reference pressure issues in 2023 that primarily impacted the airspeed, comparison of data between the 2022 and 2023 test entries were limited. The report provides data and discussion on aerodynamic tests, supercooled liquid icing tests, ice crystal icing tests, and heat flux icing threshold tests.

Aerodynamic tests were conducted at various *AOA* and airspeeds to characterize the flow field around the test article. Flow separation occurred further aft on the pressure side for greater *AOA*, and further aft on both sides of the test article at greater airspeeds. Pressure coefficient data indicated that there was no impact on the flow due to the 0.5 in. gap between the test article and the test section for the forward 30% of the chord, where icing primarily occurred, but impacted flow towards the ceiling beyond 30% chord. There was good repeatability of pressure coefficient data for the forward portion of the test article between the 2022 and 2023 test entries, but the discrepancies in airspeed (due to the reference pressure issue), are likely the reason for poor pressure data repeatability for the aft portion of the test article. Finer AOA increment tests pinpointed the stagnation line at the leading edge at $AOA = 0.1°$ for $U = 100.5$ knots, and at $AOA = 0.3°$ for airspeeds of 152.5 and 207 knots.

Various parametric sweeps were conducted under supercooled liquid clouds, with the primary objective to measure that parameter's impact on ice accretion size, location, and characteristics. Ice mass, 3D laser scans, photography, and video were primary measurements to characterize the accreted ice. Higher MVD, lower total air temperatures, lower angles of attack, and longer spray times were the primary parameters that resulted in greater ice mass. Larger droplets are more ballistic and resulted in greater collection efficiency. Colder air temperatures resulted in less shedding compared to warmer air temperature accretions (and hence less mass loss). Smaller angles of attack resulted in fewer shadow regions leading to more ice accretion. Longer spray duration times provide greater time to accrete more ice. Test article AoA and cloud MVD impacted the location of ice accretion. Test article AoA directly influenced collection efficiency along the chord of the test article creating shadow regions. Cloud MVD impacted collection efficiency along the test article chord resulting in different impingement limits downstream of the leading edge as larger droplets are more ballistic and smaller droplets follow the flow. Total air temperature and cloud MVD were the primary parameters impacting icing characteristics. Warmer air temperatures resulted in glaze ice while colder conditions resulted in rime ice accretions. Smaller MVD clouds and warmer air temperatures resulted in greater amounts of feather shedding on the steep inclined area of the test article. The larger struts accreted more ice compared to the smaller struts used during the 2022 test entry. Various cross sections of ice accretions on the main body and struts were provided for comparison for all parameter sweeps.

Parametric sweeps were conducted under ice crystal clouds. Measurements to characterize the icing included surface heat flux at six heating zones, thermocouple data, ice mass, 3D laser scans of the accreted ice (not shown in this report), and photo images. A sufficiently high surface heat flux at the leading edge (i.e., sufficiently warm) can provide a continuous supply of liquid melt downstream resulting in greater ice mass compared to a lower surface heat flux. A lower flux setting results in the leading edge cooling down enough that it ceases to produce melt for accretion downstream. Longer spray duration times, along with greater AOA test conditions resulted in greater amounts of accreted ice mass. The greater ice mass result can be directly linked to increased collision efficiency (and collection efficiency) for the greater AOA test runs. Tests conducted at greater angles of attack resulted in more orderly shark teeth ice shape features, which had been observed during full-scale engine icing tests previously conducted at NASA GRC. The location and physical appearance of ice accretions were similar between the 2022 and 2023 test entries for repeated test conditions. However, ice mass was generally lower in the 2023 tests, possibly due to the larger strut displacing ice that had accreted in that location in the 2022 tests, along with discrepancies in airspeed due to the reference pressure issue. Overall, the larger struts used during this 2023 entry had little impact on ice crystal ice accretion.

Icing threshold tests were conducted under SCL and IC clouds to determine heat flux settings that differentiate between running wet and icing conditions. These tests provided heat transfer data for surfaces that generated running wet conditions, much like an ice protection system. Heat flux threshold values were determined for the forward portion of the test article at 152.5 and 207 knots. The icing threshold heat flux was greater for the higher airspeed test runs, as additional heat was needed to overcome the energy loss at the surface due to convective cooling. Corresponding dry tests (no icing cloud) conducted at the same heater settings during the SCL and IC icing threshold tests measured warmer surface temperatures as the surface for running-wet tests experienced evaporative cooling. Current IC cloud generation capabilities at the IRT limited the time to conduct the heat flux threshold tests. Improving upon the systematic heat flux setting procedures can provide more accurate threshold values for both SCL and IC tests.

Appendix A.—Supplemental Information on the SIDRM Test Article and Test Data

TABLE A.1.—NOMINAL LOCATION OF TYPE-K THERMOCOUPLES FLUSH WITH THE TEST ARTICLE OUTER MOLD LINE, WHERE (0, 0, 0) IS LOCATED AT THE MIDSPAN LEADING EDGE

TC name, ID	x (negative towards floor), in.	y (negative towards instrumented side), in.	z (negative downstream of LE), in.	Heater zone, no.
T201	–2.500	0.000	0.000	1
[a]T301	0.000	0.000	0.000	1
T401	2.500	0.000	0.000	1
T302	0.000	–0.842	–2.500	2
T303	0.000	–1.283	–5.000	2
T304	0.000	–1.723	–7.500	2
T305	0.000	–2.164	–10.000	2
T306	0.000	–2.762	–12.500	3
T207	–2.500	–4.196	–15.000	3
T307	0.000	–4.196	–15.000	3
T407	2.500	–4.196	–15.000	3
T310	0.000	–9.207	–21.480	4
T311	0.000	–10.546	–23.980	4
T312	0.000	–10.841	–26.480	4
T313	0.000	–10.830	–31.480	5
T314	0.000	–10.715	–36.480	5
T315	0.000	–7.716	–50.940	6
BT303	0.000	1.283	–5.000	2
BT307	0.000	4.196	–15.000	3
BT311	0.000	10.546	–23.980	4
BT314	0.000	10.715	–36.480	5
BT315	0.000	7.716	–50.940	6

[a] T301 was not functioning properly during icing tests.

TABLE A.2.—NOMINAL LOCATION OF TYPE-K THERMOCOUPLES LOCATED INTERNALLY NEAR THE SIDRM LEADING EDGE, WHERE (0, 0, 0) IS LOCATED AT THE MIDSPAN LEADING EDGE

TC name, ID	x (negative towards floor), in.	y (negative towards instrumented side), in.	z (negative downstream of LE), in.	Heater zone, no.
IT101	–3.750	0.000	–0.093	1
IT201	–1.250	0.000	–0.093	1
IT301	1.250	0.000	–0.093	1
IT401	3.750	0.000	–0.093	1

TABLE A.3.—NOMINAL LOCATION OF HEAT FLUX GAUGES (HFG) EPOXIED INTO POCKETS OF THE TEST ARTICLE INNER MOLD LINE, WHERE (0, 0, 0) IS LOCATED AT THE MIDSPAN LEADING EDGE.

HFG name, ID	x (negative towards floor), in.	y (negative towards instrumented side), in.	z (negative downstream of LE), in.	Heater zone, no.
HFG302	–0.950	–0.622	–2.500	2
HFG303	–0.950	–1.063	–5.000	2
HFG304	–0.950	–1.503	–7.500	2
HFG305	–0.950	–1.944	–10.000	2
HFG306	–0.950	–2.543	–12.500	3
HFG207	–3.450	–3.977	–15.000	3
HFG307	–0.950	–3.977	–15.000	3
HFG407	0.550	–3.977	–15.000	3
HFG310	–0.950	–8.987	–21.478	4
HFG311	–0.950	–10.326	–23.977	4
HFG312	–0.950	–10.621	–26.480	4

TABLE A.4.—NOMINAL LOCATION OF TYPE-T THERMOCOUPLES INTEGRATED INTO THE HEAT FLUX GAUGES EPOXIED INTO POCKETS OF THE TEST ARTICLE INNER MOLD LINE, WHERE (0, 0, 0) IS LOCATED AT THE MIDSPAN LEADING EDGE

TC name, ID	x (negative towards floor), in.	y (negative towards instrumented side), in.	z (negative downstream of LE), in.	Heater zone, no.
TC_HFG302	–0.425	–0.622	–2.500	2
TC_HFG303	–0.425	–1.063	–5.000	2
TC_HFG304	–0.425	–1.503	–7.500	2
TC_HFG305	–0.425	–1.944	–10.000	2
TC_HFG306	–0.425	–2.543	–12.500	3
TC_HFG207	–2.925	–3.977	–15.000	3
TC_HFG307	–0.425	–3.977	–15.000	3
TC_HFG407	1.075	–3.977	–15.000	3
TC_HFG310	–0.425	–8.989	–21.478	4
TC_HFG311	–0.425	–10.326	–23.977	4
TC_HFG312	–0.425	–10.621	–26.480	4

TABLE A.5.—NOMINAL LOCATION OF PRESSURE TAPS LOCATED ON THE TEST ARTICLE OUTER MOLD LINE, WHERE (0, 0, 0) IS LOCATED AT THE MIDSPAN LEADING EDGE

Pressure tap name, ID	x (negative towards floor), in.	y (negative towards instrumented side), in.	z (negative downstream of LE), in.	Pressure tap name, ID	x (negative towards floor), in.	y (negative towards instrumented side), in.	z (negative downstream of LE), in.
Lower row pressure taps				Upper row pressure taps			
P101	–16.750	0.000	0.000	P201	16.750	0.000	0.000
P102	–17.000	–0.165	–0.030	P202	17.000	–0.165	–0.030
P103	–17.250	–0.289	–0.100	P203	17.250	–0.289	–0.100
P104	–17.500	–0.377	–0.190	P204	17.500	–0.377	–0.190
P105	–17.750	–0.437	–0.300	P205	17.750	–0.437	–0.300
P106	–17.250	–0.953	–3.130	P206	17.250	–0.953	–3.130
P107	–17.250	–1.505	–6.260	P207	17.250	–1.505	–6.260
P108	–17.250	–2.770	–12.520	P208	17.250	–2.770	–12.520
P109	–17.250	–7.127	–18.780	P209	17.250	–7.127	–18.780
P110	–17.250	–9.506	–21.910	P210	17.250	–9.506	–21.910
P111	–17.250	–10.777	–25.040	P211	17.250	–10.777	–25.040
P112	–17.250	–10.840	–28.170	P212	17.250	–10.840	–28.170
P113	–17.250	–10.831	–31.300	P213	17.250	–10.831	–31.300
P114	–17.250	–10.658	–37.550	P214	17.250	–10.658	–37.550
P115	–17.250	–9.907	–43.810	P215	17.250	–9.907	–43.810
P116	–17.250	–8.080	–50.070	P216	17.250	–8.080	–50.070
P117	–17.250	–4.794	–56.330	P217	17.250	–4.794	–56.330
P118	–17.250	0.000	–62.590	P218	17.250	0.000	–62.590
P119	–17.250	0.289	–0.100	P219	17.250	0.289	–0.100
P120	–17.750	0.437	–0.300	P220	17.750	0.437	–0.300
P121	–17.250	0.953	–3.130	P221	17.250	0.953	–3.130
P122	–17.250	1.505	–6.260	P222	17.250	1.505	–6.260
P123	–17.250	2.770	–12.520	P223	17.250	2.770	–12.520
P124	–17.250	7.127	–18.780	P224	17.250	7.127	–18.780
P125	–17.250	9.506	–21.910	P225	17.250	9.506	–21.910
P126	–17.250	10.777	–25.040	P226	17.250	10.777	–25.040
P127	–17.250	10.840	–28.170	P227	17.250	10.840	–28.170
P128	–17.250	10.831	–31.300	P228	17.250	10.831	–31.300
P129	–17.250	10.658	–37.550	P229	17.250	10.658	–37.550
P130	–17.250	9.907	–43.810	P230	17.250	9.907	–43.810
P131	–17.250	8.080	–50.070	P231	17.250	8.080	–50.070
P132	–17.250	4.794	–56.330	P232	17.250	4.794	–56.330

TABLE A.6.—PROFILE GEOMETRY OF SIDRM MAIN BODY LISTED AS 181 POINTS

[Negative “z” values refer to a chord location downstream of the main body leading edge. The profile is symmetric around the “y” coordinate. The leading edge of the 7-in. chord NACA 0018 struts occurs at z = –12.978 in., where the span extends 9.852 in. from the strut junction leading edge. Rounded endcaps that are 0.4 in. at maximum thickness cap the open end of the struts.]

Point no.	z, in.	y, in.	Point no.	z, in.	y, in.	Point no.	z, in.	y, in.	Point no.	z, in.	y, in.
1	0.0000	0.0000	46	–0.4783	0.4849	91	–14.5344	3.8655	136	–30.0679	10.8371
2	–0.0022	0.0457	47	–0.4863	0.4865	92	–14.7744	4.0329	137	–30.7906	10.8343
3	–0.0089	0.0909	48	–0.4943	0.4880	93	–15.0144	4.2060	138	–31.5133	10.8300
4	–0.0200	0.1353	49	–0.5023	0.4895	94	–15.2544	4.3839	139	–32.2360	10.8236
5	–0.0353	0.1783	50	–0.5103	0.4909	95	–15.4944	4.5657	140	–32.9587	10.8147
6	–0.0548	0.2197	51	–0.5183	0.4924	96	–15.7344	4.7503	141	–33.6814	10.8026
7	–0.0782	0.2590	52	–0.5263	0.4938	97	–15.9744	4.9369	142	–34.4041	10.7869
8	–0.1053	0.2958	53	–0.5343	0.4953	98	–15.9744	4.9369	143	–35.1268	10.7667
9	–0.1359	0.3298	54	–0.5423	0.4967	99	–16.4680	5.3224	144	–35.8495	10.7415
10	–0.1697	0.3606	55	–0.5503	0.4981	100	–17.4680	6.1034	145	–36.5722	10.7104
11	–0.2063	0.3880	56	–0.5583	0.4995	101	–18.4680	6.8844	146	–37.2949	10.6728
12	–0.2063	0.3880	57	–0.5663	0.5009	102	–19.4680	7.6654	147	–38.0176	10.6279
13	–0.2143	0.3933	58	–0.5743	0.5023	103	–20.2144	8.2483	148	–38.7403	10.5749
14	–0.2223	0.3983	59	–0.5823	0.5038	104	–20.2144	8.2483	149	–39.4630	10.5130
15	–0.2303	0.4031	60	–0.5903	0.5052	105	–20.4544	8.4355	150	–40.1858	10.4414
16	–0.2383	0.4078	61	–0.5983	0.5066	106	–20.6944	8.6214	151	–40.9085	10.3592
17	–0.2463	0.4122	62	–0.6063	0.5080	107	–20.9344	8.8049	152	–41.6312	10.2658
18	–0.2543	0.4164	63	–0.6063	0.5080	108	–21.1744	8.9852	153	–42.3539	10.1602
19	–0.2623	0.4204	64	–1.4680	0.6599	109	–21.4144	9.1610	154	–43.0766	10.0417
20	–0.2703	0.4243	65	–2.4680	0.8363	110	–21.6544	9.3314	155	–43.7993	9.9095
21	–0.2783	0.4279	66	–3.4680	1.0126	111	–21.8944	9.4956	156	–44.5220	9.7628
22	–0.2863	0.4315	67	–4.4680	1.1889	112	–22.1344	9.6525	157	–45.2447	9.6008
23	–0.2943	0.4348	68	–5.4680	1.3652	113	–22.3744	9.8015	158	–45.9674	9.4230
24	–0.3023	0.4381	69	–6.4680	1.5416	114	–22.6144	9.9417	159	–46.6901	9.2284
25	–0.3103	0.4411	70	–7.4680	1.7179	115	–22.8544	10.0726	160	–47.4128	9.0166
26	–0.3183	0.4441	71	–8.4680	1.8942	116	–23.0944	10.1934	161	–48.1355	8.7869
27	–0.3263	0.4469	72	–9.4680	2.0705	117	–23.3344	10.3039	162	–48.8582	8.5387
28	–0.3343	0.4496	73	–10.4544	2.2445	118	–23.5744	10.4036	163	–49.5809	8.2714
29	–0.3423	0.4522	74	–10.4544	2.2445	119	–23.8144	10.4923	164	–50.3036	7.9847
30	–0.3503	0.4547	75	–10.6944	2.2871	120	–24.0544	10.5700	165	–51.0263	7.6780
31	–0.3583	0.4571	76	–10.9344	2.3316	121	–24.2944	10.6367	166	–51.7490	7.3511
32	–0.3663	0.4594	77	–11.1744	2.3797	122	–24.5344	10.6927	167	–52.4717	7.0036
33	–0.3743	0.4616	78	–11.4144	2.4327	123	–24.7744	10.7383	168	–53.1944	6.6352
34	–0.3823	0.4638	79	–11.6544	2.4918	124	–25.0144	10.7741	169	–53.9171	6.2460
35	–0.3903	0.4658	80	–11.8944	2.5582	125	–25.2544	10.8010	170	–54.6398	5.8356
36	–0.3983	0.4678	81	–12.1344	2.6324	126	–25.4944	10.8197	171	–55.3625	5.4042
37	–0.4063	0.4698	82	–12.3744	2.7153	127	–25.7344	10.8315	172	–56.0852	4.9519
38	–0.4143	0.4716	83	–12.6144	2.8071	128	–25.9744	10.8378	173	–56.8079	4.4788
39	–0.4223	0.4734	84	–12.8544	2.9081	129	–26.2144	10.8402	174	–57.5306	3.9852
40	–0.4303	0.4752	85	–13.0944	3.0185	130	–26.4544	10.8406	175	–58.2533	3.4714
41	–0.4383	0.4769	86	–13.3344	3.1382	131	–26.4544	10.8406	176	–58.9760	2.9380
42	–0.4463	0.4786	87	–13.5744	3.2671	132	–27.1771	10.8404	177	–59.6987	2.3854
43	–0.4543	0.4802	88	–13.8144	3.4047	133	–27.8998	10.8402	178	–60.4214	1.8145
44	–0.4623	0.4818	89	–14.0544	3.5507	134	–28.6225	10.8397	179	–61.1441	1.2260
45	–0.4703	0.4834	90	–14.2944	3.7045	135	–29.3452	10.8388	180	–61.8669	0.6208
									181	–62.5896	0.0000

TABLE A.7.—LANGMUIR-D 7-BIN DROP SIZE DISTRIBUTIONS OF SUPERCOOLED LIQUID CLOUDS PRESENTED IN THIS REPORT

[End-point values are provided for each bin. The cumulative bin fraction is listed in the first column.]

SCL Cloud *MVD* →	18 µm	25 µm	30 µm	50 µm	90 µm
Cumulative bin fraction	Drop diam., µm	Drop diam., µm	Drop diam., µm	Drop diam., µm	Drop diam., µm
0	4	4	4	4	4
0.05	7	8	8	9	12
0.15	10	11	11	13	25
0.35	13	19	20	29	56
0.65	23	35	46	83	139
0.85	33	61	92	154	218
0.95	45	103	154	217	293
1	177	299	314	378	775

TABLE A.8.—PARTICLE SIZE DISTRIBUTIONS OF ICE CRYSTAL CLOUDS PRESENTED IN THIS REPORT

[Mid-point values are provided for each bin. The individual bin fraction is listed in the first column.]

IC Cloud *MVD* →	26 µm	27 µm	28 µm	41 µm
Bin fraction	Particle diam., µm	Particle diam., µm	Particle diam., µm	Particle diam., µm
0.1	5	6	6	7
0.1	12	13	14	18
0.1	16	17	18	24
0.1	20	20	22	31
0.1	24	25	26	37
0.1	29	29	30	44
0.1	34	34	35	52
0.1	41	41	41	63
0.1	50	50	50	77
0.1	71	71	74	118

TABLE A.9.—TEST RUN PRESPRAY CONDITIONS WITH CORRESPONDING STEADY STATE SURFACE TEMPERATURES PRIOR TO SPRAY ACTIVATION

[Light orange shaded cells indicated the test condition or heater setting that was varied for the test objective block. Thermocouple T307 is located directly under the strut. Due to the absence of heating directly under the strut, T307 measured lower temperatures compared to surrounding thermocouples.]

Test run prespray conditions				Heater settings						Prespray steady state surface TC temperatures															
										Zone 1		Zone 2				Zone 3				Zone 4			Zone 5		Zone 6
Test run, no.	T_0, °C	U, kn	AOA, °	Zone 1 flux, W/in^2	Zone 2 flux, W/in^2	Zone 3 flux, W/in^2	Zone 4 flux, W/in^2	Zone 5 flux, W/in^2	Zone 6 flux, W/in^2	T201, °C	T401, °C	T302, °C	T303, °C	T304, °C	T305, °C	T306, °C	T207, °C	T307, °C	T407, °C	T310, °C	T311, °C	T312, °C	T313, °C	T314, °C	T315, °C
Block 1: Repeat of 2022 test conditions at T_0 = –15 °C																									
UG3596	–15	152.5	0	7.1	2.8	3.3	3.2	6.3	4.0	13.9	13.2	7.9	7.3	8.0	8.8	8.0	6.1	0.1	6.3	0.9	0.7	1.9	14.8	18.7	23.1
UG3592	–15	152.5	2	7.1	2.8	2.7	3.2	6.3	4.0	16.6	15.6	11.4	9.3	8.9	8.3	5.5	3.7	–2.5	3.8	0.4	0.7	2.1	14.9	18.9	21.6
UG3581	–15	152.5	4	7.1	2.3	2.5	3.2	6.3	4.0	22.1	20.3	19.9	16.3	11.8	9.5	7.6	5.0	0.0	4.9	1.0	1.1	2.1	15.4	19.1	20.7
Block 2: Repeat of 2022 test conditions at T_0 = –20 °C																									
UG3599	–20	152.5	0	8.9	3.6	4.2	4.0	7.9	4.6	16.5	15.8	9.0	8.5	9.5	10.5	9.4	6.7	–2.1	6.7	0.1	0.1	1.4	17.4	22.2	25.1
UG3595	–20	152.5	2	8.9	3.6	3.3	4.0	7.9	4.6	19.1	17.7	12.7	10.4	10.1	9.5	6.8	3.3	–4.2	3.2	–0.8	–0.3	1.3	17.2	21.9	23.1
UG3594	–20	152.5	4	8.9	3.1	3.3	4.0	7.9	4.6	20.3	18.3	18.6	15.1	10.7	8.4	6.0	2.8	–4.7	2.9	–0.5	0.1	1.6	17.3	22.0	21.3
UG3626	–20	152.5	4	8.9	3.1	3.3	4.0	7.9	4.6	21.4	18.7	19.7	16.3	11.6	9.1	6.7	3.7	–2.1	3.9	0.0	0.7	2.0	17.6	22.5	21.7
Block 3: Heater surface heat flux evaluation																									
UG3629	–20	152.5	4	7.1	3.1	3.3	4.4	7.5	5.3	15.5	13.5	16.1	14.2	10.6	8.7	6.5	3.4	–4.0	3.5	1.0	1.8	2.7	16.8	21.1	26.5
UG3627	–20	152.5	4	9.9	3.1	3.3	4.4	7.5	5.3	24.5	21.7	21.5	17.3	12.2	9.7	7.3	3.9	–3.1	3.9	1.1	1.8	2.8	16.8	21.1	26.1
UG3637	–20	152.5	4	12.0	3.1	3.3	4.4	7.5	5.3	30.1	27.3	24.9	19.3	13.2	10.1	7.7	4.0	–3.1	3.9	0.9	1.6	2.7	16.6	20.9	26.3
UG3630	–20	152.5	4	12.0	3.6	3.9	4.4	7.5	5.3	32.7	30.0	29.4	24.3	18.0	14.8	11.7	7.8	–1.3	7.8	2.7	2.8	3.6	17.5	21.7	27.0
Block 4: Spray duration time sweep																									
UG3622	–20	152.5	0	16.7	3.9	4.2	6.1	7.5	5.3	40.4	38.7	21.8	16.5	15.2	14.9	12.8	9.3	2.3	9.7	6.6	8.2	8.8	18.7	22.4	31.5
UG3624	–20	152.5	0	16.7	3.9	4.2	6.1	7.5	5.3	40.5	39.0	21.9	16.7	15.4	14.9	12.3	8.7	–0.1	9.0	6.5	8.1	8.7	18.8	22.6	31.5
Block 5: AOA sweep at T_0 = –15 °C and U = 207 knots																									
UG3600	–15	207	0	9.9	3.1	3.3	4.4	7.5	5.3	17.8	16.0	7.4	5.7	5.9	6.3	5.2	3.1	–1.8	3.2	0.2	0.7	1.6	13.4	16.7	24.8
UG3601	–15	207	2	9.9	3.1	3.3	4.4	7.5	5.3	19.3	18.3	10.5	7.7	7.2	7.3	6.5	4.1	–2.1	3.7	1.0	1.1	2.0	14.0	17.0	23.3
UG3597	–15	207	4	9.9	3.1	3.3	4.4	7.5	5.3	21.9	20.1	18.5	13.5	9.6	8.2	6.9	4.4	–2.1	4.0	1.4	1.4	2.3	13.9	16.8	21.7
UG3623	–15	207	4	9.9	3.1	3.3	4.4	7.5	5.3	23.0	20.6	19.5	14.6	10.4	8.8	7.8	5.1	–1.2	4.6	2.0	2.0	2.7	14.7	17.7	22.7
Block 6: AOA sweep at T_0 = –20 °C and U = 152.5 knots																									
UG3611	–20	152.5	0	9.9	3.1	3.3	4.4	7.5	5.3	18.1	17.1	8.2	6.2	6.2	6.5	5.1	2.3	–4.9	2.3	–0.5	0.1	1.6	15.9	20.3	30.2
UG3610	–20	152.5	2	9.9	3.1	3.3	4.4	7.5	5.3	21.6	20.1	13.7	9.2	7.8	7.4	5.7	2.9	–4.4	2.9	0.1	1.0	2.3	16.2	20.6	28.0
UG3609	–20	152.5	4	9.9	3.1	3.3	4.4	7.5	5.3	23.5	21.4	21.8	18.2	12.9	9.7	7.0	3.8	–2.5	4.0	0.7	1.5	2.8	16.2	20.3	25.4
UG3636	–20	152.5	4	9.9	3.1	3.3	4.4	7.5	5.3	24.1	21.6	22.1	18.7	13.3	10.1	7.5	3.9	–2.9	4.0	0.9	1.7	2.8	16.5	20.8	26.2

References

1. Bravin, M., and Strapp, J.W., "A Continuing Investigation of Diurnal and Location Trends in an Ice Crystal Icing Engine Event Data Base," *SAE International Conference on Icing of Aircraft, Engines, and Structures*, SAE, Minneapolis, MN, 2019, SAE Technical Paper 2019-01-1964.
2. Bravin, M., Strapp, J.W., and Mason, J., "An Investigation into Location and Convective Lifecycle Trends in an Ice Crystal Icing Engine Event Database," 2015 *SAE International Conference on Icing of Aircraft, Engines, and Structures*, SAE, Prague, Czech Republic, 2015, SAE Technical Paper 2015-01-2130.
3. Mason, J. G., Strapp, J. W., and Chow, P., "The Ice Particle Threat to Engines in Flight," *44th AIAA Aerospace Sciences Meeting and Exhibit*, AIAA, Reno, NV, 2006, AIAA-2006-206.
4. Mason, J.G., Chow, P., and Riley, J., "Engine Ice Crystal Icing Technology Plan with Research Needs," Federal Aviation Administration Report, DOT/FAA/TC-20/34, 2020.
5. Struk, P. M., Agui, J. H., Bartkus, T. P., Tsao, J.-C., King, M. J., and Ratvasky, T. "Ice-Crystal Icing Accretion Studies at the NASA Propulsion Systems Laboratory," *SAE 2019 International Conference on Icing of Aircraft, Engines, and Structures*, SAE, Minneapolis, MN, 2019, SAE Technical Paper 2019-01-1921.
6. Bartkus, T. P., Tsao, J.-C., and Struk, P. M. "Analysis of Experimental Ice Accretion Data and Assessment of a Thermodynamic Model During Ice Crystal Icing," 2019 *SAE International Conference on Icing of Aircraft, Engines, and Structures*, SAE, Minneapolis, MN, 2019, SAE Technical Paper, 2019-01-2016.
7. Bartkus, T. P., Struk, P. M., and Tsao, J.-C., "Evaluation of a Thermodynamic Ice Crystal Icing Model Using Experimental Ice Accretion Data," *2018 AIAA Atmospheric and Space Environments Conference*, AIAA, Atlanta, GA, 2018, AIAA-2018-4129.
8. Struk, P. M., Ratvasky, T. P., Bencic, T., Van Zante, J. F., King, M. C., Tsao, J.-C., and Bartkus, T. P. "An Initial Study of the Fundamentals of Ice Crystal Icing Physics in the NASA Propulsion Systems Laboratory," *9th AIAA Atmospheric and Space Environments Conference*, AIAA, Denver, CO, 2017, AIAA-2017-4242.
9. Struk, P. M., Tsao, J.-C., and Bartkus, T. B., "Plans and Preliminary Results of Fundamental Studies of Ice Crystal Icing Physics in the NASA Propulsion Systems Laboratory," *8th AIAA Atmospheric and Space Environments Conference*, 2016, AIAA-2016-3738.
10. Bucknell, A., McGilvray, M., Gillespie, D., Parker, L. et al., "Experimental Study and Analysis of Ice Crystal Accretion on a Gas Turbine Compressor Stator Vane," 2019 *SAE International Conference on Icing of Aircraft, Engines, and Structures*, SAE, Minneapolis, MN, 2019, SAE Technical Paper 2019-01-1927.
11. Bucknell, A. J., McGilvray, M., Gillespie, D., Jones, G., Reed, A., and Collier, B., "Experimental Studies of Ice Crystal Accretion on an Axisymmetric Body at Engine-Realistic Conditions," *2018 AIAA Atmospheric and Space Environments Conference*, AIAA, Atlanta, GA, 2018, AIAA-2018-4223.
12. Struk, P. M., King, M. C., Bartkus, T. P., Tsao, J.-C., Fuleki, D., Neuteboom, M., and Chalmers, J. L., "Ice Crystal Icing Physics Study Using a NACA 0012 Airfoil at the National Research Council of Canada's Research Altitude Test Facility," *2018 AIAA Atmospheric and Space Environments Conference*, AIAA, Atlanta, GA, 2018, AIAA-2018-4224.
13. Struk, P. M., Bartkus, T. P., Tsao, J.-C., Currie, T., and Fuleki, D., "Ice Accretion Measurements on an Airfoil and Wedge in Mixed-Phase Conditions," 2015 *SAE International Conference on Icing of Aircraft, Engines, and Structures*, SAE, Prague, Czech Republic, 2015, SAE Technical Paper 2015-01-2116.

14. Currie, T. C., Fuleki, D., and Mahallati, A. “Experimental Studies of Mixed-Phase Sticking Efficiency for Ice Crystal Accretion in Jet Engines,” *6th AIAA Atmospheric and Space Environments Conference*, AIAA, Atlanta, GA, 2014, AIAA-2014-3049.
15. Currie, T. C., Fuleki, D., Knezevici, D. C., and MacLeod, J. D. “Altitude Scaling of Ice Crystal Accretion,” *5th AIAA Atmospheric and Space Environments Conference*, AIAA, San Diego, 2013, AIAA-2013-2677.
16. Currie, T. C., Struk, P. M., Tsao, J., Fuleki, D., and Knezevici, D. C. “Fundamental Study of Mixed-Phase Icing with Application to Ice Crystal Accretion in Aircraft Jet Engines,” *4th Atmospheric and Space Environments Conference,* AIAA, New Orleans, LA, 2012, AIAA-2012-3035.
17. Struk, P. M., Broeren, A. P., Tsao, J.-C., Vargas, M., Wright, W. B., Currie, T., Knezevici, D., and Fuleki, D., “Fundamental Ice Crystal Accretion Physics Studies,” *SAE 2011 International Conference on Aircraft and Engine Icing and Ground Deicing*, SAE, Chicago, IL, 2011, SAE Technical Paper 2011-38-0018, NASA/TM-2012-217429.
18. Connolly, J., Choi, M., Yang, X., Doherty, L.J. et al., “Ice Crystal Accretion in a Combined Linear Cascade and Swan Neck Duct,” *AIAA Aviation 2020 Forum*, AIAA, Virtual Event, 2020, *AIAA-2020*-2828.
19. Mason, J. G., Chow, P., and Fuleki, D. M., “Understanding Ice Crystal Accretion and Shedding Phenomenon in Jet Engines Using a Rig Test,” *Journal of Engineering for Gas Turbines and Power,* Vol. 133, No. 4, 2010, pp. 041201-041201-8. doi: 10.1115/1.4002020.
20. Mason, J., Neuteboom, M., Chalmers, J., Dumont, C., and Chow, P., “Ice Crystal Environment - Modular Axial Compressor Rig: Comparisons of Ice Accretion for 1 and 2 Stages of Compression,” *2023 SAE International Conference on Icing of Aircraft, Engines, and Structures,* SAE, Vienna, Austria, 2023, SAE Technical Paper 2023-01-1397, 2023.
21. Neuteboom, M., Dumont, C., Mason, J., Chalmers, J., and Chow, P., “NRC’s ICE-MACR 2018-2023: What Has Been Learned So Far,” *2023 SAE International Conference on Icing of Aircraft, Engines, and Structures,* SAE, Vienna, Austria, 2023, SAE Technical Paper 2023-01-1377.
22. Neuteboom, M.O. and Chalmers, J.L.Y., “Ice Crystal Environment-Modular Axial Compressor Rig: Transient Analysis of Icing Severity Levels,” *AIAA Aviation 2021 Forum,* AIAA, Virtual Event, 2021, AIAA-2021-2660.
23. Neuteboom, M.O., Chalmers, J.L.Y., and Davison, C.R., “Ice Crystal Environment-Modular Axial Compressor Rig: Overview of Altitude Icing Commissioning,” *AIAA Aviation 2020 Forum*, AIAA, Virtual Event, 2020, AIAA-2020-2823.
24. Flegel, A. B., “Ice Crystal Icing Investigation on a Honeywell Uncertified Research Engine in an Altitude Simulation Icing Facility,” *Proceedings of the ASME Turbo Expo 2020*, London, England, 2020, GT2020-14714.
25. Tsao, J.-C., “Scaling Evaluation of Ice-Crystal Icing on a Modern Turbofan Engine in PSL Using the COMDES-MELT Code,” *SAE International Conference on Icing of Aircraft, Engines, and Structures*, SAE, Minneapolis, MN, 2019, SAE Technical Paper 2019-01-1920.
26. Rigby, D. L., Wright, W. B., “Numerical Investigation of Particle Breakup and Ingestion into an Axial Low Pressure Compressor at Engine Icing Operating Points,” *2018 AIAA Atmospheric and Space Environments Conference*, AIAA, Atlanta, GA, 2018, AIAA-2018-4131.
27. Tsao, J.-C., “Preliminary Evaluation of Altitude Scaling for Turbofan Engine Ice Crystal Icing,” *9th AIAA Atmospheric and Space Environments Conference*, AIAA, Denver, CO, 2017, AIAA-2017-4086.
28. Rigby, D. L., Ameri, A. A., Veres, J., Jorgenson, P. C. E., “Viscous Three-Dimensional Simulation of Flow in an Axial Low Pressure Compressor at Engine Icing Operating Points,” *9th AIAA Atmospheric and Space Environments Conference*, AIAA, Denver, CO, 2017, AIAA-2017-4087.

29. Flegel, A. B., and Oliver, M. J., “Preliminary Results from a Heavily Instrumented Engine Ice Crystal Icing Test in a Ground Based Altitude Test Facility,” *8th AIAA Atmospheric and Space Environments Conference*, 2016, AIAA-2016-3894.
30. NASA Glenn Research Center, “When Hot Engines meet Ice Clouds” YouTube video [online May 5, 2016], URL: https://www.youtube.com/watch?v=L_6HxvwHsdg.
31. Veres, J. P., Jorgenson, P. C. E., Jones, S. M., “Modeling of Highly Instrumented Honeywell Turbofan Engine Tested with Ice Crystal Ingestion in the NASA Propulsion System Laboratory,” *8th AIAA Atmospheric and Space Environments Conference*, AIAA, Washington D.C., 2016, AIAA-2016-3895.
32. Oliver, M. J., “Validation Ice Crystal Icing Engine Test in the Propulsion Systems Laboratory at NASA Glenn Research Center,” *6th AIAA Atmospheric and Space Environments Conference*, AIAA, Atlanta, GA, 2014, AIAA-2014-2898.
33. Veres, J. P., Jorgenson, P. C. E., Coennen, R., “Modeling of Commercial Turbofan Engine with Ice Crystal Ingestion; Follow On,” *6th AIAA Atmospheric and Space Environments Conference*, AIAA, Atlanta, GA, 2014, AIAA-2014-2899.
34. Tsao, J.-C., Struk, P, Oliver, M., “Possible Mechanisms for Turbofan Engine Ice Crystal Icing at High Altitude,” *6th AIAA Atmospheric and Space Environments Conference*, AIAA, Atlanta, GA, 2014, AIAA-2014-3044.
35. Bartkus, T. P., and Lee, S., “Icing Physics Studies Using the 3D SIDRM Test Article: Ice Crystal Icing Analysis," *AIAA Aviation Forum and Ascend 2024*, Las Vegas, NV, 2024, AIAA-2024-3845.
36. Bartkus, T., Lee, S., and Stewart, E., “Icing Physics Studies Using the 3D SIDRM Test Article: Aerodynamic and Supercooled Liquid Icing Analysis,” *2023 SAE International Conference on Icing of Aircraft, Engines, and Structures,* SAE, Vienna, Austria, 2023, SAE Technical Paper 2023-01-1399.
37. Stewart, E. and Bartkus, T., “Computational Icing Analysis on NASA’s SIDRM Geometry to Investigate Collection Efficiency,” *2023 SAE International Conference on Icing of Aircraft, Engines, and Structures,* SAE, Vienna, Austria, 2023, SAE Technical Paper 2023-01-1476.
38. Bartkus, T. P., Lee, S., Potapczuk, M. G., and Flack. C. A., “Description of Cloud Characterization and Icing Tests for a 3D Heated Test Article at the NASA Icing Research Tunnel,” *AIAA Aviation 2022 Forum,* AIAA, Chicago, IL, 2022, AIAA-2022-3700.
39. Bartkus, T., Potapczuk, M., Lee, S., Stewart, E., and Chen, R.-C., “Plans for Ice Crystal Icing Tests Using a 3D Heated Test Article at the NASA Icing Research Tunnel,” *AIAA Aviation 2021 Forum,* AIAA, Virtual Event, 2021, Oral Presentation.
40. Porter, C., Potapczuk, M., Ozoroski, T., Sabri, Z, Galloway, E., Rigby, D., Wright, W., and Tsao P., “GlennICE Manual 4.1.0,” NASA Technical Memorandum, 2024, NASA/TM-20240002191.
41. Porter, C.E., “Utilization of Streamtubes to Analyze the Physical Interaction of a Dispersed Cloud with the CRM65 Hybrid Midspan Model,” *AIAA Aviation 2024 Forum,* AIAA, Las Vegas, NV, 2024, (submitted for publication).
42. Sabri, Z.H., and Porter, C.E., “A Study of Parallel Scalability and Dynamic Workload Balancing in GlennICE,” *AIAA Aviation 2024 Forum,* AIAA, Las Vegas, NV, 2024, (submitted for publication).
43. Sabri, Z. and Porter, C., “Scalability of GlennICE in a Parallel Environment,” *2023 SAE International Conference on Icing of Aircraft, Engines, and Structures,* SAE, Vienna, Austria, 2023, SAE Technical Paper 2023-01-1482.
44. Rigby, D. and von Hardenberg, P., “Demonstration of Initial GlennICE Relative Frame Capability: Axial-Flow Propeller,” *2023 SAE International Conference on Icing of Aircraft, Engines, and Structures,* SAE, Vienna, Austria, 2023, SAE Technical Paper 2023-01-1457.

45. Wright, W., Rigby, D., and Ozoroski, T., "Roughness Parameter Optimization of the McClain Model in GlennICE," *2023 SAE International Conference on Icing of Aircraft, Engines, and Structures,* SAE, Vienna, Austria, 2023, SAE Technical Paper 2023-01-1468.
46. Wright, W. B., Porter, C. E., Galloway E. T., and Rigby D. L, "GlennICE 2.1 Capabilities and Results," *AIAA Aviation 2022 Forum,* AIAA, Chicago, IL, 2022, AIAA-2022-3309.
47. Porter, C. E., "A Comparison of Trajectory Refinement Schemes for GlennICE," *AIAA Aviation 2022 Forum,* AIAA, Chicago, IL, 2022, AIAA-2022-3692.
48. Wright, W., Porter, C., Galloway, E., and Rigby, D. "An Automated Refinement Process for Particle Trajectory Methods in GlennICE," *AIAA Aviation 2021 Forum,* AIAA, Virtual Event, 2021, AIAA-2021-2631.
49. Porter, C. E., Rigby, D. L., "Three Dimensional Surface Redefinition Method for Computational Ice Accretion Solvers," *AIAA Aviation 2020 Forum*, AIAA, Virtual Event, 2020, *AIAA-2020*-2831.
50. Bartkus, T. P., Struk, P. M., and Tsao, J.-C., "Comparisons of Mixed-Phase Icing Cloud Simulations with Experiments Conducted at the NASA Propulsion Systems Laboratory," *9th AIAA Atmospheric and Space Environments Conference*, AIAA, Denver, CO, 2017, AIAA-2017-4243.
51. Bartkus, T. P., Struk, P. M., Tsao, J.-C., and Van Zante, J. F., "Numerical Analysis of Mixed-Phase Icing Cloud Simulations in the NASA Propulsion Systems Laboratory," *8th AIAA Atmospheric and Space Environments Conference*, AIAA, Washington D.C., 2016, AIAA-2016-3739.
52. Bartkus, T. P., Struk, P. M., and Tsao, J.-C., "Development of a Coupled Air and Particle Thermal Model for Engine Icing Test Facilities," *SAE International Journal of Aerospace,* Vol. 8, No. 1, 2015, pp. 15-32, SAE Journal Paper 2015-01-2155.
53. Brunner, C. E., Kiefer, J., Hansen, M. O., and Hultmark, M., "Study of Reynolds number effects on the aerodynamics of a moderately thick airfoil using a high-pressure wind tunnel," *Exp Fluids* 62, 178 (2021).